IOWA STATE UNIVERSITY
Digital Repository

Retrospective Theses and Dissertations

Iowa State University Capstones, Theses and Dissertations

1994

# New ultrasonic signal processing techniques for NDE applications

Myung-Hyun Yoon
*Iowa State University*

Follow this and additional works at: https://lib.dr.iastate.edu/rtd

 Part of the Electrical and Electronics Commons

Recommended Citation
Yoon, Myung-Hyun, "New ultrasonic signal processing techniques for NDE applications " (1994). *Retrospective Theses and Dissertations*. 10527.
https://lib.dr.iastate.edu/rtd/10527

This Dissertation is brought to you for free and open access by the Iowa State University Capstones, Theses and Dissertations at Iowa State University Digital Repository. It has been accepted for inclusion in Retrospective Theses and Dissertations by an authorized administrator of Iowa State University Digital Repository. For more information, please contact digirep@iastate.edu.

www.manaraa.com

# INFORMATION TO USERS

This manuscript has been reproduced from the microfilm master. UMI films the text directly from the original or copy submitted. Thus, some thesis and dissertation copies are in typewriter face, while others may be from any type of computer printer.

**The quality of this reproduction is dependent upon the quality of the copy submitted.** Broken or indistinct print, colored or poor quality illustrations and photographs, print bleedthrough, substandard margins, and improper alignment can adversely affect reproduction.

In the unlikely event that the author did not send UMI a complete manuscript and there are missing pages, these will be noted. Also, if unauthorized copyright material had to be removed, a note will indicate the deletion.

Oversize materials (e.g., maps, drawings, charts) are reproduced by sectioning the original, beginning at the upper left-hand corner and continuing from left to right in equal sections with small overlaps. Each original is also photographed in one exposure and is included in reduced form at the back of the book.

Photographs included in the original manuscript have been reproduced xerographically in this copy. Higher quality 6" x 9" black and white photographic prints are available for any photographs or illustrations appearing in this copy for an additional charge. Contact UMI directly to order.

UMI

University Microfilms International
A Bell & Howell Information Company
300 North Zeeb Road, Ann Arbor, MI 48106-1346 USA
313/761-4700 800/521-0600

Order Number 9503612

# New ultrasonic signal processing techniques for NDE applications

Yoon, Myung-Hyun, Ph.D.

Iowa State University, 1994

U·M·I
300 N. Zeeb Rd.
Ann Arbor, MI 48106

# New ultrasonic signal processing techniques for NDE applications

by

Myung-Hyun Yoon

A Dissertation Submitted to the

Graduate Faculty in Partial Fulfillment of the

Requirements for the Degree of

DOCTOR OF PHILOSOPHY

Department: Electrical Engineering and Computer Engineering
Major: Electrical Engineering (Communications and Signal Processing)

Approved:

Signature was redacted for privacy.

Signature was redacted for privacy.

In Charge of Major Work

Signature was redacted for privacy.

For the Major Department

Signature was redacted for privacy.

For the Graduate College

Iowa State University
Ames, Iowa
1994

Copyright © Myung-Hyun Yoon, 1994. All rights reserved.

# TABLE OF CONTENTS

**CHAPTER 1. INTRODUCTION** . . . . . 1

Overview of Ultrasonic Testing . . . . . 2

Research Objective and Approach . . . . . 7

Research Summary and Contributions . . . . . 8

Overview of Chapters . . . . . 10

**CHAPTER 2. WAVELET TRANSFORM BASED SIGNAL PROCESSING** . . . . . 12

Ultrasonic Flaw Detection . . . . . 13

Hypothesis Testing . . . . . 15

Signal Detection Using Matched Filter . . . . . 17

Detection Performance of Matched Filter . . . . . 19

Wavelet Transform Based Signal Processing . . . . . 23

Wavelet transform . . . . . 23

Proposed signal processing method . . . . . 27

Comparison with split-spectrum processing (SSP) . . . . . 29

System Performance Evaluation . . . . . 33

Magnitude of wavelet transform . . . . . 33

Relative peak location . . . . . 37

Magnitude ratio . . . . . 37
Overall system performance . . . . . 39

**CHAPTER 3. APPLICATION OF THE WAVELET TRANSFORM BASED SIGNAL PROCESSING METHOD TO THE HARD-ALPHA DETECTION PROBLEM** . . . . . 42

Ultrasonic Data Sets . . . . . 43
Statistical Analysis of Noise Signals . . . . . 43
Application to Hard-Alpha Detection . . . . . 54
Example 1 . . . . . 57
Example 2 . . . . . 58

**CHAPTER 4. KALMAN FILTER BASED DECONVOLUTION** . 66

Ultrasonic Signal and System Model . . . . . 66
Minimum-Variance Estimation . . . . . 71
Optimal filtering . . . . . 73
Optimal smoothing . . . . . 74
Deconvolution Algorithm . . . . . 75
Application Examples . . . . . 78
Example 1 . . . . . 84
Example 2 . . . . . 88
Example 3 . . . . . 88

**CHAPTER 5. COLORED SEQUENCE ESTIMATION** . . . . . 96

Colored System Model . . . . . 96
Iterative Scheme . . . . . 99
Simulation Results . . . . . 100

CHAPTER 6. SPACE VARYING DECONVOLUTION . . . . . 113
Space Varying System Model . . . . . 114
Parameter Interpolation . . . . . 117
Space Varying Deconvolution . . . . . 119
Experimental Results . . . . . 120
CHAPTER 7. MATERIAL CHARACTERIZATION USING KALMAN FILTER BASED DECONVOLUTION . . . . . 126
Grain Scattering . . . . . 127
Signal Processing . . . . . 128
Deconvolution . . . . . 131
Spectrum estimation . . . . . 131
Feature extraction . . . . . 132
Experimental Results . . . . . 132
Material characterization . . . . . 133
Inclusion detection . . . . . 139
CHAPTER 8. SUMMARY AND CONCLUSIONS . . . . . 145
BIBLIOGRAPHY . . . . . 150
ACKNOWLEDGMENTS . . . . . 156

# LIST OF TABLES

Table 3.1: Descriptions of ultrasonic data sets . . . . . 47

Table 4.1: System modeling performances of different order system models 78

Table 5.1: Estimation error variances for different system models and shaping filters . . . . . 104

Table 6.1: Comparison of performances of model parameter interpolation method and Wiener filter method . . . . . 122

Table 7.1: Particle sizes and average grain diameters of the titanium samples A, B and C . . . . . 133

Table 7.2: Separability measure for different window sizes . . . . . 138

# LIST OF FIGURES


Figure 1.1: General model for NDE inspection . . . . . 2

Figure 1.2: Basic ultrasonic test setup . . . . . 4

Figure 1.3: Block diagram of an ultrasonic test modeled as an LTI system 6

Figure 2.1: Block diagram of an optimal detection system using matched filter . . . . . 17

Figure 2.2: Simulated ultrasonic data . . . . . 21

Figure 2.3: Probability density functions for matched filter . . . . . 22

Figure 2.4: ROC curves for matched filter . . . . . 22

Figure 2.5: Gaussian wavelet functions . . . . . 26

Figure 2.6: Block diagram of wavelet transform based signal processing method . . . . . 28

Figure 2.7: Flow diagram of detection scheme . . . . . 29

Figure 2.8: Magnitudes of wavelet transformed signal . . . . . 30

Figure 2.9: Magnitude peaks of wavelet transformed signal . . . . . 30

Figure 2.10: Block diagram of split-spectrum processing technique . . . . 32

Figure 2.11: Probability density functions of magnitude . . . . . 36

Figure 2.12: ROC curve using magnitude . . . . . 36

Figure 2.13: Probability density functions of relative peak location . . . . 38

Figure 2.14: Probability density functions of magnitude ratio . . . . . 40
Figure 2.15: Comparison of ROC curves of wavelet transform based method and matched filter . . . . . 41

Figure 3.1: Flaw and noise signals of data set 1 . . . . . 44
Figure 3.2: Flaw and noise signals of data set 2 . . . . . 46
Figure 3.3: Mean and standard deviation of data set 1 . . . . . 49
Figure 3.4: Mean and standard deviation of data set 2 . . . . . 50
Figure 3.5: Correlation functions of data set 1 . . . . . 51
Figure 3.6: Correlation functions of data set 2 . . . . . 52
Figure 3.7: Probability plots of data set 1 . . . . . 55
Figure 3.8: Probability plots of data set 2 . . . . . 56
Figure 3.9: Wavelet transformed signals of data set 1 . . . . . 59
Figure 3.10: Wavelet transformed signals of data set 2 . . . . . 60
Figure 3.11: Comparison of ROC curves of wavelet transform based method and matched filter . . . . . 61
Figure 3.12: Perturbed flaw signals . . . . . 63
Figure 3.13: ROC curves of perturbed flaw signals . . . . . 65

Figure 4.1: Signal models . . . . . 68
Figure 4.2: Block diagram of state-space model . . . . . 69
Figure 4.3: Block diagram of Kalman filter . . . . . 74
Figure 4.4: Flow diagram of Kalman filter based deconvolution algorithm 77
Figure 4.5: Reference pulse . . . . . 79
Figure 4.6: Second-order system model . . . . . 80

Figure 4.7: Sixth-order system model . . . . . 81
Figure 4.8: Tenth-order system model . . . . . 82
Figure 4.9: Deconvolution of single reflector . . . . . 85
Figure 4.10: Deconvolution of double reflector . . . . . 87
Figure 4.11: Experimental flaw data . . . . . 89
Figure 4.12: Deconvolution of flaw data . . . . . 90
Figure 4.13: Reference pulse measured from layered material . . . . . 92
Figure 4.14: Measured data from layered material . . . . . 93
Figure 4.15: Deconvolution of measured data from layered material . . . . 94
Figure 4.16: Averaged magnitude spectrum of deconvolved data from layered material . . . . . 95

Figure 5.1: Block diagram of augmented system . . . . . 99
Figure 5.2: Flow diagram of iterative scheme . . . . . 101
Figure 5.3: Frequency responses of shaping filters . . . . . 102
Figure 5.4: Change in coefficients and error variances for 2nd order system and LPF1 . . . . . 105
Figure 5.5: Change in coefficients and error variances for 2nd order system and HPF1 . . . . . 106
Figure 5.6: Change in coefficients and error variances of 2nd order system and LPF2 . . . . . 107
Figure 5.7: Change in coefficients and error variances for 2nd order system and HPF2 . . . . . 108
Figure 5.8: Change in coefficients and error variances for 6th order system and LPF1 . . . . . 109

Figure 5.9: Change in coefficients and error variances for 6th order system and HPF1 . . . . . 110

Figure 5.10: Change in coefficients and error variances for 6th order system and LPF2 . . . . . 111

Figure 5.11: Change in coefficients and error variances for 6th order system and HPF2 . . . . . 112

Figure 6.1: Measured signals from copper samples of different thicknesses 123

Figure 6.2: Interpolated signals using 14-th order ARMA models . . . . 124

Figure 6.3: Interpolated signals using 20-th order AR models . . . . . 125

Figure 7.1: Frequency dependent scattered energies of different microstructures . . . . . 129

Figure 7.2: Flow diagram of signal processing method . . . . . 130

Figure 7.3: Experimental setup for measuring backscattered signal and reference pulse . . . . . 134

Figure 7.4: Feature vector distributions for AR (10) model . . . . . 136

Figure 7.5: Basic concept of inclusion detection . . . . . 139

Figure 7.6: Decision line of host material A and inclusion C with inclusion size of 4 mm . . . . . 143

Figure 7.7: POD performances of different host materials and inclusions (POF=0.1) . . . . . 144

# CHAPTER 1. INTRODUCTION

Nondestructive evaluation (NDE) is an interdisciplinary field whose primary task is to measure material and flaw parameters and relate these parameters to information which is useful in an engineering context. In general, the NDE problem is to detect and characterize defects in industrial parts without destroying them. A general model for the NDE problem is indicated in Figure 1.1. The device-under-test, or sample, is a physical object possibly containing one or more defects. Energy is introduced into the sample by the source. This energy interacts with the structure of the material and is observed by the detector. The goal of nondestructive evaluation is to analyze the detected energy to derive quantitative information about the structure of any flaws or defects present in the sample. A prior knowledge about the energy source, material structure, and detector response is the key to this analysis. Nearly all forms of known energy can be used for this purpose including acoustic waves (ultrasonic and acoustic emission), electromagnetic radiation (microwave, eddy currents, optics, X-rays, and gamma rays), neutrons, and thermal waves. Of these, ultrasonic energy is one of the most widely used because (1) it can be inexpensively generated and detected, (2) it can propagate deeply into the interior of many structures without excessive attenuation, and (3) the return signals have sufficient information-carrying capacity to determine important failure-related characteristics of the flaws or material

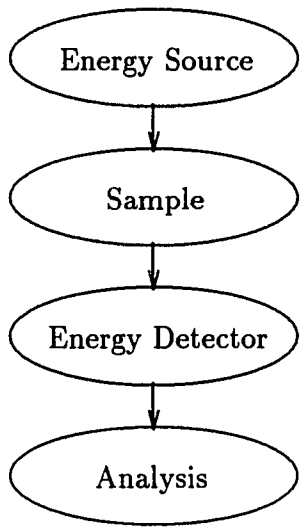


Figure 1.1: General model for NDE inspection

(Thompson and Thompson, 1985).

## Overview of Ultrasonic Testing

Ultrasonics is a branch of acoustics dealing with frequencies generally beyond the audible limit. For industrial applications, ultrasonic testing has the advantages of (1) high sensitivity permitting detection of minute discontinuities, (2) good penetrating power allowing examination of extremely thick sections, (3) accuracy in the measurement of discontinuity position and estimation of discontinuity size, (4) fast response permitting rapid and automated testing, and (5) need for access to only one surface of the test object. The primary disadvantage of ultrasonic testing is that it is adversely affected by (1) unfavorable test object geometry (size, contour, surface roughness, complexity and discontinuity orientation) and (2) undesirable internal structure (grain size, structure porosity, inclusion content or fine, dispersed

precipitates) (Birks *et al.*, 1991).

The utilization of ultrasonic waves as a means of nondestructive testing occurred in the late 1920s. Developments since the 1930s have made ultrasonics one of the most widely used nondestructive testing techniques. The rapid development of early ultrasonic NDE was aided by a contemporary growth of electronic instrumentation and technology. While the ultrasonic techniques have greatly progressed, the need to extract exact data from ultrasonics has led to the development of more quantitative testing techniques. These include the signal processing techniques which have significantly advanced the state of the art of nondestructive evaluation and testing recently. Much of the progress in recent ultrasonic signal processing has been centered on the application of digital signal processing, already successfully applied in other areas such as radar, sonar and geophysics, in order to enhance the capability of conventional NDE. The specific goals of digital signal processing in NDE are (1) to improve inspection reliability, (2) to improve flaw detection, (3) to improve flaw characterization, and (4) to generate information about material properties to assess the remaining life of a structure. Advanced signal processing techniques are needed to achieve these objectives (Chen, 1988).

Ultrasonic testing is typically performed in two ways. A beam of ultrasonic energy is directed into the test object and (1) the energy transmitted through it is measured (through-transmission method), or (2) energy reflected from discontinuities in the object is measured (pulse-echo method). A basic ultrasonic pulse-echo measurement system is shown in Figure 1.2. In this common system configuration, an electrical waveform generated by the pulser is applied to the transmitting transducer. Conversion of the electrical energy into mechanical energy occurs within the

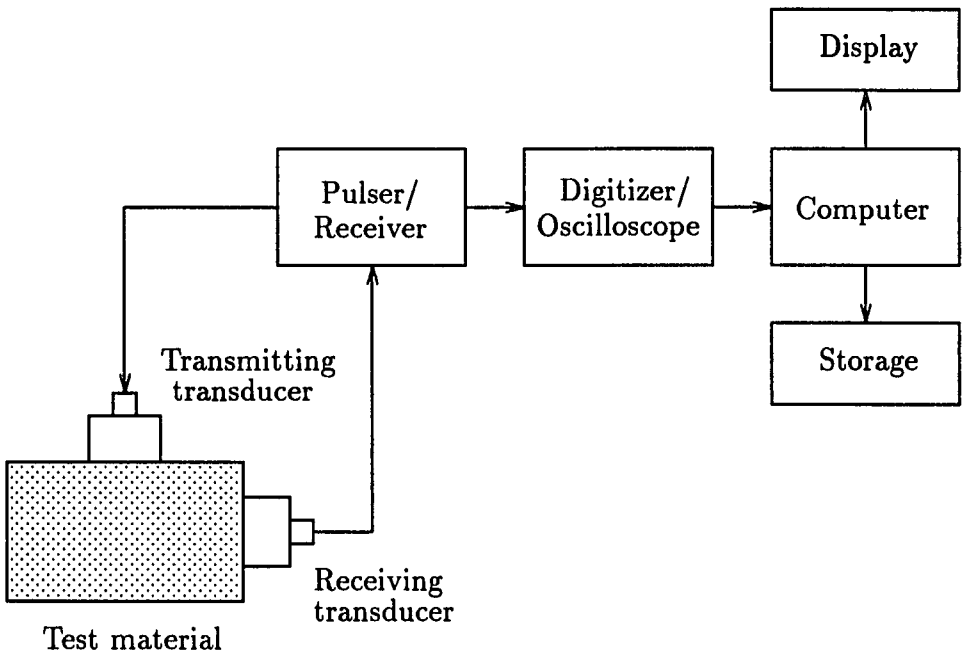


Figure 1.2: Basic ultrasonic test setup

transducer, producing an ultrasonic wave. As the wave propagates through the test material, interactions of the ultrasonic energy with the material alter the amplitude, phase, and direction of the wave. A receiving transducer intercepts a portion of this ultrasonic energy and conversion occurs from mechanical to electrical energy. Because the electrical signal is usually small, an amplifier is used to increase its amplitude. The amplified electrical signal is digitized, displayed, and stored for analysis by a computer.

A reasonable model of the ultrasonic measurement system was proposed by Frederick and Seydel (1973). They considered each component of the system as a linear time-invariant (LTI) system. Although such an assumption may not be always appropriate, it provides a good basis for assessing the performance of the system components (Fitting and Adler, 1981). The behavior of an LTI system is completely described by its impulse response (in the time domain) or its frequency response (in the frequency domain) (Oppenheim and Schafer, 1989). These two descriptions of system are equivalent. Figure 1.3 is a block diagram of an ultrasonic test modeled as an LTI system. In general, the time-domain representation of the signal is the one that is monitored. The analysis subsystem provides the transformation to the frequency domain. The independent variable inside the test material through which an ultrasonic wave propagates is distance ($z$). Distance may be converted to time if the velocity of wave travel is known. The measured signal by the receiver, $y(t)$, is represented in the time domain as

$$y(t) = x(t) * t_1(t) * p_1(t) * h(t) * p_2(t) * t_2(t), \tag{1.1}$$

where $*$ represents convolution. In Equation (1.1), $x(t)$ is the electrical impulse driving the transducer, $t_1(t)$ the transmitting transducer impulse response, $p_1(t)$ the

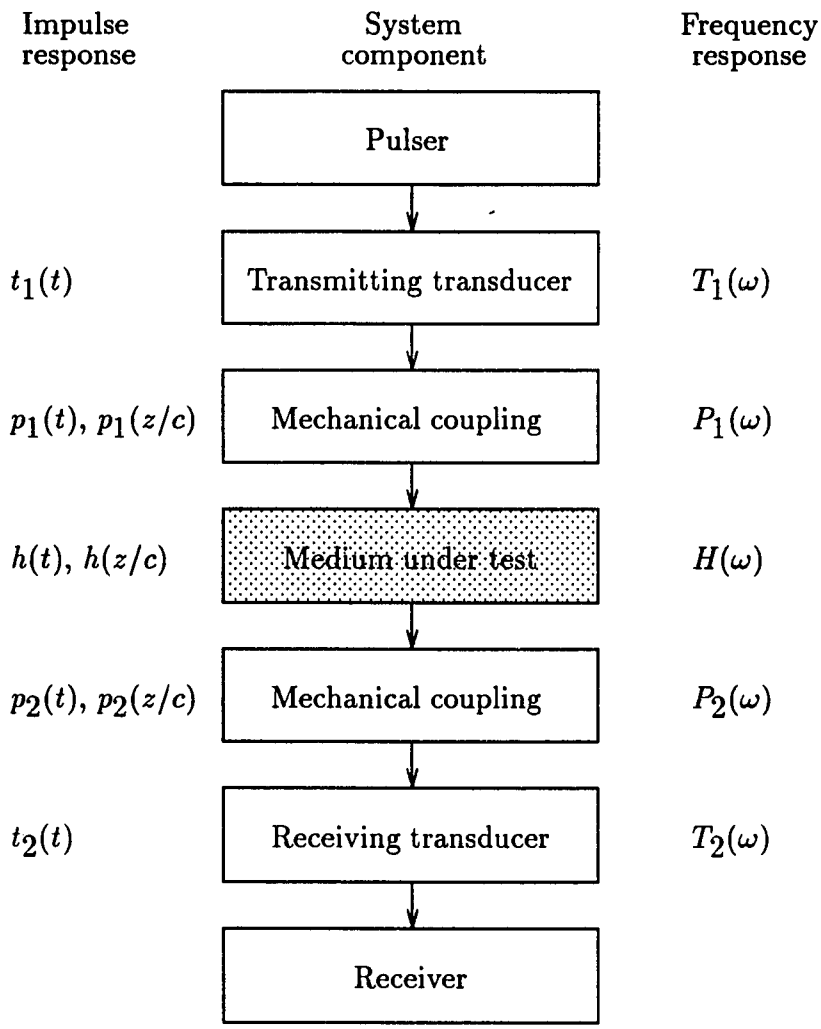


Figure 1.3: Block diagram of an ultrasonic test modeled as an LTI system

forward propagation path impulse response, $h(t)$ the impulse response of the test material, $p_2(t)$ the return propagation path impulse response, $t_2(t)$ the receiving transducer impulse response. The LTI model can be expressed in the frequency domain as

$$Y(\omega) = X(\omega)T_1(\omega)P_1(\omega)H(\omega)P_2(\omega)T_2(\omega), \tag{1.2}$$

where convolution becomes simple multiplication, and $Y(\omega)$, $X(\omega)$, $T_1(\omega)$, $P_1(\omega)$, $H(\omega)$, $P_2(\omega)$, and $T_2(\omega)$ are the Fourier transforms of $y(t)$, $x(t)$, $t_1(t)$, $p_1(t)$, $h(t)$, $p_2(t)$, and $t_2(t)$ respectively. Throughout this dissertation, the analysis of an ultrasonic system is based on this LTI model.

## Research Objective and Approach

The main motivation for this research comes from the need to find an NDE method for detecting hard alpha inclusions in titanium alloys. Hard alpha inclusions in titanium alloys are brittle regions of altered microstructure, usually caused by oxygen or nitrogen contamination. The brittleness of these inclusions can initiate cracks during manufacture or in-service use. These cracks may eventually lead to catastrophic failure of highly-stressed components, such as aircraft engine turbine disks (Costa *et al.*, 1990). Hence, it is important to be able to detect the hard alpha inclusions before the cracks form and grow. NDE techniques for hard alpha detection are currently fairly limited. Ultrasonic methods for detecting hard alpha inclusions have relied upon finding associated defects such as voids or cracks. The ultrasonic contrast for regions of hard alpha is said to be very low. Hence, relatively sophisticated signal processing are needed to distinguish the flawed regions (Rose, 1989; Ramabadran, 1990; Ramabadran *et al.*, 1991).

In order to solve hard alpha detection problem, two approaches were considered. One approach is to consider the flaw detection problem as a hypothesis testing problem. Based on this approach, a wavelet transform based signal processing method has been developed for ultrasonic flaw detection. The wavelet transform is a newly developed signal analysis tool that handles time-localized signals such as an ultrasonic flaw signal quite well. The other approach is to use material reflection coefficient sequence to distinguish hard-alpha inclusions and the host material. A Kalman filter based deconvolution algorithm has been developed to estimate the reflection coefficient sequence of a given test material. The main advantage of the Kalman filter approach is that it can be more readily applied to situations involving time-varying signals and non-stationary statistics and consequently has the potential to perform better under these situations than the Wiener filter approach.

## Research Summary and Contributions

The first part of the dissertation is concerned with the application of the wavelet transform to ultrasonic flaw detection. The wavelet transform is a newly developed signal analysis tool that handles time-localized signals such as an ultrasonic flaw signal quite well. A wavelet transform based signal processing technique has been proposed which uses only partial knowledge of the flaw signal waveform that may be obtained from a reference experiment. The detection performance of the proposed technique is found to be comparable to that of the matched filter. Although the matched filter provides excellent performance, it requires exact knowledge of the flaw signal waveform and the noise autocorrelation function. Its effectiveness diminishes if this exact knowledge is unavailable. The proposed technique based on the wavelet

transform can therefore be quite useful in situations where the flaw signal waveform is unknown or partially known.

The second part of the dissertation describes a Kalman filter based deconvolution algorithm for ultrasonic signals and its application to material characterization. The Kalman filter based deconvolution algorithm is based on state-space modeling of the ultrasonic measurement system. Since the Kalman filter can handle time-varying systems and non-stationary statistics quite naturally, it is better suited for such situations than the Wiener filter approach. In applying the Kalman filter based deconvolution algorithm, the deconvolved sequence is assumed white. However, material reflection coefficient sequences which are the deconvolved sequences in the present case are generally colored. A simple iterative scheme is proposed in this dissertation for estimating such colored sequences. The Kalman filter based deconvolution algorithm is implemented in the time-domain and can be easily modified to handle space-varying systems. We investigate in this dissertation a model parameter interpolation method to handle such space-varying systems to incorporate the effect of ultrasonic attenuation. In this dissertation, a method is also developed for material characterization through processing of grain backscattered signals. The backscattered ultrasonic signals are deconvolved and appropriate features are extracted from the deconvolved sequences for the purpose of material characterization.

The contributions of this research are summarized below.

- Wavelet transform based signal processing: A wavelet transform based signal processing technique has been developed for flaw detection. This technique does not require exact knowledge of the flaw signal waveform or the noise autocorrelation function. The detection performance of the proposed technique is

found to be comparable to that of the matched filter.

- Kalman filter based deconvolution: A Kalman filter based deconvolution algorithm has been developed for ultrasonic signals and its application to material characterization. The main advantage of the Kalman filter is that it can handle time-varying signals and non-stationary statistics more easily. It is expected that the algorithm will be useful for different applications in the NDE area.

- Colored input sequence estimation: A simple iterative scheme for estimating colored input sequence has been developed. The scheme uses the Kalman filter based deconvolution algorithm iteratively. It was observed that this scheme outperforms the straight Kalman filter deconvolution algorithm for a high-pass colored sequence.

- Space-varying deconvolution: A model parameter interpolation method was investigated to modify the Kalman filter based deconvolution algorithm such that it can handle space-varying systems. It was shown that the method yields reasonably good results.

- Material characterization and inclusion detection: A new technique for processing grain backscattered ultrasonic signals and extracting useful features from them has been developed. The features show good potential for material characterization and inclusion detection as well.

## Overview of Chapters

Chapter 2 describes a wavelet transform based signal processing method for ultrasonic flaw detection. The performance of the proposed signal processing technique

is evaluated by means of a receiver operating characteristics (ROC) curve using simulated ultrasonic data and compared with the performance of the matched filter. Chapter 3 describes the application of the wavelet transform based signal processing method to the hard-alpha detection problem. A statistical analysis of the grain noise signals is provided. The detection performance of the proposed signal processing method is evaluated for the hard-alpha detection problem and compared with the performance of the matched filter. Chapter 4 describes the Kalman filter based deconvolution algorithm. It discusses a typical ultrasonic measurement system and its signal/system model as an LTI system, and essential estimation theory for deriving the Kalman filter based deconvolution algorithm. Application examples of the Kalman filter approach are presented using simulated and actual measured ultrasonic data. Chapter 5 describes an iterative scheme for estimating colored input sequences. The colored system modeling and iterative scheme are described followed by simulation results using two different system models and four different shaping filters. Chapter 6 describes the space varying deconvolution problem. The use of a model parameter interpolation method is investigated to provide suitable correction for a space-varying system. The effectiveness of this approach is evaluated using experimentally obtained signals from copper samples of different thicknesses. Chapter 7 describes a new method developed for material characterization and inclusion detection through processing of grain backscattered signals. Experimental results involving characterization of some pure titanium samples with different grain sizes are presented. Chapter 8 summarizes the work, presents conclusions, and describes future directions for this research.

# CHAPTER 2. WAVELET TRANSFORM BASED SIGNAL PROCESSING

This chapter describes a wavelet transform based signal processing method for ultrasonic flaw detection. The wavelet transform is a recently developed signal analysis tool that can provide a time-frequency description of a given signal. An engineering interpretation of the wavelet transform is a set of bandpass filters with different center frequencies and bandwidths. In the proposed signal processing method, the received ultrasonic signal is passed through several bandpass filters with different center frequencies but with the same bandwidth. The magnitude peaks of the filtered signals are then used in the detection process. Two types of features are extracted from these peaks: (1) relative peak location and (2) magnitude ratio with respect to one of the filtered signals regarded as reference. The performance of the proposed method is evaluated using simulated ultrasonic data. It is shown that the detection performance achieved is close to that of the matched filter.

In the following, an overview of the ultrasonic flaw detection problem and current signal processing techniques for flaw detection are given. This is followed by a description of the matched filter technique which is an optimal filter if the flaw signal waveform and the autocorrelation function of grain noise are exactly known. The proposed wavelet transform based signal processing is then described. Under certain

assumptions, the probability distributions of the selected features are derived. Finally, the performance of the proposed technique is evaluated by means of a receiver operating characteristics (ROC) curve using simulated ultrasonic data and compared with the performance of the matched filter. In this chapter, we develop the signal processing method using simulated grain noise data. In the next chapter, the proposed method will be applied to actual grain noise data.

## Ultrasonic Flaw Detection

When an ultrasonic wave is propagating through a material, it produces a scattered wave by interacting with any defects in the material. It also produces a scattered signal due to material texture such as porosity, grain boundaries, and dislocations. This scattered signal is called background clutter or grain noise. Moreover, testing at high frequencies to increase resolution tends to amplify the grain noise. The grain noise reduces the signal-to-noise ratio (SNR) of the measured signal from flaws and results in unreliable detection, especially when the flaw size is small in relation to the size of the grains in the material.

Time-averaging of the return echoes and correlation methods have been used conventionally to reduce the effects of backscattered noise (Furgason *et al.*, 1975; Lee and Furgason, 1981). The main objective of these techniques is to obtain a set of decorrelated grain noise signals by collecting the ultrasonic data from different locations of the transducer (spatial diversity). However, it is not possible to reduce the grain noise using these methods if the grain noise signals are correlated or enough sample signals are not available. An alternative signal decorrelation method uses frequency diversity. This technique called split-spectrum processing (SSP) was intro-

duced by Bilgutay *et al.* in the late seventies and has been used for the purpose of SNR enhancement in ultrasonic signal detection (Bilgutay *et al.*, 1979; Newhouse *et al.*, 1982). This technique suppresses the grain noise by using a number of bandpass filters the outputs of which are uncorrelated. For strong scatterers (such as flat-bottom holes), which possess higher reflectivity and a characteristic spectrum that is distinct from that of grain noise, this method has been shown to work well (Yue and Chong-Fu, 1987). For very weak flaw signals, this technique is very sensitive to the parameter settings which are usually difficult to obtain a priori in practice.

A matched filter is a linear filter designed to provide the maximum signal-to-noise ratio at its output for a given signal waveform. It has been widely used in the area of communications for signal detection in noise. The effectiveness of the matched filter technique for ultrasonic flaw detection was studied by Chiou *et al.* (1993a, 1993b). This technique relied on a model-based technique which assumed the existence of a priori signal models. The detection performance of the matched filter is maximized, if the flaw signal waveform and autocorrelation function of additive noise are exactly known. However, its effectiveness diminishes if the flaw signal waveform and the noise autocorrelation function are not reasonably well known.

Another approach to the detection of signals in noise is Fourier analysis or spectral estimation. This technique works best if the signal to be detected has spectral features that clearly distinguish it from the noise. Its advantage over correlation and matched filter methods is its insensitivity to the shape or time of occurrence of the desired signal. It is not well adapted to the detection of time-localized signals whose exact waveform is unknown. The fundamental problem with ordinary spectral analysis is that the basis functions of Fourier analysis, viz., sinusoidal functions, extend

over infinite time and are therefore poorly matched to the short-time transients of interest. An obvious method for dealing with short-time or nonstationary signals is to use Fourier analysis with a sliding time window. This is referred to as time-windowed Fourier transform. A major disadvantage of the time-windowed Fourier transform is that the window function is fixed and therefore as the frequency is increased, more and more cycles are included inside the window; hence all frequency components of the signal are not treated in the same way by the time-windowed Fourier transform.

Some of the problems of the time-windowed Fourier transform are avoided in the recently proposed wavelet transform (Morlet *et al.*, 1982; Morlet, 1983; Grossmann and Morlet, 1984). The wavelet transform technique is relatively new and has found applications in different fields such as image analysis, communication systems, biomedical imaging, radar, air acoustics, theoretical mathematics, control systems, and other signal processing areas. The advantage of the wavelet transform is its ability to use different windows at different frequencies. The wavelet transform looks at a given signal with high frequency resolution at lower frequencies and high time resolution at higher frequencies. Several ways of detecting transient signals using the wavelet transform are described in Tuteur (1988), Petropulu (1992), and Frisch and Messer (1992).

## Hypothesis Testing

Mathematically, the received ultrasonic signal can be expressed as the summation of flaw and noise signals:

$$x(t) = s(t) + v(t), \tag{2.1}$$

where $x(t)$ represents the measured signal, $s(t)$ represents the flaw signal, and the noise is represented by $v(t)$. In general, the signal $s(t)$ is not completely known. The noise $v(t)$ has zero mean and an autocorrelation function represented by $R(i,j)$. It is not necessarily white or Gaussian.

In statistics, the flaw detection problem is referred to as hypothesis testing and is described below.

$$H_0 : \quad x(t) = v(t) \tag{2.2}$$

$$H_1 : \quad x(t) = s(t) + v(t) \tag{2.3}$$

The null hypothesis $H_0$ is the event that no flaw is present and the alternative hypothesis $H_1$ is the event that a flaw is present. Based on the measured signal $x(t)$, we must choose between these hypotheses. Sometimes we can improve detection performance by processing the signal $x(t)$ through a signal processing method such as linear or nonlinear filtering and signal correlation. In this case, the output of the signal processing, $y(t)$, is called a *test statistic.* When the flaw signal waveform and the noise autocorrelation function are known, the optimal signal processing method is the well-known matched filter. Our primary goal in this research is to design a new signal processing method which does not require exact knowledge of the flaw signal waveform and the noise autocorrelation function.

There are many criteria for making decisions using the test statistic $y(t)$. When $H_0$ is true and we choose $H_1$ instead, the resulting error is called *false alarm.* Similarly, when $H_1$ is true and we choose $H_0$, the error is called *miss.* In the communications area, where both types of errors are assumed to be of equal importance and the a priori probabilities of the two hypotheses are known, the criterion of minimum error probability is generally used. In the NDE flaw detection problem, however, the

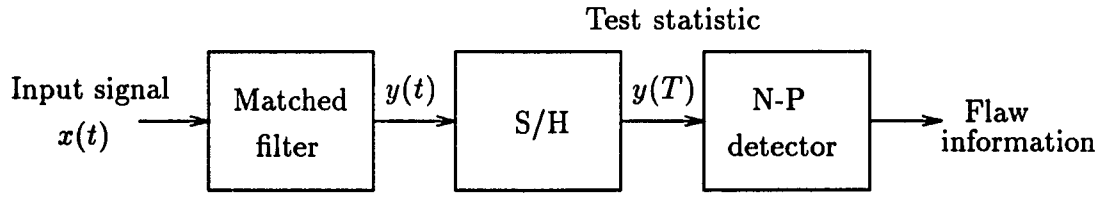


Figure 2.1: Block diagram of an optimal detection system using matched filter

a priori probabilities are difficult to determine. For such cases, the Neyman-Pearson criterion is widely used. Its objective is to maximize the probability of detection (POD) for a given probability of false alarm (POF). The POD and POF are defined as follows.

$$\text{POD} = \int_{\eta}^{\infty} f_1(y)\,dy \tag{2.4}$$

$$\text{POF} = \int_{\eta}^{\infty} f_0(y)\,dy, \tag{2.5}$$

where $\eta$ is the threshold used at the output of the system, i.e., if $y(t) > \eta$, we choose $H_1$, and $f_0(y)$ and $f_1(y)$ are conditional probability density functions of $y$ under null and alternative hypotheses respectively.

### Signal Detection Using Matched Filter

A block diagram of an optimal detection system using the matched filter is illustrated in Figure 2.1. The input signal is denoted by $x(t)$ and the output signal by $y(t)$. In applying a matched filter, the flaw signal $s(t)$ is assumed to be completely known which extends over the time interval $(0, T)$. The autocorrelation function of the additive noise $v(t)$ is also known. In the case of a matched filter, the processing is done by a linear filter. The test statistic is the output sample at time $T$.

The generalized matched filter that maximizes signal-to-noise ratio for non-white noise can be derived as follows. The outputs of the filter at time $T$ under null and alternative hypotheses are

$$H_0: \quad y(T) = \sum_i h(T-i)v(i) \tag{2.6}$$

$$H_1: \quad y(T) = \sum_i h(T-i)s(i) + \sum_i h(T-i)v(i), \tag{2.7}$$

where $h(t)$ is the impulse response of the matched filter. From Equations (2.6) and (2.7), the signal and noise components are easily identified as

$$S(T) = \sum_i h(T-i)s(i) \tag{2.8}$$

$$N(T) = \sum_i h(T-i)v(i). \tag{2.9}$$

The mean and variance of $N(T)$ are

$$\begin{aligned} E\{N(T)\} &= E\Big\{\sum_i h(T-i)v(i)\Big\} \\ &= \sum_i h(T-i)E\{v(i)\} \\ &= 0 \end{aligned} \tag{2.10}$$

$$\begin{aligned} V\{N(T)\} &= E\Big\{\sum_{i,j} h(T-i)h(T-j)v(i)v(j)\Big\} \\ &= \sum_{i,j} h(T-i)h(T-j)E\{v(i)v(j)\} \\ &= \sum_{i,j} h(T-i)h(T-j)R(i,j), \end{aligned} \tag{2.11}$$

where $R(i,j)$ is autocorrelation function of $v(t)$, $E\{\cdot\}$ denotes expectation, and $V\{\cdot\}$ denotes variance.

There are many definitions of an engineering parameter called signal-to-noise ratio (SNR) which is the ratio of the signal power to the noise power. Here, we define

it as the ratio of the peak signal power to the average noise power. This is expressed as

$$\text{SNR} = \frac{S(T)}{\sqrt{V\{N(T)\}}} \tag{2.12}$$

at the filter output. The optimal filter that maximizes the SNR of the test statistic $y(T)$ is the solution of the equation (Whalen, 1971),

$$\sum_j h(T-j)R(i,j) = s(i). \tag{2.13}$$

Clearly, the determination of the optimal linear filter $h(t)$ through Equation (2.13) requires the knowledge of the flaw signal waveform and the autocorrelation function of the noise. If the noise signal $v(t)$ is white Gaussian with unity variance, then its autocorrelation function $R(i,j)$ is

$$R(i,j) = \delta(i-j), \tag{2.14}$$

where $\delta(i-j)$ is Kronecker delta function which is equal to one if $i$ and $j$ are equal, and to zero in other cases. Then, the optimal filter that satisfies Equation (2.13) is

$$h(t) = s(T-t). \tag{2.15}$$

Equation (2.15) shows that the impulse response of the optimal filter for the white noise case is simply the known signal that is reversed in time. Thus, the filter is said to be matched to the signal.

### Detection Performance of Matched Filter

The performance of the matched filter was tested using simulated ultrasonic signals which were generated by adding Gaussian noise to an actual ultrasonic flaw

signal. The flaw signal and an example of the simulated signal (flaw+noise) are shown in Figure 2.2. In testing the matched filter, the ultrasonic signal SNR was set at 10 dB.

As discussed in the previous section, the matched filter is a *linear filter* which maximizes the output signal SNR. So, if the matched filter input $x(t)$ is Gaussian, the output $y(t)$ is also Gaussian. The probability density functions of test statistic $y(T)$ under the null and alternative hypotheses can be expressed as

$$H_0: \quad y(T) \sim N(0, \sigma^2) \tag{2.16}$$

$$H_1: \quad y(T) \sim N(m, \sigma^2). \tag{2.17}$$

These conditional probability density functions of $y(T)$ under null and alternative hypotheses are shown in Figure 2.3. In Equation (2.17), the mean of the test statistic under the alternative hypothesis $m$ is computed as

$$m = \sum_i s^2(i). \tag{2.18}$$

The detection performance of the matched filter can be evaluated in terms of the probability of detection and the probability of false alarm. Figure 2.4 shows the detection performance of the matched filter using the Neyman-Pearson detector. This figure showing the probability of detection versus the probability of false alarm with signal SNR as a parameter is referred to as the receiver operating characteristics (ROC) curve. The point plots were obtained experimentally using a Monte Carlo simulation (100 trials).

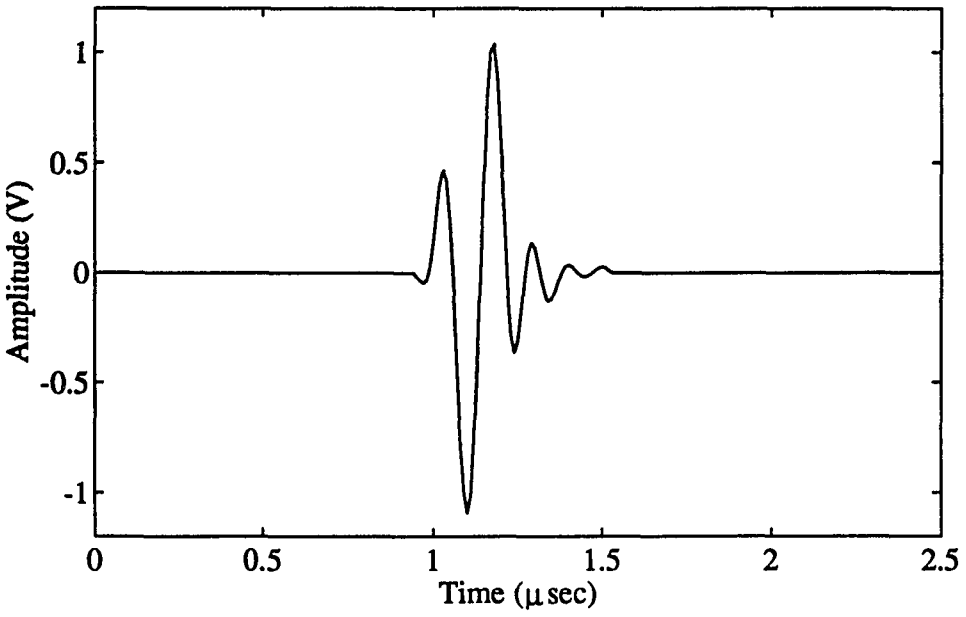


(a)

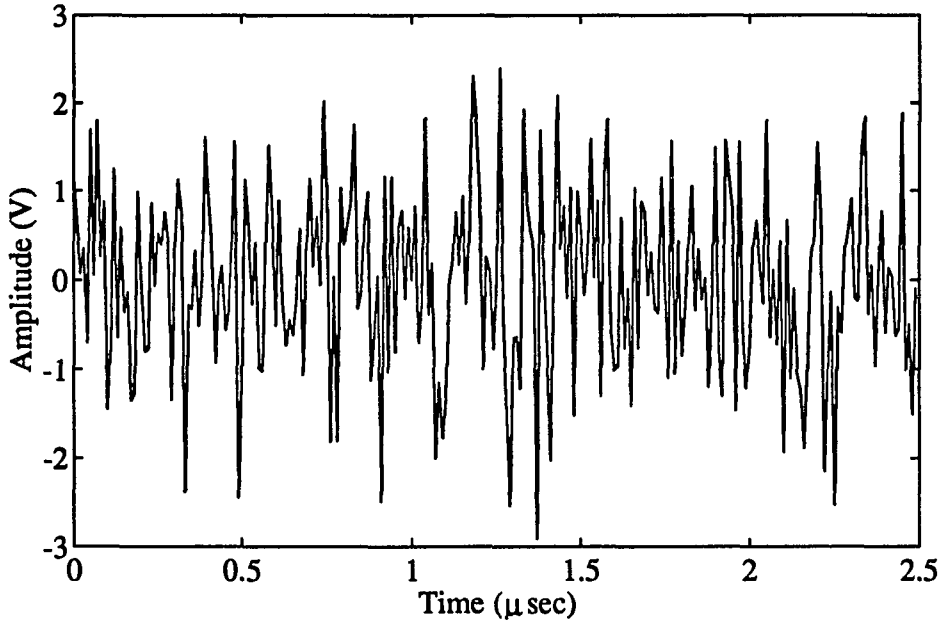


(b)

Figure 2.2: Simulated ultrasonic data: (a) flaw signal, (b) noise plus flaw signal (SNR = 10 dB)

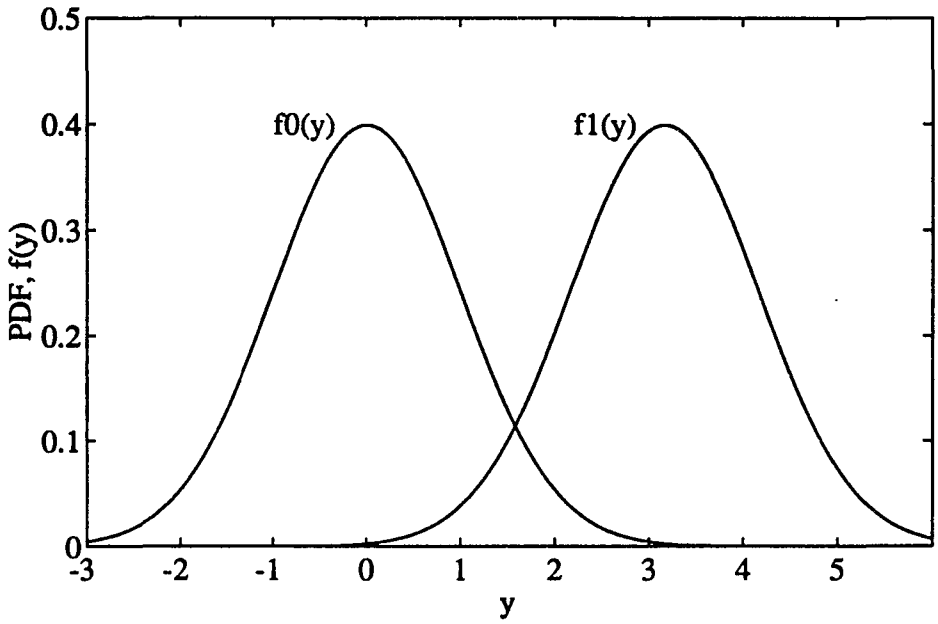


Figure 2.3: Probability density functions for matched filter

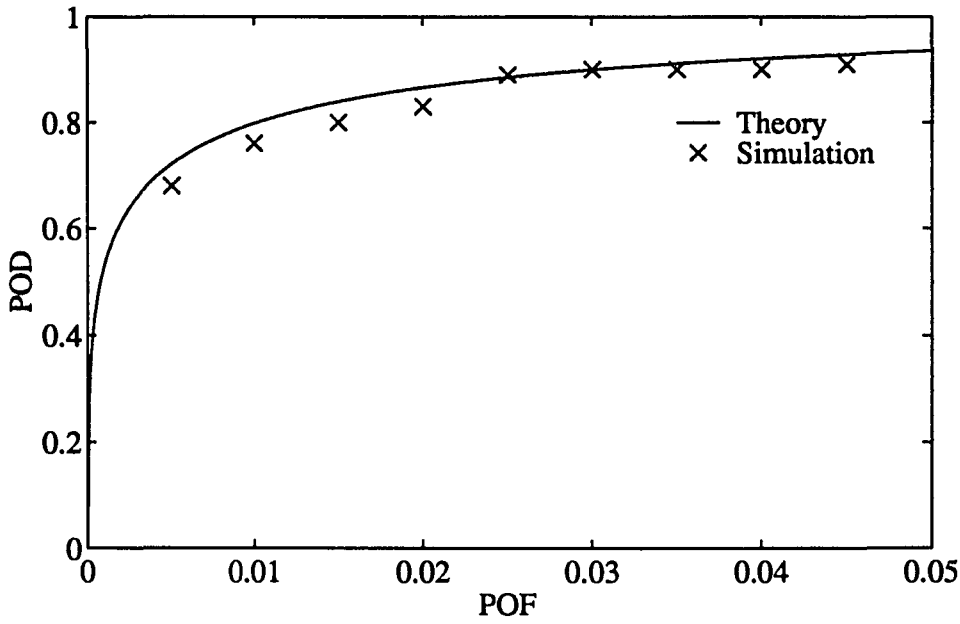


Figure 2.4: ROC curves for matched filter

## Wavelet Transform Based Signal Processing

This section describes the wavelet transform and the proposed signal processing method for ultrasonic flaw detection.

### Wavelet transform

The wavelet transform of a signal $x(t)$ is given by

$$W_x(a,b) = \int x(t)\,\psi^{a,b}(t)\,dt, \tag{2.19}$$

where the family of functions $\psi^{a,b}(t)$ derived from $\psi(t)$ through dilations and translations is referred to as *wavelets* and expressed as

$$\psi^{a,b}(t) = \frac{1}{\sqrt{a}}\,\psi\left(\frac{t-b}{a}\right), \tag{2.20}$$

where the parameters $a > 0$ and $b$ are real. The function $\psi(t)$ is called the *mother wavelet* and is typically localized in time $t$. It also satisfies the condition that $\int \psi(t)\,dt = 0$. This means that $\psi(t)$ has some oscillations. In fact, $\psi(t)$ can be viewed as the impulse response of a bandpass filter. The wavelets are useful in analyzing any arbitrary (square integrable) signal $x(t)$. The translation parameter $b$ shifts the function $\psi(t)$ to the right ($b > 0$) or the left ($b < 0$) thereby permitting the analysis of different parts of $x(t)$. The dilation parameter $a$ compresses ($a < 1$) or expands ($a > 1$) the function $\psi(t)$ thereby permitting the analysis of $x(t)$ at different scales or resolutions. If we interpret $\psi(t)$ as the impulse response of a bandpass filter with center frequency $\omega_C$, then values of $a < 1$ and $a > 1$ shift $\omega_C$ to higher and lower values respectively. The bandwidth $B$ of the filter also changes (inversely) with $a$ thereby maintaining a constant $Q = \omega_C/B$ of the filter.

The wavelet transform of a given signal $x(t)$ is a mapping of $x(t)$ into a two-dimensional function $W_x(a,b)$, where the values of $W_x(a,b)$ are obtained by performing the inner products of $x(t)$ with the wavelets $\psi^{a,b}(t)$. Using $W_x(a,b)$, the signal $x(t)$ can be expressed as a linear combination of the wavelets $\psi^{a,b}(t)$. Thus, the wavelet transform permits a decomposition of $x(t)$ in terms of the wavelets. If the mother wavelet $\psi(t)$ satisfies some mild conditions, the parameters $a$ and $b$ need only take discrete values for the above decomposition to work. The discrete form of wavelet transform (2.19) can be obtained by restricting $a$, $b$ to only discrete values: $a = a_0^m$ and $b = nb_0a_0^m$, where $m$ and $n$ are integers. In this case, we have a discrete wavelet transform (DWT) given by

$$W_x(m,n) = \frac{1}{\sqrt{a_0^m}} \sum_k x(k)\, \psi(a_0^{-m}k - nb_0). \tag{2.21}$$

Typical choices for $a_0$ and $b_0$ are 2 and 1 respectively. Using these values for $a$ and $b$, the wavelets in Equation (2.20) can be expressed as

$$\psi^{m,n}(t) = \frac{1}{\sqrt{2^m}} \psi(2^{-m}t - n). \tag{2.22}$$

The values $W_x(m,n)$ are referred to as the discrete wavelet transform coefficients. If we consider the set of points in the $(a, b)$ plane at which the discrete wavelet transform is computed, viz., $a = 2^m$ and $b = n2^m$, and associate the scale parameter $a$ with the reciprocal of frequency and the translation parameter $b$ with time, we notice that the frequency resolution improves as the frequency decreases and the time resolution improves as the frequency increases. In fact, the orthonormal wavelet basis and the discrete wavelet transform provide a time-varying, octave-band frequency analysis of the given signal $x(t)$.

The wavelet function must satisfy a number of restrictions. The most important are integrability and square integrability. Also the low-frequency behavior of $\psi(t)$ must be such that

$$\int \frac{\hat{\psi}(\omega)}{|\omega|}\, d\omega < \infty, \tag{2.23}$$

where $\hat{\psi}(\omega)$ is the Fourier transform of $\psi(t)$ and $\omega$ is the frequency. This condition implies that if $\hat{\psi}(\omega)$ is a smooth function in the neighborhood of the frequency origin then $\hat{\psi}(0) = 0$, i.e., $\psi(t)$ has no DC component. Additional assumptions are often made about wavelet functions for convenience. One such requirement is that $\hat{\psi}(\omega) = 0$ for $\omega < 0$. It is also convenient to assume that $\psi(\omega)$ is real for $\omega > 0$. Another requirement of wavelets is that they should be concentrated in the time and frequency domains as much as possible. This means that the time-bandwidth product for wavelets should be as small as possible. It is well known that the smallest time-bandwidth product is achieved by the modulated Gaussian wavelet function. The modulated Gaussian wavelet is the function that is proposed by Morlet (Daubechies, 1992). Its Fourier transform is a shifted Gaussian, adjusted slightly so that $\hat{\psi}(0) = 0$,

$$\hat{\psi}(\omega) = \pi^{-1/4} \left[ \exp\left\{ -(\omega - \omega_0)^2/2 \right\} - \exp\left(-\omega^2/2\right) \exp\left(-\omega_0^2/2\right) \right], \tag{2.24}$$

$$\psi(t) = \pi^{-1/4} \left[ \exp\left(-i\omega_0 t\right) - \exp\left(-\omega_0^2/2\right) \right] \exp\left(-t^2/2\right). \tag{2.25}$$

For $\omega_0 > 5$, the second term in Equation (2.25) is so small that it can be neglected in practice. The parameter $\omega_0$ is related to the center frequency of wavelet function. This function is shown in Figure 2.5 with various parameter values.

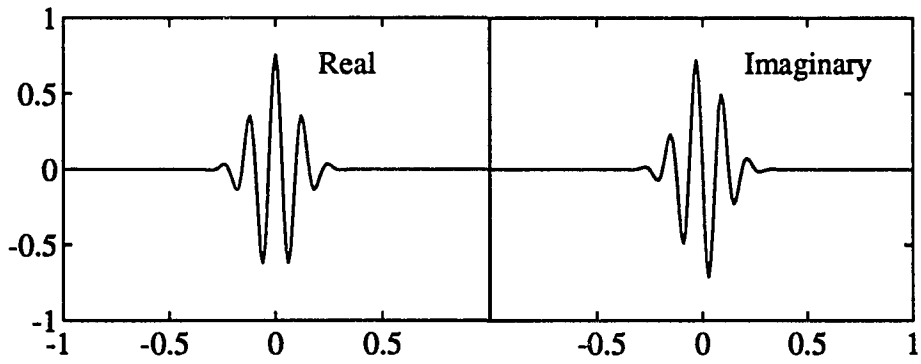


(a)

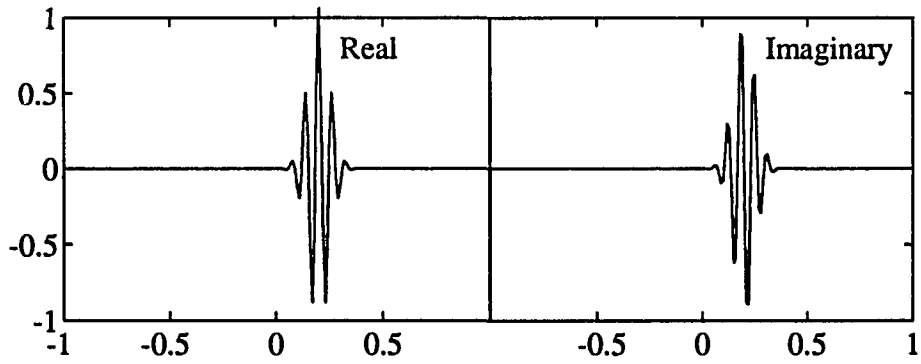


(b)

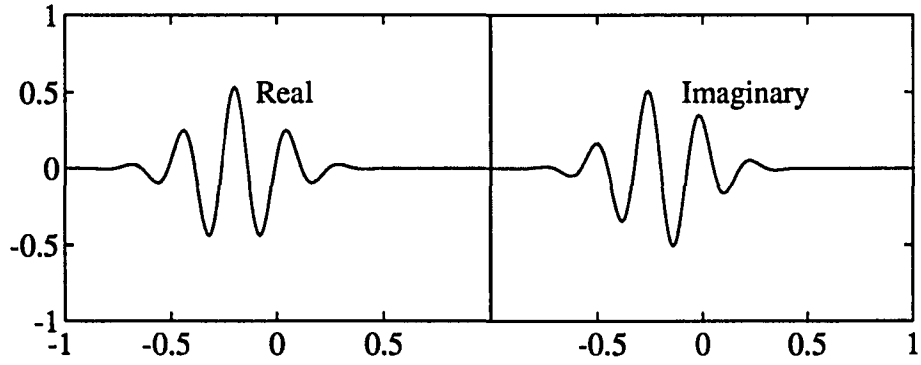


(c)

Figure 2.5: Gaussian wavelet functions: (a) $\psi(t)$, (b) $\psi^{a,b}(t)$ with $a < 1$ and $b > 0$, (c) $\psi^{a,b}(t)$ with $a > 1$ and $b < 0$

## Proposed signal processing method

The proposed wavelet transform based signal processing method is illustrated in Figure 2.6. The proposed signal processing method is motivated by the fact that one wide-band signal can be partitioned into many independent narrow-band signals, and these signals are statistically independent and can be used for output signal SNR enhancement. An engineering interpretation of the wavelet transform is a set of bandpass filters with different center frequencies and bandwidths. In the proposed signal processing method, the received ultrasonic signal $x(t)$ is passed through several bandpass filters with different center frequencies but with the same bandwidth. Figure 2.8 shows the magnitudes of filtered signals of the input signal shown in Figure 2.2 (b). The input signal was passed through three bandpass filters with center frequencies of 4, 6.35, and 8.7 MHz. In order to enhance the detection performance, some points which are less probable to be flaws than other points can be removed from the magnitudes of filtered signals. We assume that peak points are much more probable to be flaws than the other points. The magnitude peaks of the filtered signals are used in the detection process. Since the peak location of a flaw may be shifted due to additive noise, we may not get exact flaw location information from magnitude peaks and we may not even detect some flaws. By processing magnitude peaks, we can enhance the probability of detection at low probability of false alarm. This is very important because the probability that such a point is a flaw is very low in ultrasonic NDE. Figure 2.9 shows the magnitude peaks of the filtered signals shown in Figure 2.8. From the magnitude peaks of the filtered signal, two types of features are extracted: (1) relative peak location and (2) magnitude ratio with respect to one of the filtered signals regarded as reference. The center frequency of

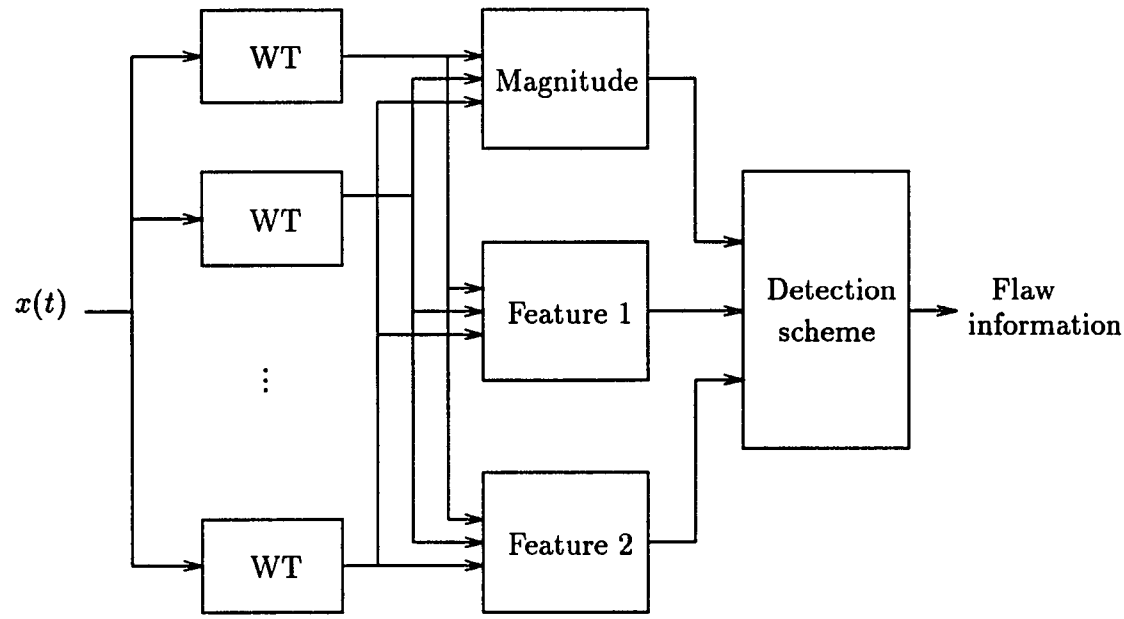


Figure 2.6: Block diagram of wavelet transform based signal processing method

the reference bandpass filter can be determined from a partial knowledge of the flaw signal waveform which may be obtained from a reference experiment.

The detection scheme used in the proposed signal processing method is illustrated in the Figure 2.7. The detection method is based on hypothesis testing described in the preceding sections. The main test statistics are the magnitudes of filtered signals with different center frequencies. The extracted features, relative peak location and magnitude ratio, are used to enhance the detection performance of the system. The scheme operates as follows. First, the magnitude vector of filtered signals $\mathbf{M}$ is compared with a threshold $\boldsymbol{\eta}$. If the magnitude vector exceeds the threshold, it is decided that there is a flaw. If the magnitude does not exceed the threshold, the feature vectors, $\mathbf{F}_1$ and $\mathbf{F}_2$ are tested and if both feature vectors are

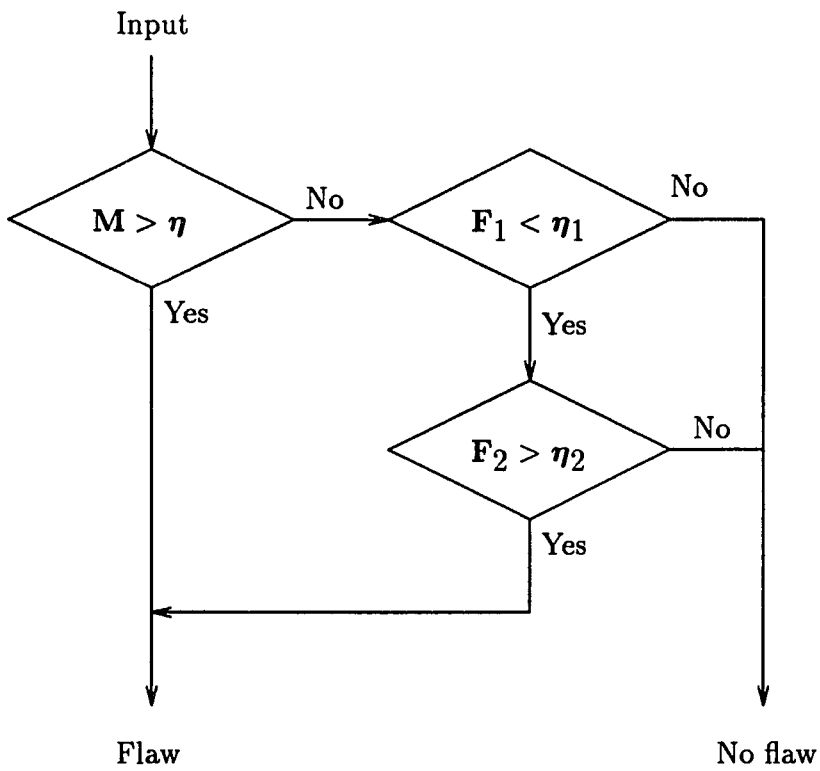


Figure 2.7: Flow diagram of detection scheme

within the thresholds $\eta_1$ and $\eta_2$ respectively, it is decided that there exists a flaw. All other situations are flagged as no flaw. The thresholds $\eta$, $\eta_1$ and $\eta_2$ may be determined from reference experiments and a priori knowledge of the ultrasonic test.

### Comparison with split-spectrum processing (SSP)

Split-spectrum processing (SSP) was introduced in the late seventies in an attempt towards implementing frequency agility techniques used in radar for signal-to-noise ratio (SNR) improvement of ultrasonic signals. The frequency diverse signals in ultrasound are produced by splitting the frequency spectrum of the received signal

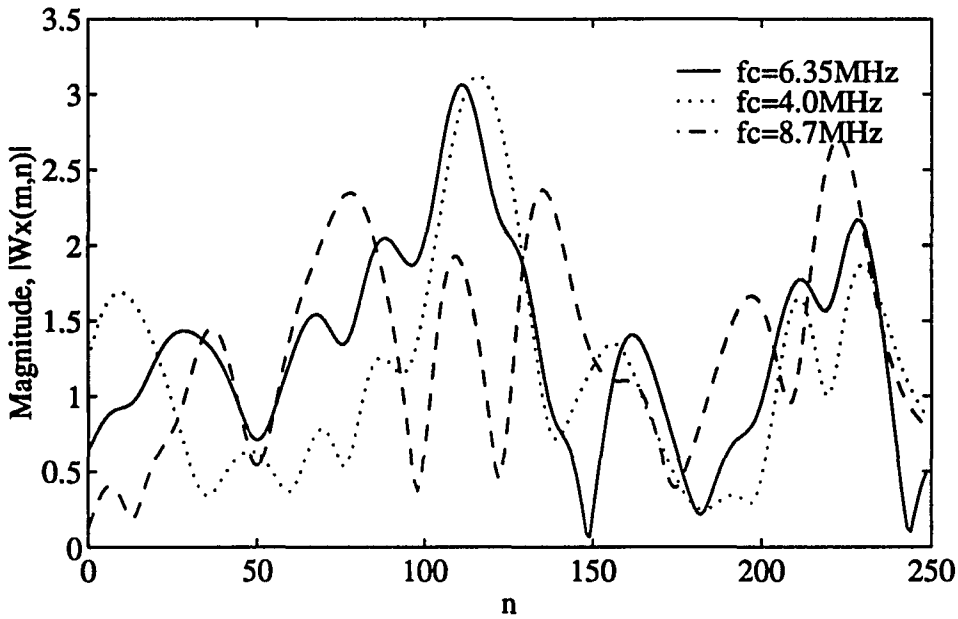


Figure 2.8: Magnitudes of wavelet transformed signal

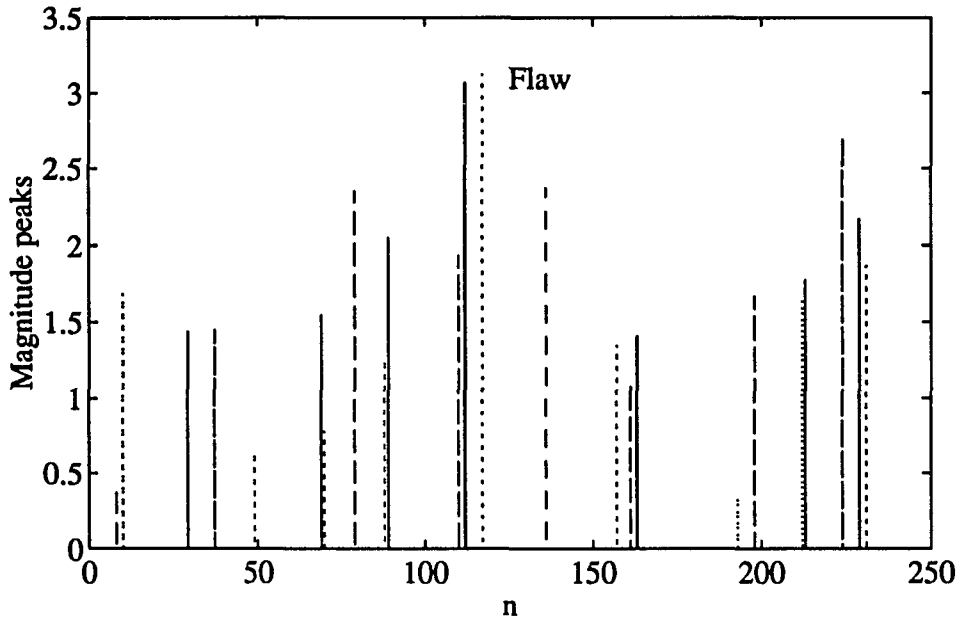


Figure 2.9: Magnitude peaks of wavelet transformed signal

instead of transmitting signals at different frequencies as is the case in radar applications. The frequency diverse signals obtained by splitting the spectrum of the received signal are uncorrelated from one another. As a result, when these signals are processed using various algorithms, the SNR can be improved.

The block diagram of the split-spectrum technique is shown in Figure 2.10. The split-spectrum technique obtains the spectrum of the received signal, $x(t)$, by a fast Fourier transform (FFT), divides the spectrum into the desired number of bands by means of digital filtering, and finally inverse Fourier transforms each band to obtain the frequency diverse signal set. Filtering is usually accomplished by Gaussian-shaped windows that have a selectable bandwidth $b$ and a fixed frequency spacing $\Delta f$. The center frequencies of the resulting signals range within the half-power bandwidth of the transducer. The resulting set of frequency diverse signals are then processed to enhance flaw visibility. The frequency diverse signals obtained from the split spectrum technique are further processed using a variety of techniques such as linear averaging, nonlinear averaging, minimization and so on.

The split-spectrum technique described above and the proposed signal processing technique using wavelet transform are similar in terms of signal processing algorithms. The main difference between the techniques is the signal which is used for flaw detection. SSP technique uses the time-domain signal processed from frequency diverse signals for flaw detection. The proposed signal processing technique uses features extracted from the wavelet transformed signals. The wavelet transform based signal processing technique is much simpler to implement than the SSP technique, because the signal processing technique does not require the inverse wavelet transform. For very weak flaw signals, SSP technique is very sensitive to processing parameters such

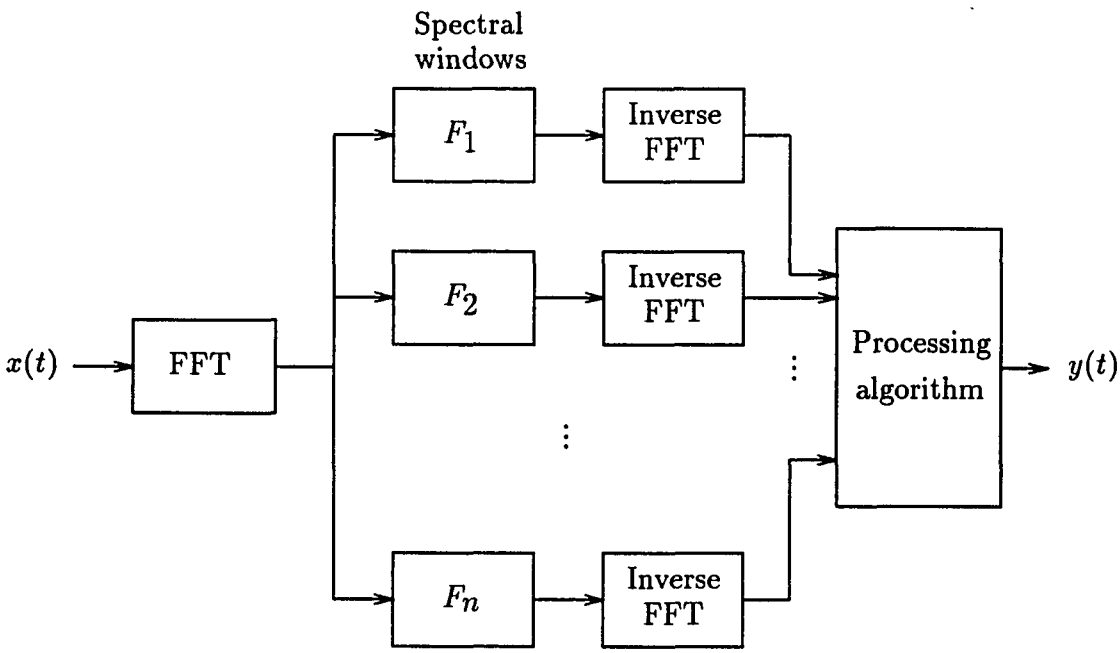


Figure 2.10: Block diagram of split-spectrum processing technique

as the number of filters used for the spectral splitting, the filter bandwidth, and the frequency separation between the adjoining filters. These parameters are usually difficult to obtain a priori in practice. The proposed signal processing technique is less sensitive to these parameters, because it uses several features which may have different sensitivities to different parameters.

## System Performance Evaluation

The performance of the proposed signal processing technique was evaluated by means of an ROC curve using simulated ultrasonic data and compared with the performance of the matched filter. Before we present the results, we justify the usefulness of the selected features, by deriving the probability distributions of the selected features under certain assumptions.

### Magnitude of wavelet transform

Since the wavelet transform is a linear transform, if the input signal is Gaussian, the transformed signal is also Gaussian. The wavelet transform of the measured signal $x(t)$ can be expressed as

$$\begin{aligned} H_0: \quad W_x(n) &= W_v(n) \\ &= R_v + jI_v \end{aligned} \tag{2.26}$$

$$\begin{aligned} H_1: \quad W_x(n) &= W_s(n) + W_v(n) \\ &= (R_s + R_v) + j(I_s + I_v), \end{aligned} \tag{2.27}$$

where $(R_v, I_v)$ and $(R_s, I_s)$ are the real and imaginary components of the wavelet transforms of noise and flaw signal respectively.

The probability density function under the null hypothesis can be determined as follows. If the noise is assumed Gaussian, the real and imaginary components of the noise wavelet transform, $R_v$ and $I_v$, are also Gaussian with each having zero-mean and variance $\sigma^2$. If we assume that they are uncorrelated at any particular instant, then, their joint density function is

$$f(R_v, I_v) = \frac{1}{2\pi\sigma^2} \exp\left[\frac{\left(R_v^2 + I_v^2\right)}{-2\sigma^2}\right]. \tag{2.28}$$

We now define a new variable which is the magnitude of the wavelet transform.

$$M = \sqrt{R_v^2 + I_v^2} \tag{2.29}$$

From Equations (2.28) and (2.29), the probability density function for $M$ can be derived as

$$f_0(M) = \frac{M}{\sigma^2} \exp\left(-\frac{M^2}{2\sigma^2}\right), \quad M \geq 0, \tag{2.30}$$

which is the well-known Rayleigh distribution.

In order to determine the probability density function under the alternative hypothesis, we denote the real and imaginary components of the wavelet transform of the flaw signal as

$$R_s = A\cos\theta, \quad I_s = A\sin\theta, \tag{2.31}$$

where $A$ and $\theta$ are the magnitude and phase of wavelet transform of flaw. Then the magnitude is

$$M = \sqrt{(A\cos\theta + R_v)^2 + (A\sin\theta + I_v)^2}. \tag{2.32}$$

Let us define the new variables

$$M_x = A\cos\theta + R_v, \quad M_y = A\sin\theta + I_v. \tag{2.33}$$

For any given value of $\theta$, both $M_x$ and $M_y$ are Gaussian variables and may be shown to be uncorrelated. Furthermore, for a given value of $\theta$, the means and variances of $M_x$ and $M_y$ are

$$E\{M_x\} = A\cos\theta \tag{2.34}$$

$$E\{M_y\} = A\sin\theta \tag{2.35}$$

$$V\{M_x\} = V\{M_y\} = \sigma^2. \tag{2.36}$$

Then, the joint probability density function of $M_x$ and $M_y$ conditioned on the $\theta$ is

$$f(M_x, M_y) = \frac{1}{2\pi\sigma^2}\exp\left\{-\frac{1}{2\sigma^2}\left[(M_x - A\cos\theta)^2 + (M_y - A\sin\theta)^2\right]\right\}. \tag{2.37}$$

From Equations (2.32), (2.33) and (2.37), the probability density function of the wavelet transform under the alternative hypothesis is

$$f_1(M) = \frac{M}{\sigma^2}\exp\left[-\frac{1}{2\sigma^2}\left(M^2 + A^2\right)\right] I_0\left(\frac{AM}{\sigma^2}\right), \tag{2.38}$$

where

$$I_0(z) \equiv \frac{1}{2\pi}\int_0^{2\pi} e^{z\cos\theta}d\theta \tag{2.39}$$

is the modified Bessel function of the first kind of zero order. This density function is referred to as Rician. It is sometimes called as the generalized Rayleigh.

Two conditional probability density functions under the null and alternative hypotheses, $f_0(M)$ and $f_1(M)$, are shown in Figure 2.11 when scale parameter $m = 3$ and input signal SNR is 10 dB. Actually, $f_1(M)$ is a special case of $f_0(M)$ when $A = 0$. Figure 2.12 shows the POD performance using a single wavelet transform and the Neyman-Pearson detection criterion. The single wavelet transform shows worse detection performance than matched filter, because the wavelet transform did not use the complete flaw signal information as the matched filter did.

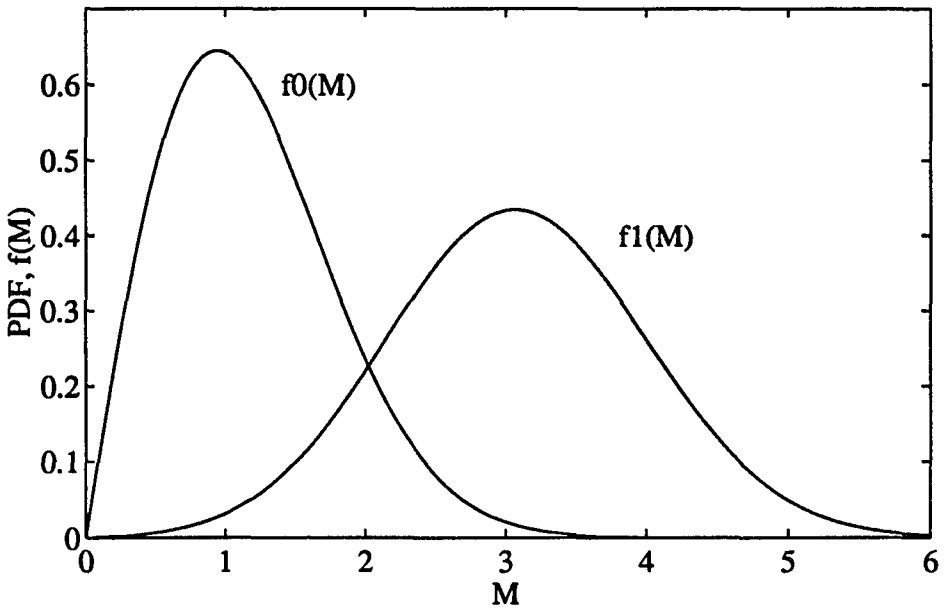


Figure 2.11: Probability density functions of magnitude

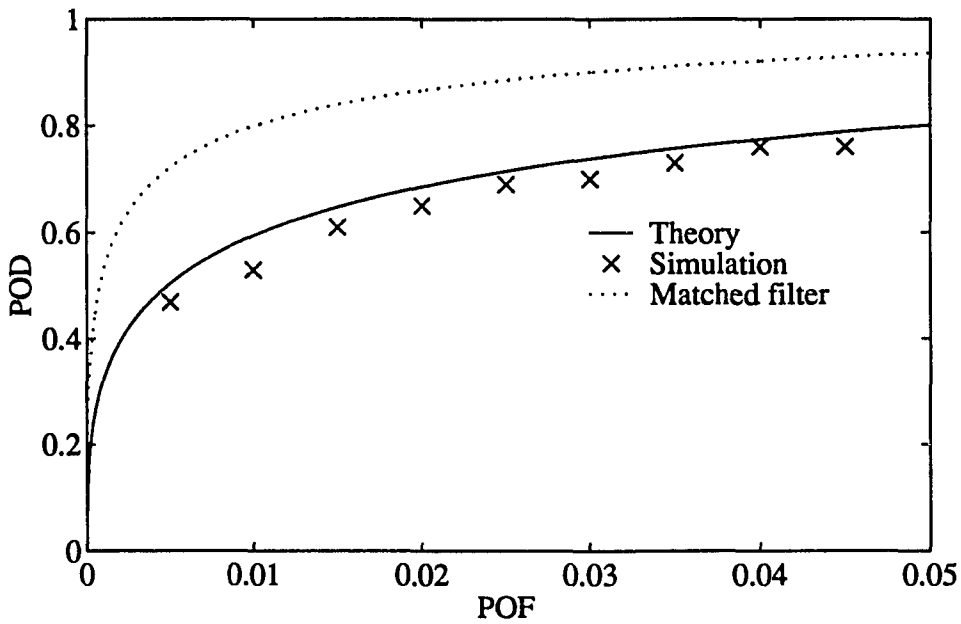


Figure 2.12: ROC curve using magnitude

### Relative peak location

The relative peak location indicates the relative distance between the peaks of a transformed signal and the peaks of the reference signal. It is closely related to the phase shift of wavelet transformed signals in the frequency domain. The relative peak location is expressed as a random process and assumed to be Gaussian distributed. The probability density functions of peak locations under null and alternative hypotheses, $f_0(P)$ and $f_1(P)$ are plotted in Figure 2.13. The probability density functions were determined from simulated data and fitted into Gaussian functions. Figure 2.13 shows that density functions of relative peak locations have common means and uncommon variances, and their most probable peak location is at $P = 0$. Figure 2.13 shows that the relative peak location feature has extra information to distinguish the null and alternative hypotheses and can be used for detection performance enhancement.

### Magnitude ratio

Another feature extracted from the magnitude peaks of the filtered signals is magnitude ratio. This is the ratio of reference magnitude to the magnitude of filtered signal. The distribution of this feature can be determined by assuming that the magnitudes and phases of wavelet transforms are statistically independent. In the frequency domain, the wavelet transforms can be considered as bandpass filters that have different center frequencies. If all wavelet functions do not overlap in the frequency domain, the magnitudes of the wavelet transforms will be independent and Rayleigh distributed as shown in the previous section, and phases will be uniformly distributed between 0 and $2\pi$.

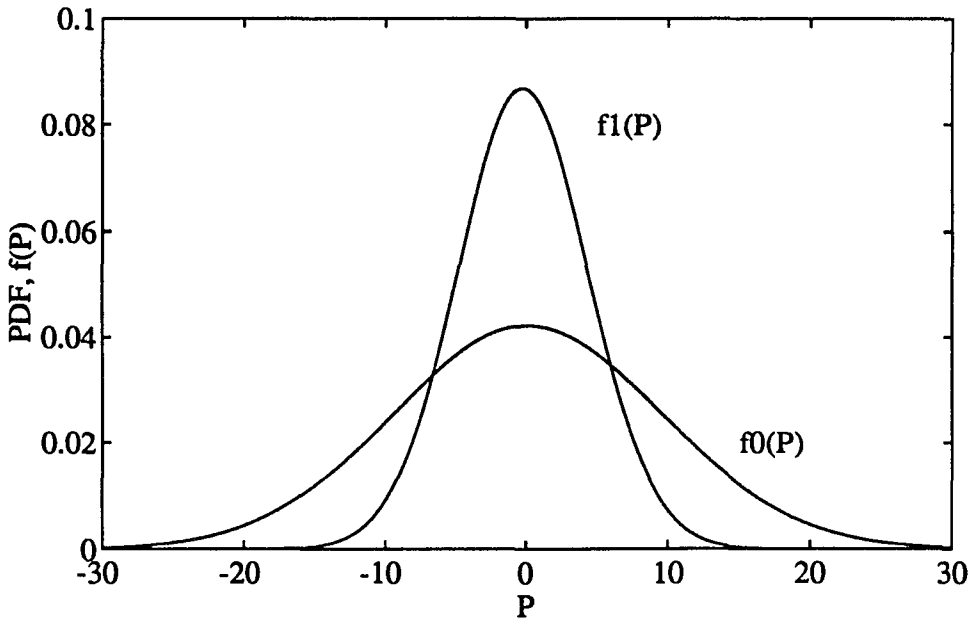


Figure 2.13: Probability density functions of relative peak location

Under the null hypothesis, the magnitude ratio to the reference peak magnitude is expressed as a new random variable

$$R = \frac{X}{Y}, \tag{2.40}$$

where the two random variables $X$ and $Y$ are the reference magnitude and magnitude of the filtered signal. Because random variables $X$ and $Y$ are independent, their joint probability density is

$$g(X,Y) = g_1(X)g_2(Y), \tag{2.41}$$

where the probability density functions $g_1(X)$ and $g_2(Y)$ are Rayleigh distributions

$$g_1(X) = \frac{X}{\sigma_1^2}\exp\left(-\frac{X^2}{2\sigma_1^2}\right) \tag{2.42}$$

$$g_2(Y) = \frac{Y}{\sigma_2^2}\exp\left(-\frac{Y^2}{2\sigma_2^2}\right). \tag{2.43}$$

We choose a second arbitrary variable as

$$Z = X. \tag{2.44}$$

Then, using Equations (2.40), (2.41) and (2.44), probability density function of $R$ is determined as

$$f(R) = \int |Z| \, g_1\left(\frac{R}{Z}\right) g_2(Z) \, dZ. \tag{2.45}$$

Under the alternative hypothesis, the random variables $X$ and $Y$ are Rician distributed as shown in the previous section.

$$g_1(X) = \frac{X}{\sigma_1^2} \exp\left[-\frac{1}{2\sigma_1^2}\left(X^2 + A_1^2\right)\right] I_0\left(\frac{A_1 X}{\sigma_1^2}\right) \tag{2.46}$$

$$g_2(Y) = \frac{Y}{\sigma_2^2} \exp\left[-\frac{1}{2\sigma_2^2}\left(Y^2 + A_2^2\right)\right] I_0\left(\frac{A_2 Y}{\sigma_2^2}\right), \tag{2.47}$$

where $A_1$ and $A_2$ are wavelet transforms of flaw signal at different center frequencies. The probability density function of $R$ under the alternative hypothesis can be solved from Equations (2.45), (2.46) and (2.47). The probability density functions of the magnitude ratio under null and alternative hypotheses, $f_0(R)$ and $f_1(R)$ are plotted in Figure 2.14 for a given flaw signal and input signal SNR of 10 dB. Figure 2.14 shows that the magnitude ratio feature has extra information to distinguish the null and alternative hypotheses and can be used for detection performance enhancement.

### Overall system performance

The proposed wavelet transform based signal processing method was implemented in software using MATLAB and tested using simulated ultrasonic data. In generating simulated data, an actual ultrasonic flaw signal was added to Gaussian random noise signals. In testing the proposed method, the ultrasonic signal SNR

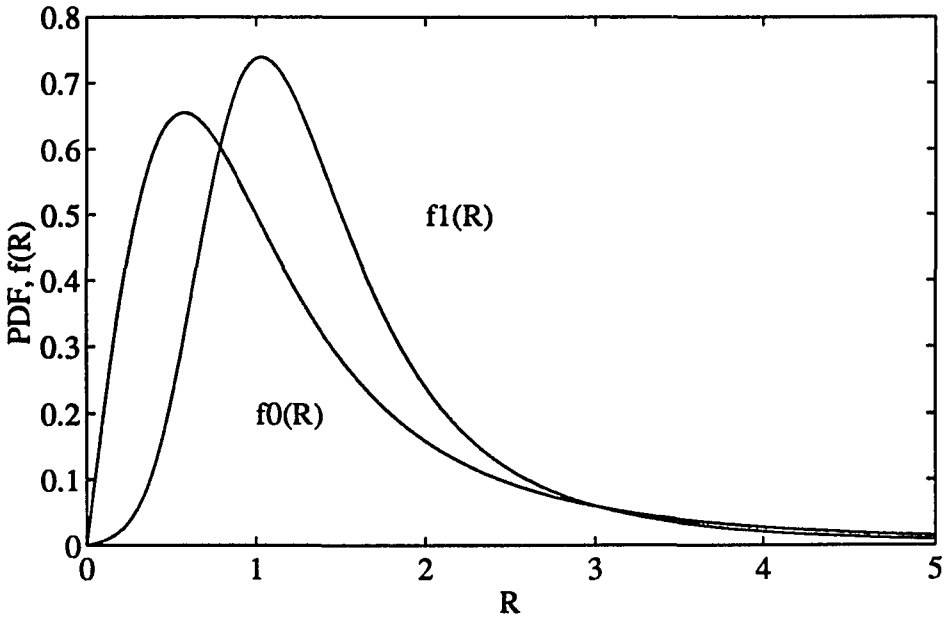


Figure 2.14: Probability density functions of magnitude ratio

was set at 10 dB. The wavelet transform was carried out as the inner product of the input signal and the Gaussian wavelet function shown in Figure 2.5. The scale parameter $m$ was fixed as 3 and the center frequencies were chosen as 4, 6.35, and 8.7 MHz from the a priori knowledge of the flaw signal bandwidth and maximum energy frequency which may be obtained from a reference experiment. Figure 2.15 shows the ROC curve of the proposed signal processing method. The proposed signal processing method shows very similar detection performance as the matched filter. When the POF is bigger than 0.03, the POD of the proposed method is a little lower than the POD performance of the matched filter. This occurs because the wavelet transform based signal processing loses some peaks of flaws during peak detection. This means we can not improve the POD by increasing the POF. However, in an actual application, the POF is very small and at this operating point, the wavelet

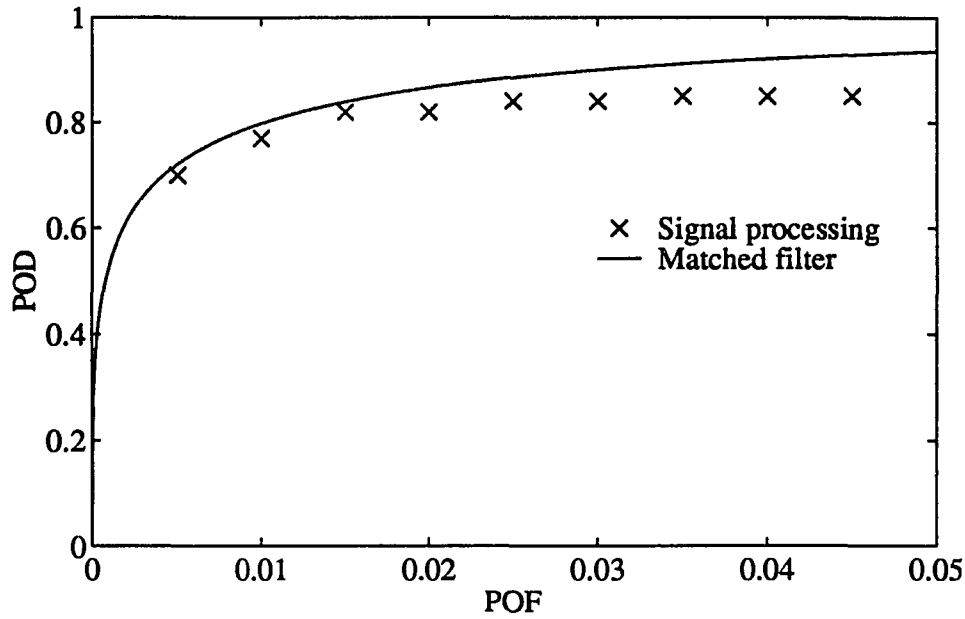


Figure 2.15: Comparison of ROC curves of wavelet transform based method and matched filter

transform based signal processing method shows almost equal performance as that of the matched filter without using exact information about the flaw signal waveform.

# CHAPTER 3. APPLICATION OF THE WAVELET TRANSFORM BASED SIGNAL PROCESSING METHOD TO THE HARD-ALPHA DETECTION PROBLEM

In this chapter, we describe the application of the wavelet transform based signal processing method developed in the preceding chapter to the hard-alpha detection problem. Hard alpha inclusions represent brittle regions in titanium alloy materials that arise from high oxygen or nitrogen concentration. When components made of titanium alloy material, e.g. fan disks in aircraft engines, are subjected to stress, the hard-alpha inclusions may lead to cracks and the eventual failure of the components. Detection of these inclusions is therefore an important NDE problem. In order to study the effectiveness of the wavelet transform based signal processing method in solving the hard-alpha detection problem, two data sets were prepared. Because of the difficulty in preparing samples containing actual hard-alpha inclusions, the flaw signals were simulated. The grain noise signals, however, were obtained from an actual titanium sample. The detection performance of the wavelet transform based signal processing method was evaluated using the receiver operating characteristics (ROC), i.e., POD versus POF, curves. In the following, we first describe the two data sets. Next, a statistical analysis of the grain noise signals is provided. Finally, the detection performance of the proposed signal processing method is evaluated for the

hard-alpha detection problem and compared with the performance of the matched filter.

## Ultrasonic Data Sets

Two sets of ultrasonic data were prepared for studying the hard-alpha detection problem (Chiou *et al.*, 1993a). Important details regarding these data sets are given in Table 3.1. The flaw signals for each data set was obtained theoretically using the Thompson-Gray measurement model (Thompson and Gray, 1982). This model incorporates in its calculations attenuation, beam spreading, interface transmission, and flaw scattering amplitude. The measurement system response is introduced in the model through a separate reference experiment. For simplicity, a spherical inclusion and a flat front surface (of the specimen) were assumed in the simulations. The grain noise data were measured from a typical Ti-6426 alloy block with moderate noise. Each signal in the data sets was obtained by adding the corresponding simulated flaw signal to the actual noise data at the appropriate location. More details about the data set generation can be found in Chiou *et al.* (1993a). In order to test the wavelet transform based signal processing technique for different SNR's, the flaw signals of data set 1 were obtained for three different inclusion sizes. Figures 3.1 and 3.2 illustrate the flaw signals and a grain noise signal from data sets 1 and 2, respectively.

## Statistical Analysis of Noise Signals

In order to understand and characterize the grain noise data, statistical analysis of the data was performed. We consider the ultrasonic noise signals measured at $N$

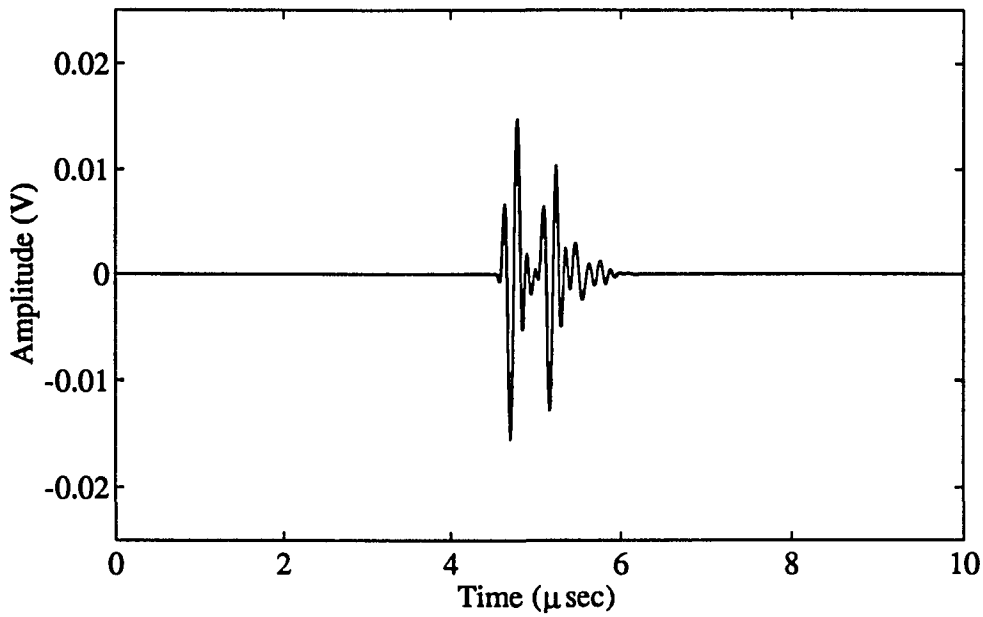


(a)

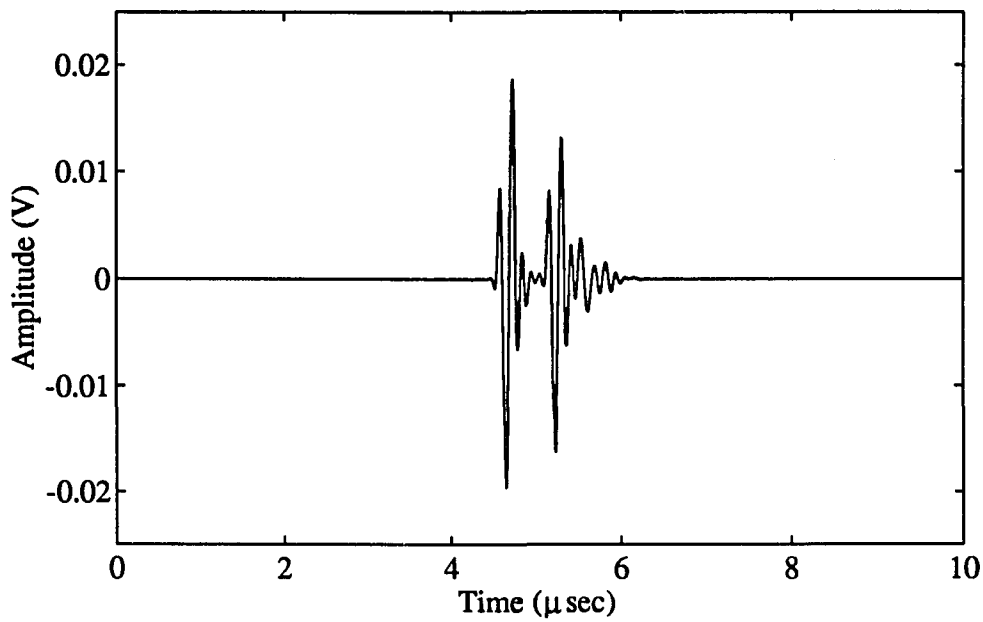


(b)

Figure 3.1: Flaw and noise signals of data set 1: (a) flaw size = 0.8 mm, (b) flaw size = 1 mm, (c) flaw size = 1.2 mm, (d) noise signal

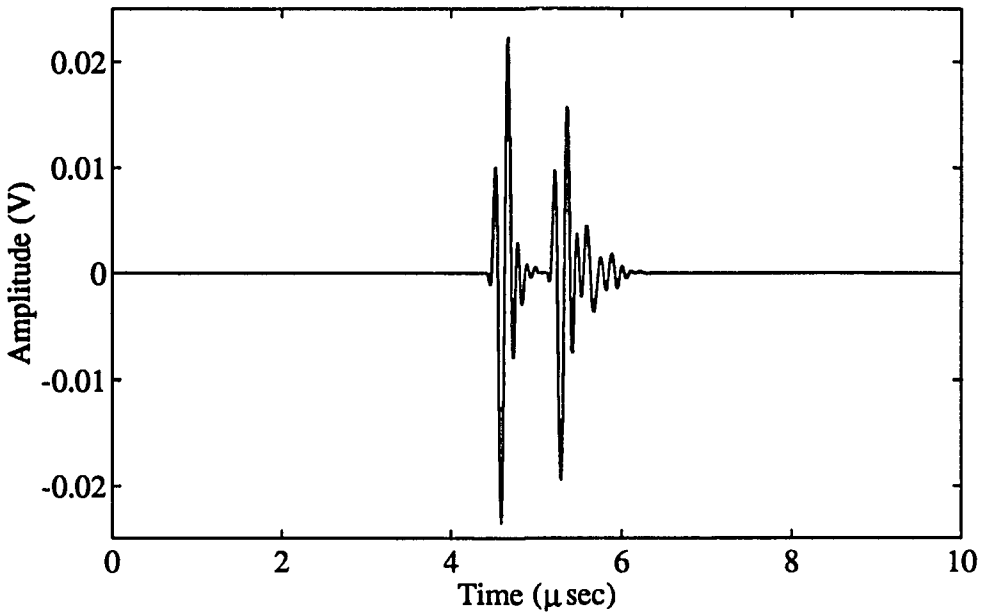


(c)

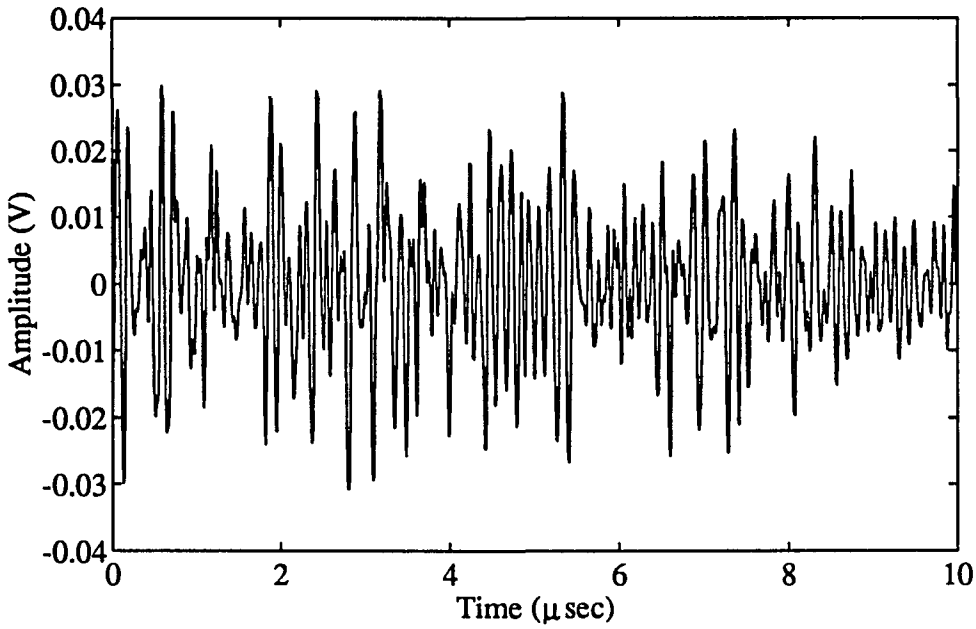


(d)

Figure 3.1 (Continued)

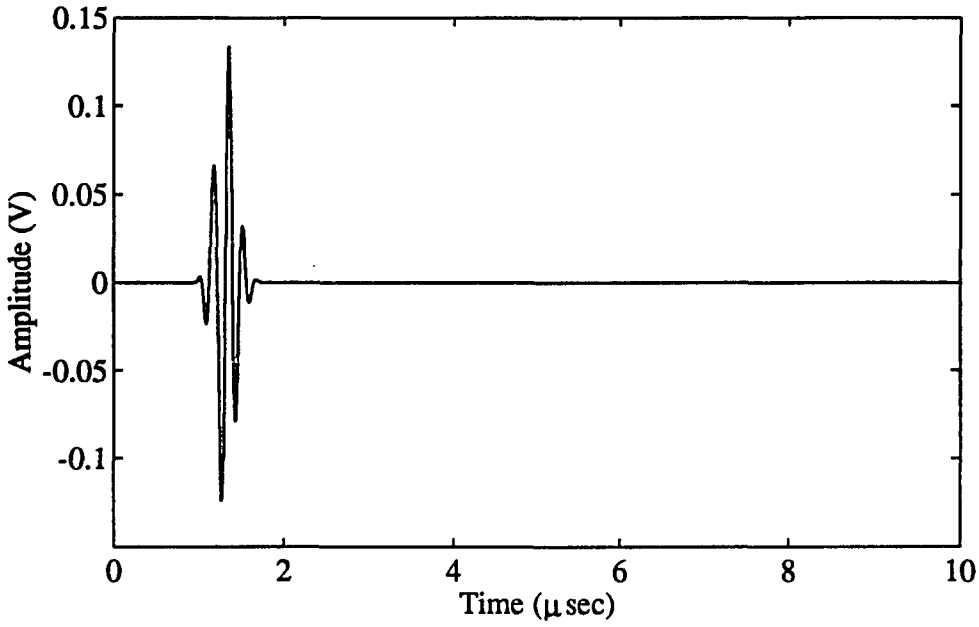


(a)

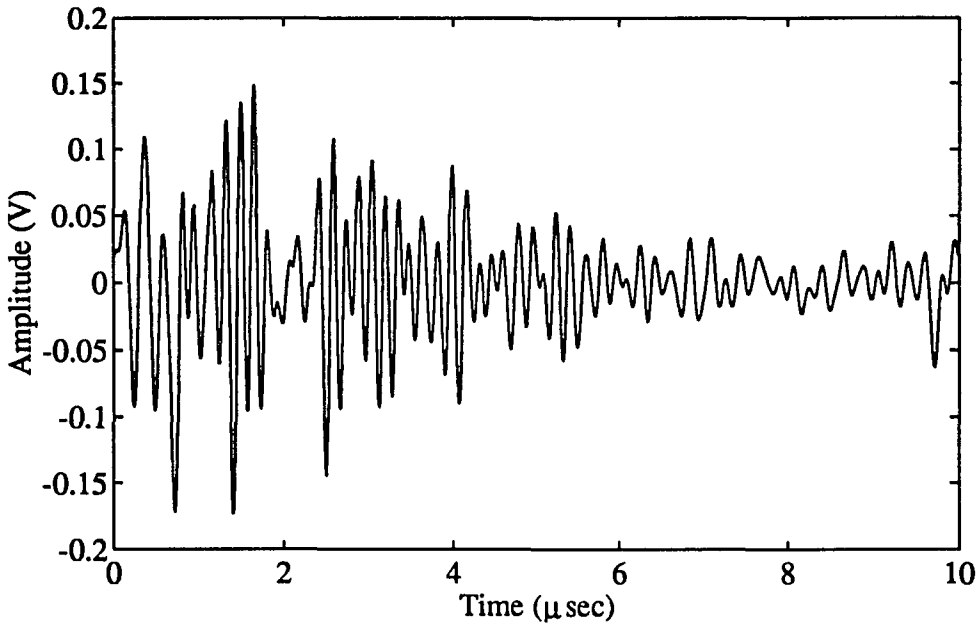


(b)

Figure 3.2: Flaw and noise signals of data set 2: (a) flaw signal, (b) noise signal

Table 3.1: Descriptions of ultrasonic data sets

| Description | Data set 1 | Data set 2 |
|---|---|---|
| Number of signals in the data set | 100 | 231 |
| Number of samples in each signal | 1000 | 1000 |
| Inclusion signal | simulated | simulated |
| Inclusion diameter (mm) | 0.8, 1, 1.2 | 0.4 |
| Inclusion impedance difference | high | low |
| Noise signal | real | real |
| Average input SNR (dB) | −5.82, −3.78, −2.21 | −2 |
| Transducer frequency (MHz) | 10 | 5 |
| Transducer type | planar 0.25" dia. | focused 0.5" dia., $F = 2$" |

different positions, $v_i(t)$ $(i = 1, 2, \cdots, N)$, as different realizations of a noise random process. At a particular time $t$, $v_i(t)$ then represents a random variable whose amplitude varies over the measurement position $i$. In general, ultrasonic noise decays with time, primarily due to attenuation and diffraction, and is therefore not time-invariant (Stanke and Kino, 1984). This can be shown by considering the mean and standard deviation as a function of time for the ensemble of signals. To compute the mean and standard deviation, each signal was divided into 20 segments with each segment containing 50 sample points. The mean for the $j$-th segment can be written as

$$\bar{m}_j = \frac{1}{N} \sum_i \left[ \frac{1}{50} \sum_k v_i(k) \right], \tag{3.1}$$

where $N$ is the total number of measurement positions. Also, assuming that the mean of each segment is zero, the standard deviation for the $j$-th segment can be written as

$$\bar{\sigma}_j = \sqrt{\frac{1}{N} \sum_i \left[ \frac{1}{50} \sum_k v_i^2(k) \right]}. \tag{3.2}$$

Figures 3.3 and 3.4 show the mean and standard deviation of data set 1 and 2 for each segment as a function of time. The straight lines with zero ordinate value are shown only for reference purposes. The standard deviation of data set 1 which was measured using a planar transducer shows the decaying nature as expected. The standard deviation of data set 2 which was measured using focused transducer shows an obvious focusing effect as well as a decaying trend.

The correlation functions of the noise signals were also plotted. The correlation function of the $k$-th signal shifted by $\tau$ relative to the $i$-th signal can be written as

$$\rho_{k,i}(\tau) = \frac{\sum_t v_k(t) v_i(t+\tau)}{\sqrt{\sum_t v_k^2(t) \sum_t v_i^2(t)}}, \tag{3.3}$$

where $k = i$ means the correlation of a signal with itself which is referred to as an autocorrelation function. Equation (3.3) is a normalized measure of the degree of correlation between two noise signals, $v_k(t)$ and $v_i(t)$ (Brown, 1983). A sample average, $\bar{\rho}(\tau)$, can be determined by averaging over a number of signal combinations,

$$\bar{\rho}(\tau) = \frac{1}{N-c} \sum_k \rho_{k,k+c}(\tau), \tag{3.4}$$

where $c = 0$ specifies the average autocorrelation, and $c = 1$ specifies the average crosscorrelation between successive signals (i.e., 1 with 2, 2 with 3, etc.). Figures 3.5 and 3.6 show the average autocorrelation and crosscorrelation ($c = 1$) functions of data sets 1 and 2 for 200 shifts in each direction. The autocorrelation plots show periodic time-correlations. Thus, the noise signals of data sets 1 and 2 are non-white. The crosscorrelation plots indicate that the the noise signals measured at adjacent measurement positions are uncorrelated.

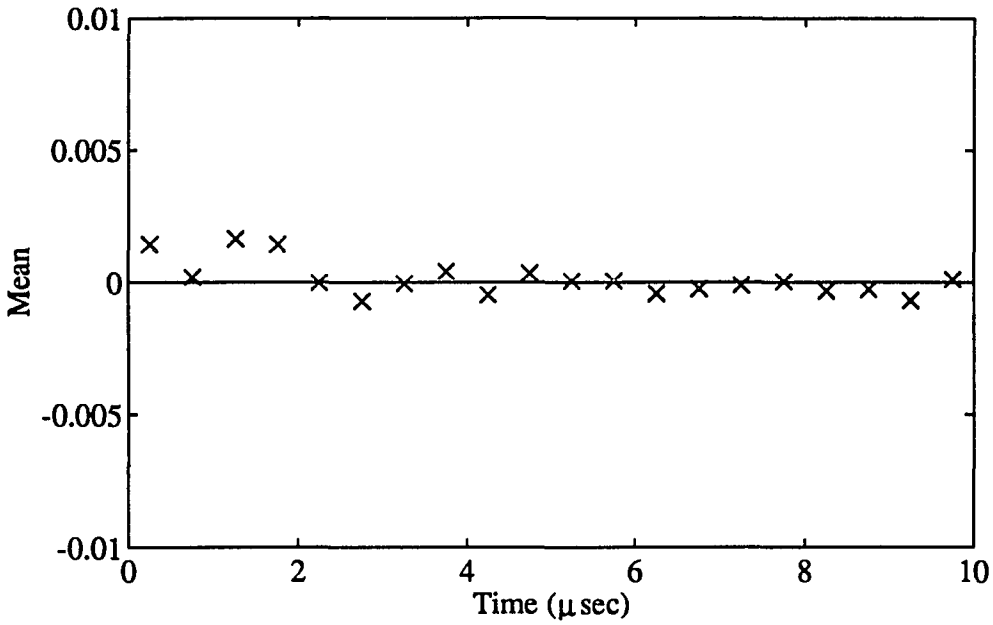


(a)

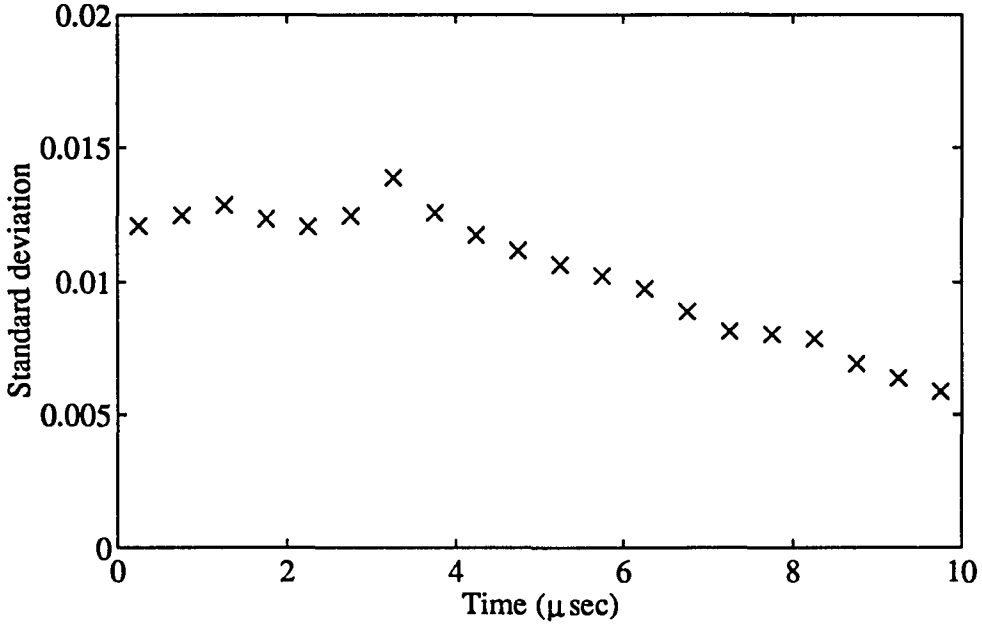


(b)

Figure 3.3: Mean and standard deviation of data set 1: (a) mean, (b) standard deviation

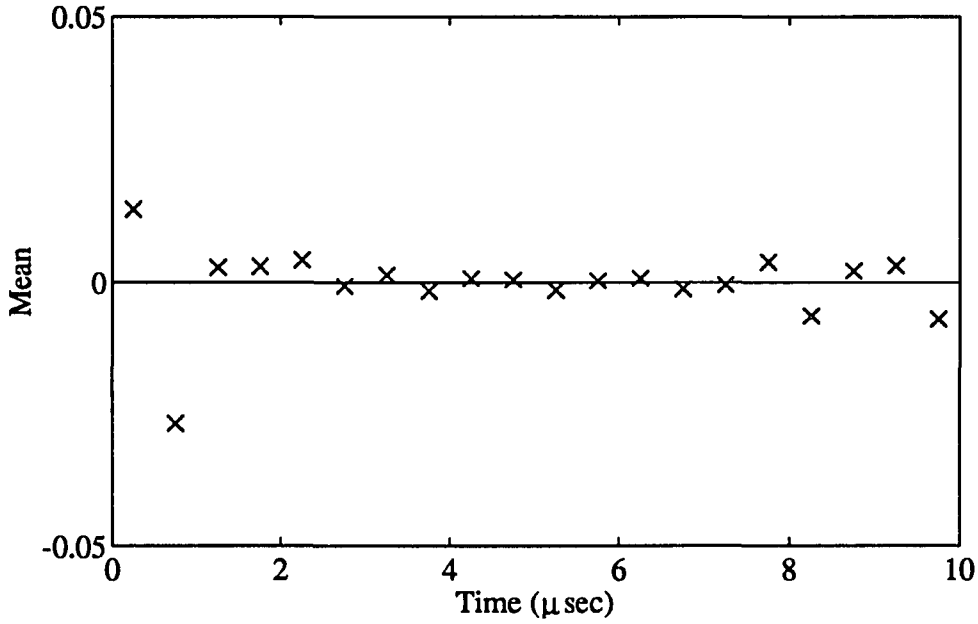


(a)

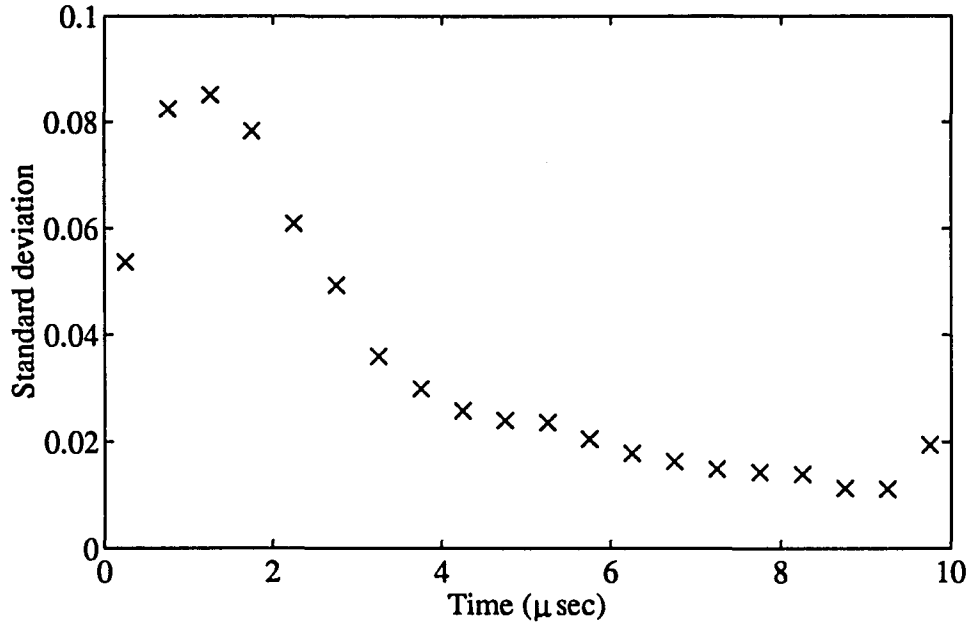


(b)

Figure 3.4: Mean and standard deviation of data set 2: (a) mean, (b) standard deviation

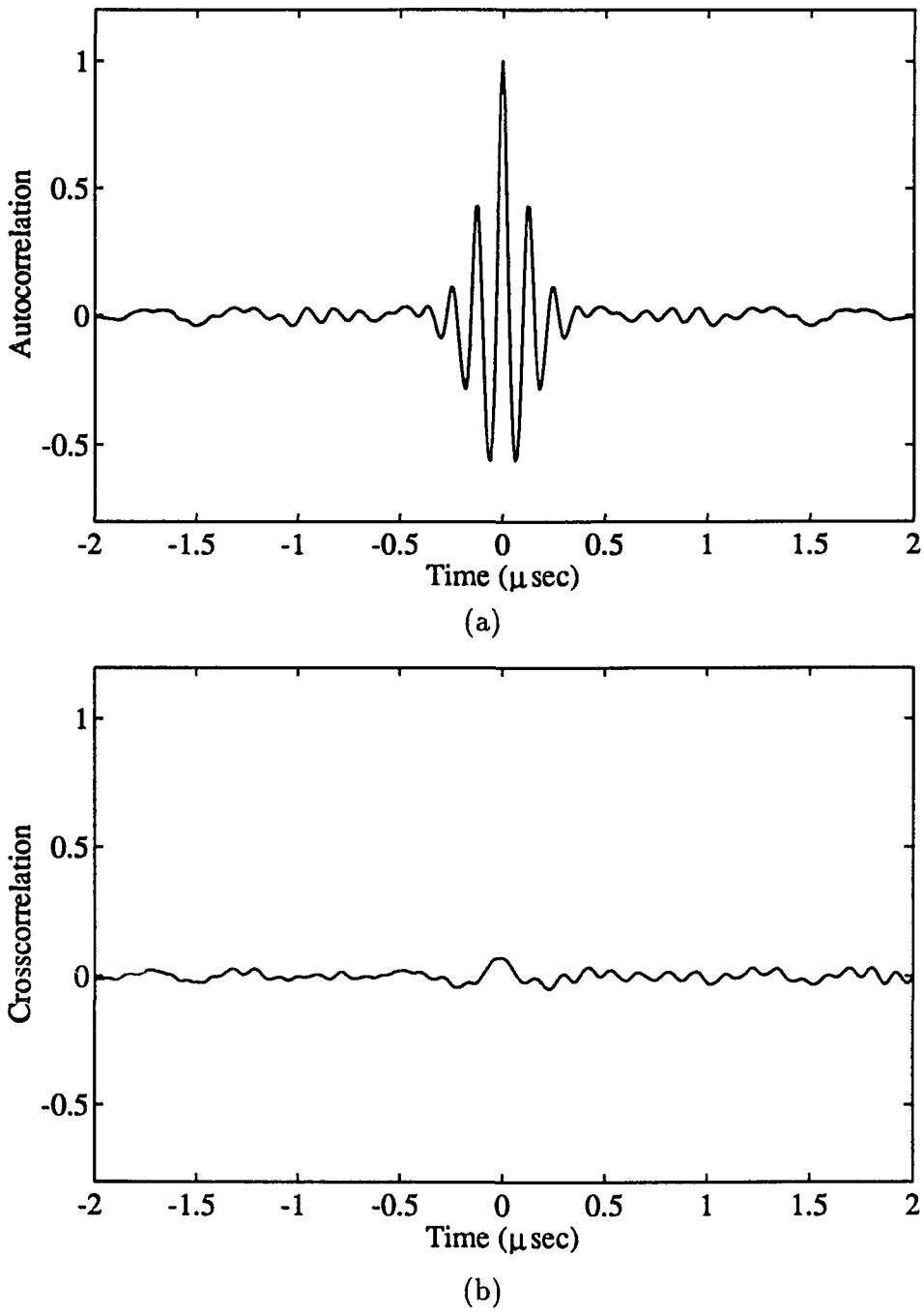


Figure 3.5: Correlation functions of data set 1: (a) autocorrelation function, (b) crosscorrelation function

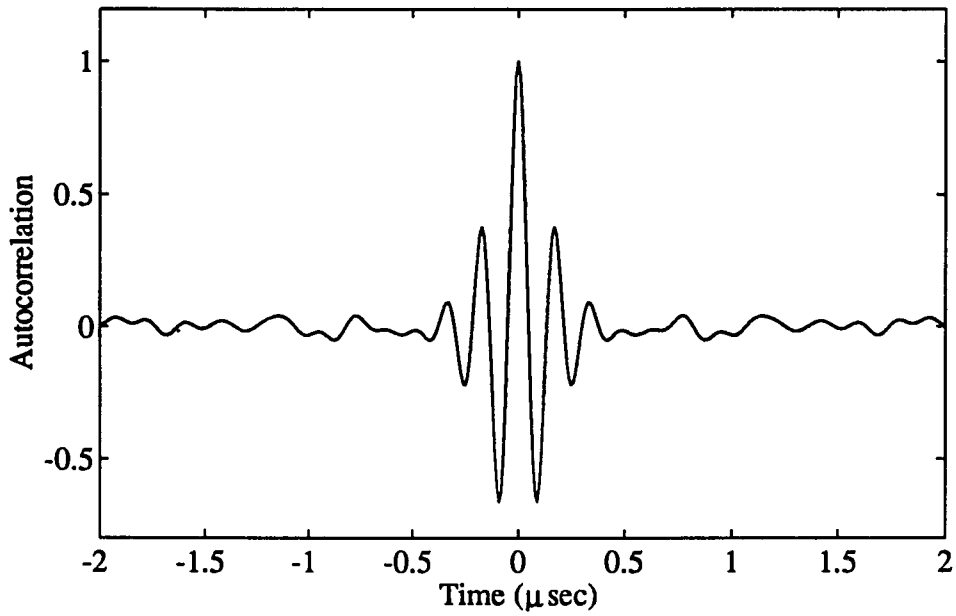


(a)

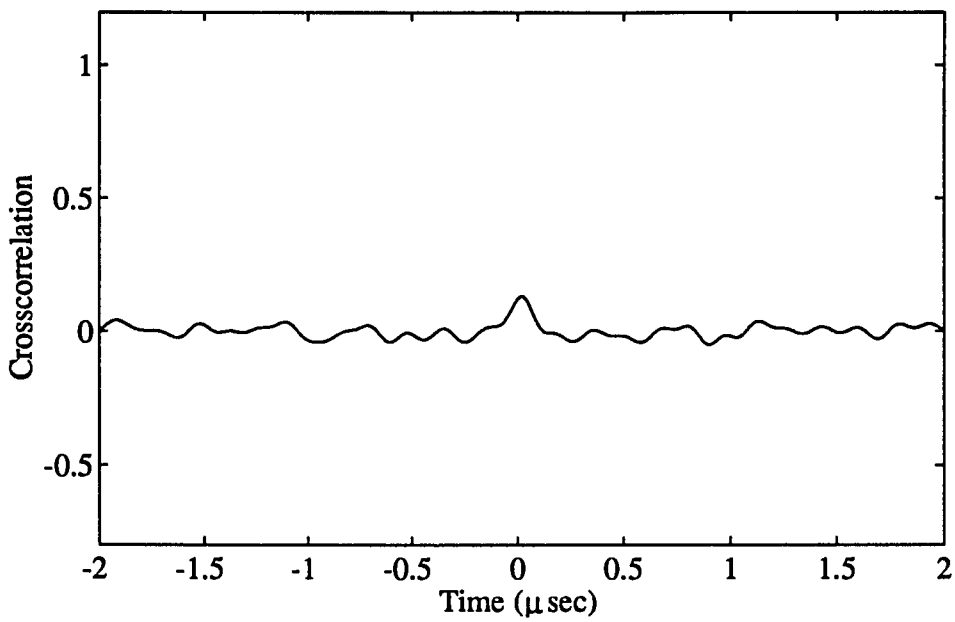


(b)

Figure 3.6: Correlation functions of data set 2: (a) autocorrelation function, (b) crosscorrelation function

As a final statistical analysis of ultrasonic noise, we consider the distribution associated with an ultrasonic noise signal. Since we have an ensemble of noise signals, two distributions associated with noise signals can be considered. That is, the distribution associated with the amplitude variations at a particular time over $N$ measurement positions and the distribution associated with a single noise signal (i.e., same measurement position but different time instants) can be compared to a Gaussian distribution. One method of comparing the distribution of a noise signal with a Gaussian distribution is via a probability plot (Hahn and Shapiro, 1967; Shapiro, 1990). A probability plot is particularly useful since it provides a visual comparison tool which may indicate what type of deviations from a Gaussian distribution exist. The basic idea of a probability plot is to plot ordered observation $x_i$, versus the expected value of the ordered observation, $E\{x_i\}$, where the expected value is a function of the sample size $n$, and the assumed distribution (in this case, Gaussian distribution). The expected value of $i$-th ordered observation $x_i$ can be computed by

$$E\{x_i\} = m_x + \sqrt{2\sigma_x}\,\text{inverf}\left(1 - 2\frac{i}{n}\right), \tag{3.5}$$

where $m_x$ and $\sigma_x$ are respectively the sample mean and standard deviation of $x$ and inverf$(\cdot)$ is inverse error function with the error function defined as

$$\text{erf}(z) \equiv \frac{2}{\sqrt{\pi}} \int_0^z \exp(-\lambda^2) d\lambda. \tag{3.6}$$

If the sample size is very large and the assumed distribution is correct, the plot of $x_i$ versus $E\{x_i\}$ (i.e., the probability plot) will be a straight line. The probability plots of noise signal amplitudes for all the measurement points at particular time are shown in Figures 3.7 (a) and 3.8 (a) for data sets 1 and 2. The probability plots of a single noise signal ($v_i(t)$ for fixed $i$ and $t = 0.2 \sim 0.3$ $\mu$s) are also shown in Figures 3.7

(b) and 3.8 (b) for data sets 1 and 2. While a limited number of points is available, the data fit the line well within the central regions for both cases, indicating that each type of noise is reasonably Gaussian.

## Application to Hard-Alpha Detection

The wavelet transform based signal processing technique was implemented in software using MATLAB and tested using simulated ultrasonic data described in the preceding sections. In the first application example, the effect of SNR of ultrasonic data to the detection performance of the proposed signal processing technique was studied using data set 1 and 2. The effect of flaw shape change was studied in the second application example. In these applications, we assumed that the flaw signal waveform is partially known. The first step in applying this technique is to obtain the information about the flaw signal center frequency and bandwidth. Maximum energy frequency and bandwidth of the flaw signal are assumed to be available from the partially known signal waveform. The wavelet transform was carried out as the inner product of the shifted and compressed wavelets and the input signal.

The detection performance of the proposed signal processing technique in application to the hard-alpha detection using simulated ultrasonic data was evaluated by means of an ROC curve and compared with the performance of the matched filter. In determining ROC curve for the matched filter, the flaw signal waveform and noise autocorrelation were assumed to be known exactly. Then, the optimal matched filter can be found as $h(t)$ which satisfies

$$\sum_j h(T-j)R(i,j) = s(i), \tag{3.7}$$

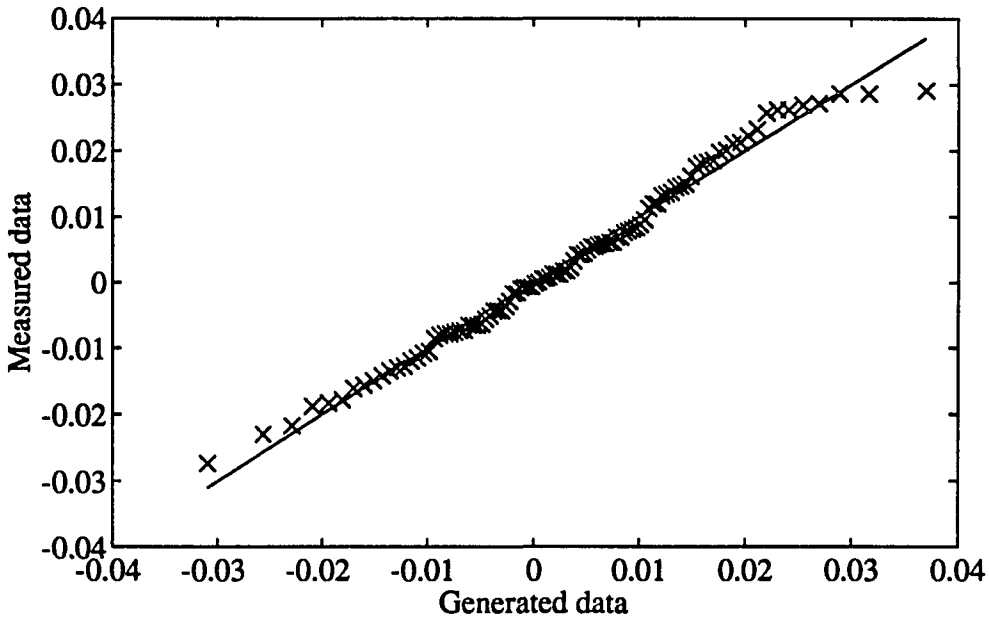


(a)

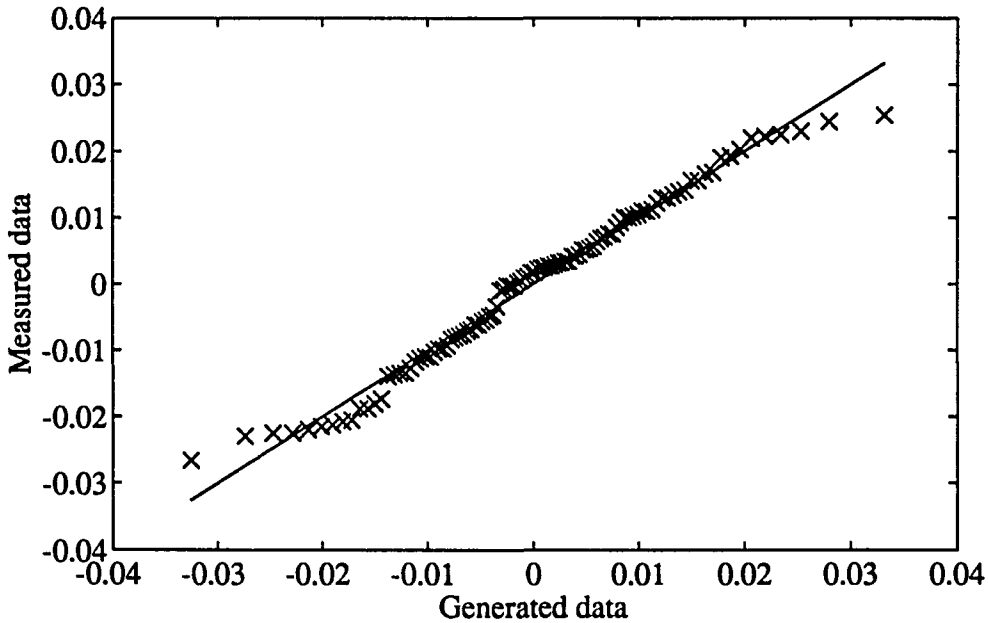


(b)

Figure 3.7: Probability plots of data set 1: (a) $v_i(t)$ for fixed $t$ and variable $i$, (b) single noise signal (fixed $i$ and variable $t$)

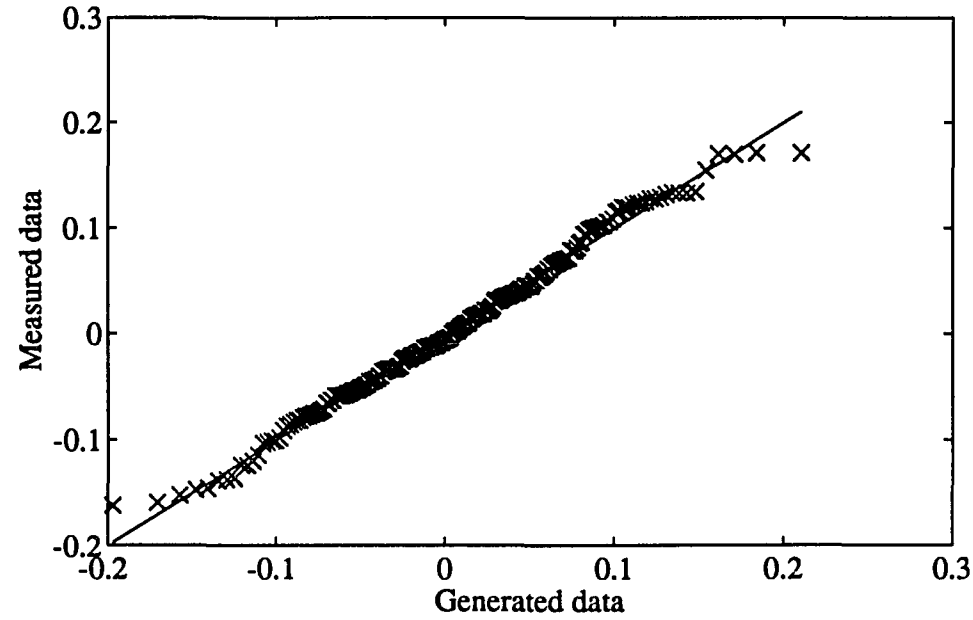


(a)

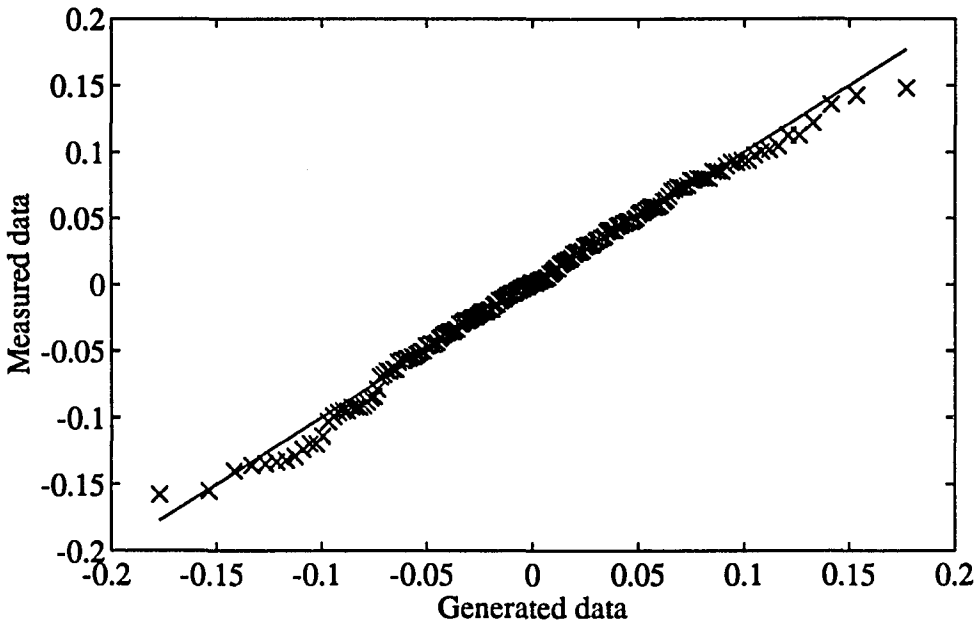


(b)

Figure 3.8: Probability plots of data set 2: (a) $v_i(t)$ for fixed $t$ and variable $i$, (b) single noise signal (fixed $i$ and variable $t$)

where $s(t)$ is flaw signal, and $R(i,j)$ is the autocorrelation function of noise. The Neyman-Pearson criterion was used to compute the POD and POF or ROC curves of the detection method. The method of computing the performance curves is to start by assigning a value for the POF. This involves estimating a value of threshold $\eta$ that satisfies

$$\text{POF} = \int_{\eta}^{\infty} f_0(y)dy. \tag{3.8}$$

This threshold value $\eta$ is then used to compute the value of POD by

$$\text{POD} = \int_{\eta}^{\infty} f_1(y)dy. \tag{3.9}$$

**Example 1**

In this example, we study the performance of the wavelet transform based signal processing method using data set 1 and 2. The flaw signals for each data set were obtained theoretically using the Thompson-Gray measurement model. To study how SNR affects the detection performance, three different flaw sizes were used to generate different SNR flaw signals for data set 1. The flaw sizes and their corresponding SNR's were 0.8, 1, 1.2 mm and $-5.82$, $-3.78$, $-2.21$ dB respectively. Each signal in the data sets was obtained by adding the corresponding simulated flaw signal to the experimentally obtained grain noise signal from a Ti-6426 alloy sample.

The wavelet transform was carried out using parameters obtained from the partially known flaw signal waveform. The Gaussian wavelet function shown in Figure 2.5 was used as the basis function. The scale parameter $m$ was fixed as 3 for both data sets. The center frequencies were chosen as 4, 6.35 and 8.7 MHz for data set 1 and 4, 5.7 and 7.4 MHz for data set 2 respectively. Figures 3.9 and 3.10 show the wavelet transformed signals of data set 1 and set 2 for scale parameter $m = 3$ and

three different center frequencies. From the magnitude peaks shown in Figures 3.9 (b) and 3.10 (b), two types of features are extracted: (1) relative peak location and (2) magnitude ratio with respect to one of the filtered signals regarded as reference. The reference filter is determined from the maximum energy frequency of the flaw signals. In this application, bandpass filters with center frequencies of 6.35 MHz and 5.7 MHz are references for data sets 1 and 2.

Figure 3.11 compares the ROC curves of the wavelet transform based method and the matched filter. The detection performance of the proposed signal processing method is very close to that of the matched filter for data set 1 for various SNR's. For data set 2, the detection performance achieved is worse than that of the matched filter. This is perhaps due to the fact that the proposed signal processing method which is based on frequency diversity does not perform very well when the bandwidth of the flaw signal is small as in the case of data set 2.

**Example 2**

The wavelet transform based signal processing technique is tested in this example to detect inclusions that are not of spherical shape. Because Thompson-Gray measurement model can not handle not spherical shape inclusions, perturbed inclusion shapes are simulated through signal modeling equations which have modeling error. Second, fourth, and sixth order ARMA equations were used to generate perturbed flaw signals from data set 1 flaw signal of flaw size 1 mm. If we define signal SNR as the ratio of signal power to modeling error power, the SNR's of perturbed flaw signals using second, fourth, and sixth ARMA equations are 4.53, 14.02, and 17.89 dB respectively. The generated flaw signals using ARMA equation are shown

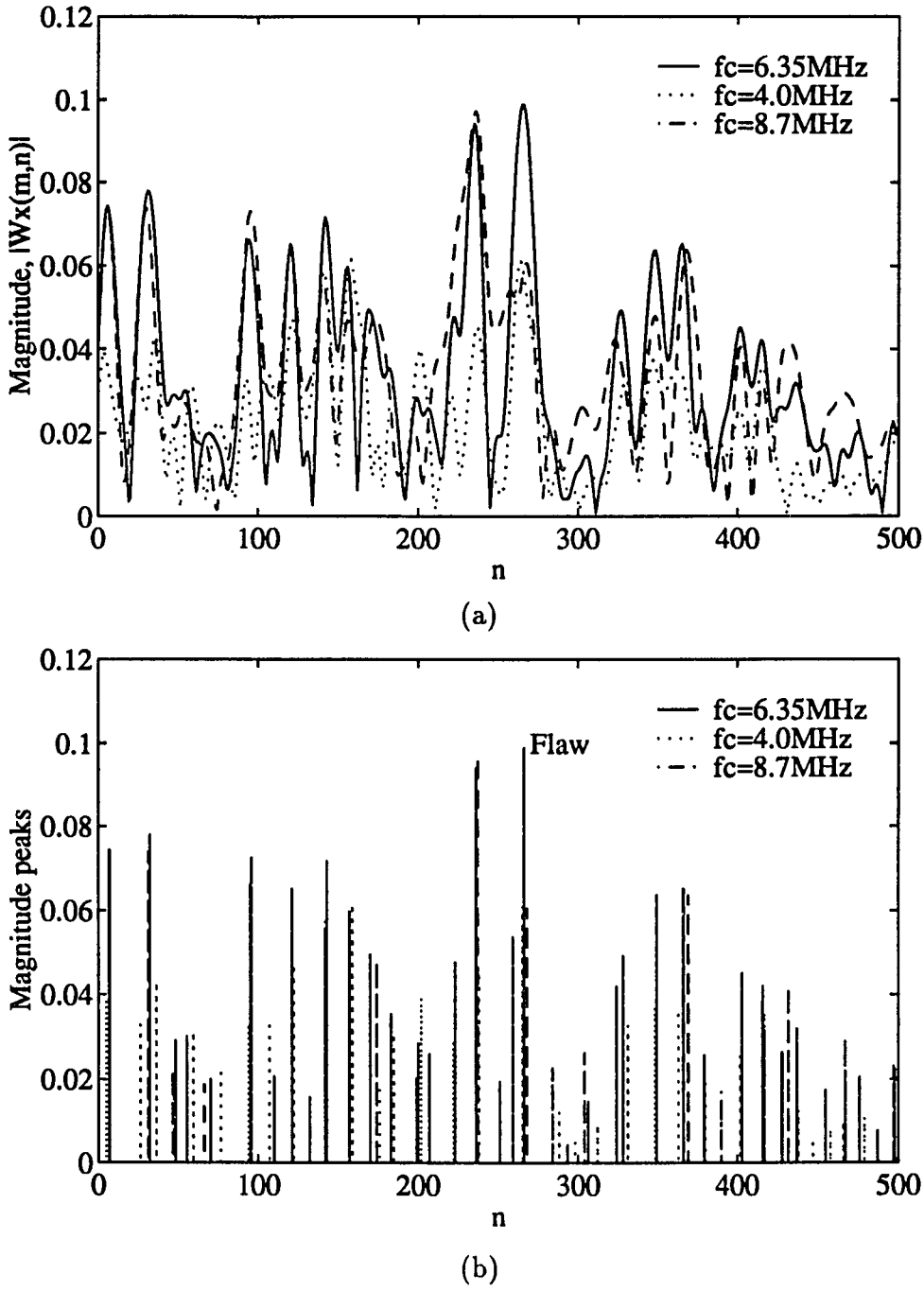


Figure 3.9: Wavelet transformed signals of data set 1: (a) magnitude, (b) magnitude peaks

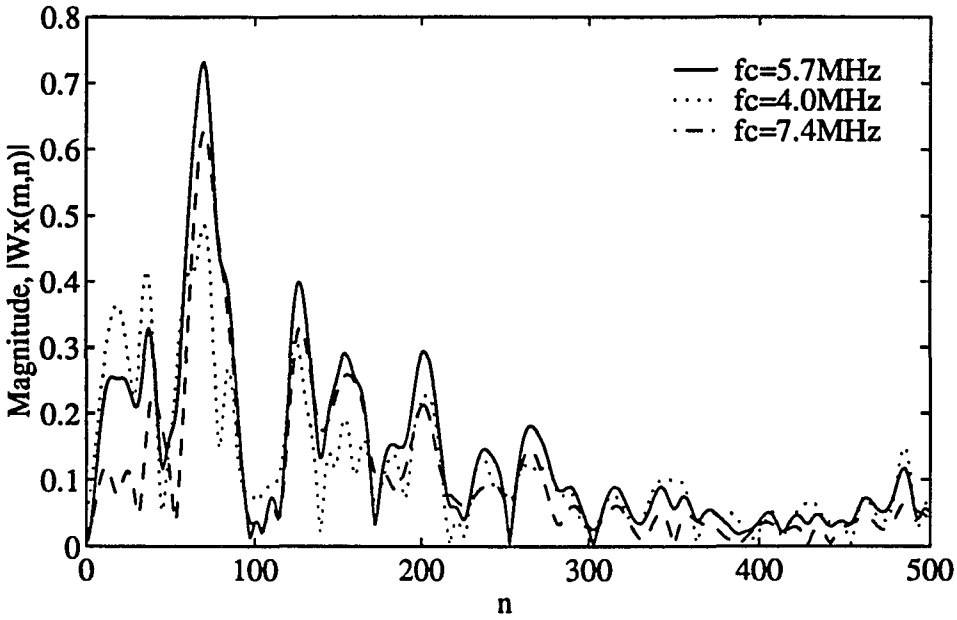


(a)

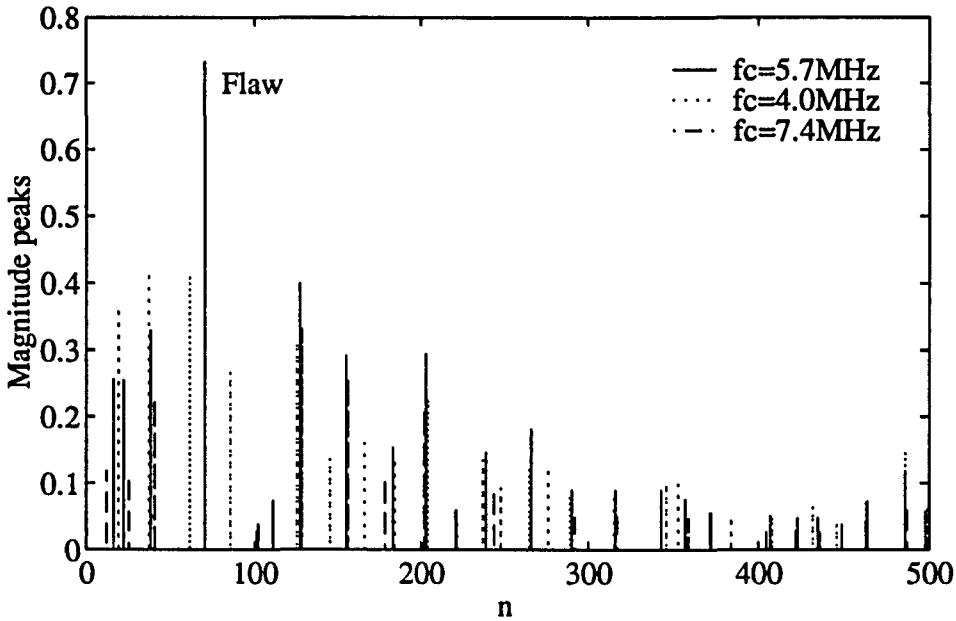


(b)

Figure 3.10: Wavelet transformed signals of data set 2: (a) magnitude, (b) magnitude peaks

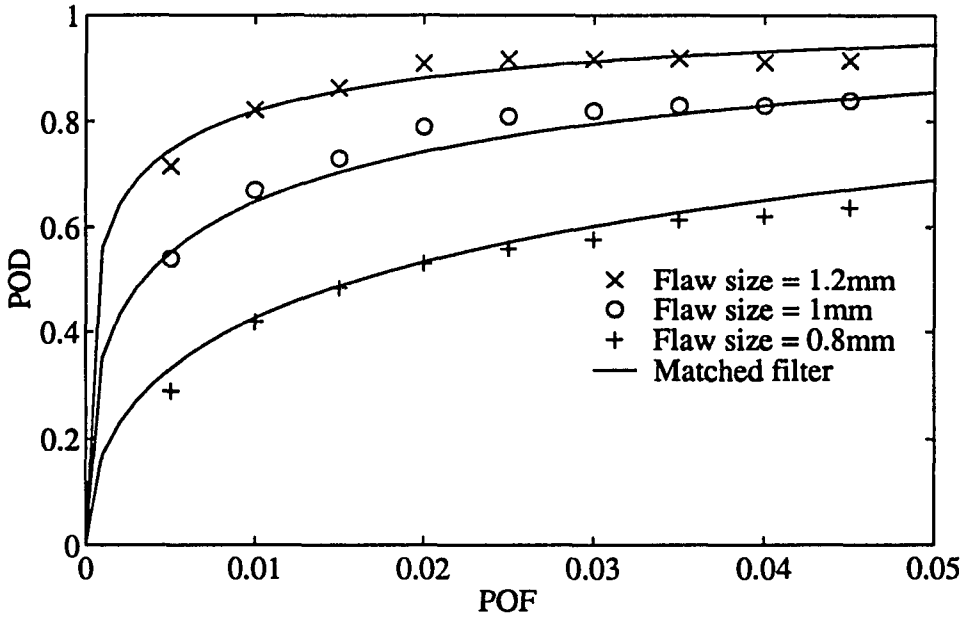


(a)

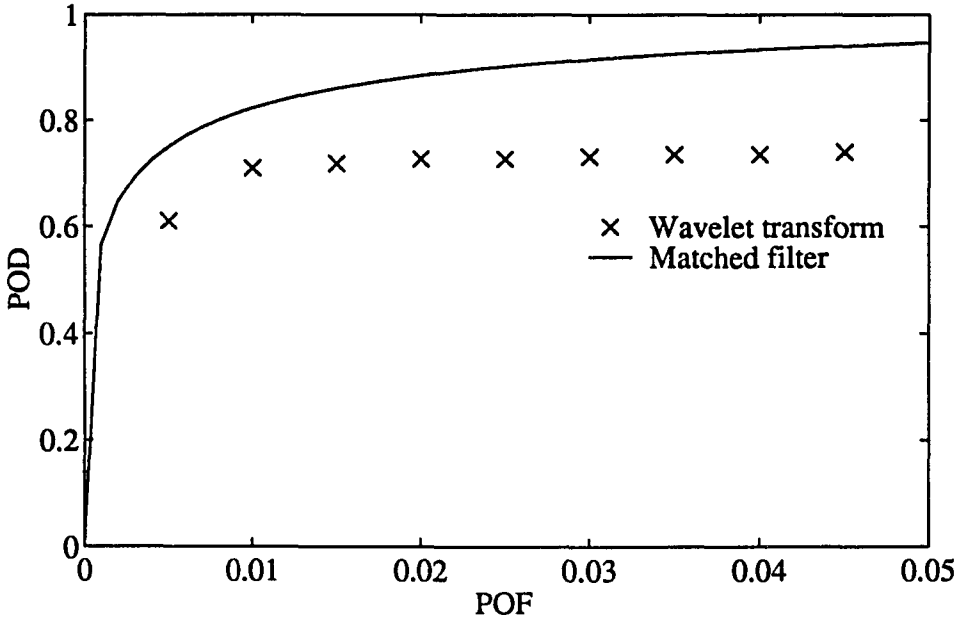


(b)

Figure 3.11: Comparison of ROC curves of wavelet transform based method and matched filter: (a) data set 1, (b) data set 2

in Figure 3.12.

The perturbed flaw signals were processed using wavelet transform parameters obtained from spherical shape flaw signal waveform. The scale parameter $m$ was fixed as 3. The center frequencies were chosen as 4, 6.35 and 8.7 MHz, and center frequency of reference bandpass filter was 6.35MHz. Figure 3.13 shows the ROC curves of perturbed flaw signals. The results show that the wavelet transform based signal processing method is not very sensitive to the slightly perturbed flaw signals. The proposed signal processing method can be successfully applied to detect hard-alpha inclusions without exact knowledge of flaw signal waveform.

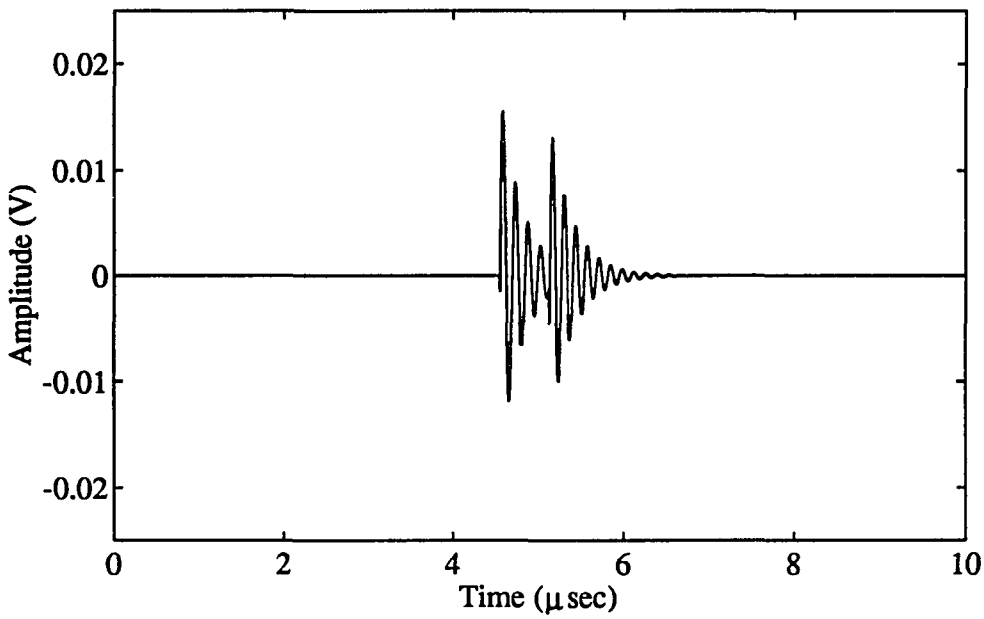


(a)

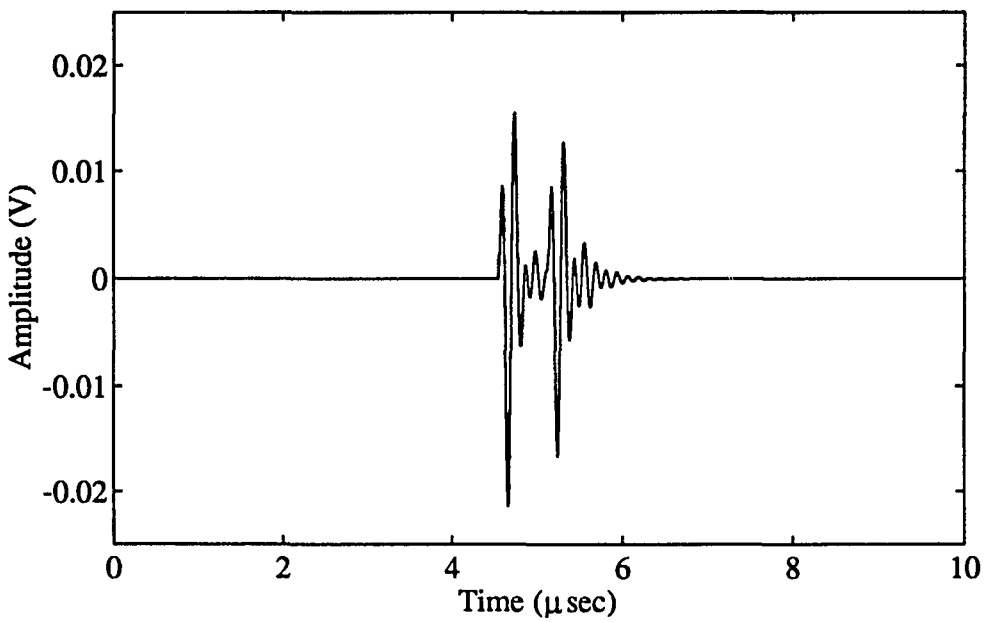


(b)

Figure 3.12: Perturbed flaw signals: (a) SNR = 4.53 dB, (b) SNR = 14.02 dB, (c) SNR = 17.89 dB

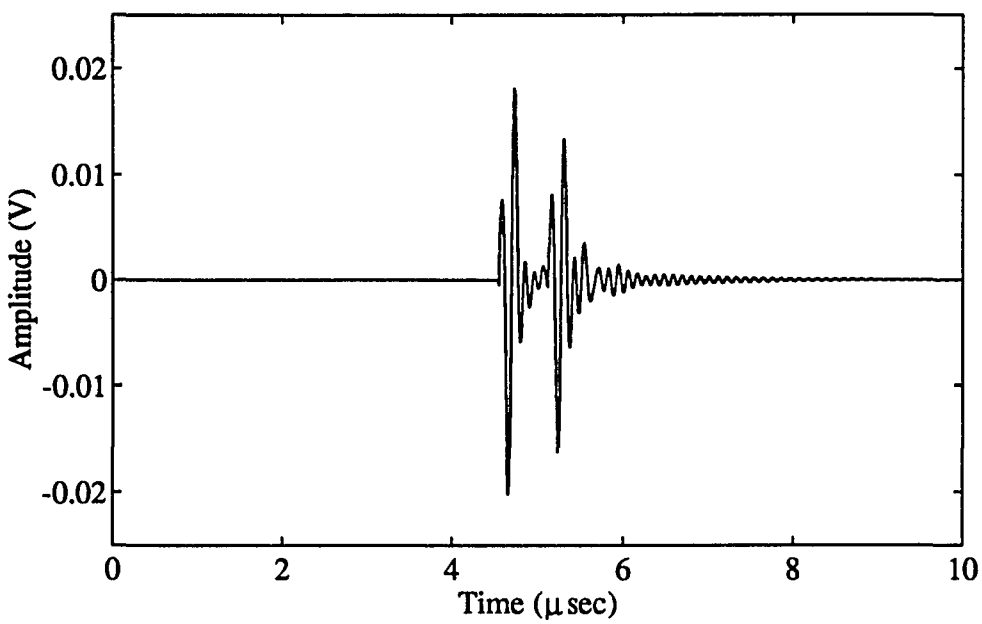


(c)

Figure 3.12 (Continued)

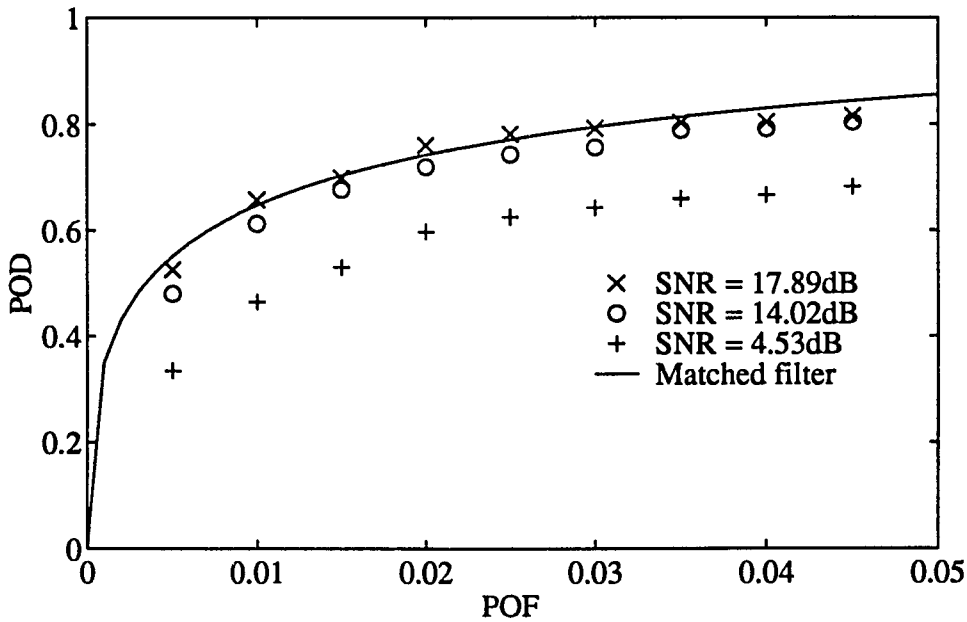


Figure 3.13: ROC curves of perturbed flaw signals

# CHAPTER 4. KALMAN FILTER BASED DECONVOLUTION

In nondestructive testing of materials and components, ultrasonic backscattered signals are often encountered. The information carried by these signals forms the basis of several techniques used for flaw detection, flaw characterization, and material characterization. In some cases, the effect of the measurement system has to be removed from these signals in order to enhance their usefulness. A deconvolution algorithm that is commonly employed for this purpose is based on the Wiener filter. In this chapter, we investigate the use of an alternative deconvolution algorithm based on the Kalman filter. The signal and system modeling of ultrasonic measurement system is presented first, followed by the elements of estimation theory for deriving a Kalman filter based deconvolution algorithm. This chapter concludes with several experimental results of ultrasonic signal deconvolution using Kalman filter based deconvolution algorithm.

## Ultrasonic Signal and System Model

In the deconvolution of an ultrasonic backscattered signal, the signal is modeled as the result of convolving the incident acoustic pulse with a signal that characterizes the material (or flaw) and furthermore corrupting it with some additive noise.

Mathematically, this can be expressed as

$$\begin{aligned} z(k) &= y(k) + v(k) \\ &= p(k) * u(k) + v(k) \\ &= \sum_{j=0}^{k} p(j)u(k-j) + v(k), \end{aligned} \tag{4.1}$$

where $k$ is the time index, $z(k)$ is the observed backscattered signal, $p(k)$ is the reference pulse which represents the measurement system response, $u(k)$ is the *reflection coefficient sequence* that characterizes the material (or flaw). In Equation (4.1), $y(k)$ represents the noise-free backscattered signal and $v(k)$ is the additive noise component which is typically sensor noise. The deconvolution problem is to estimate the reflection coefficient sequence $u(k)$ with a knowledge of $z(k)$ and $p(k)$ and an estimate of $v(k)$.

This approach is based on the linear system model shown in Figure 4.1 (a). An intuitive approach is to let the reference pulse $p(k)$ be the input to the system and reflection coefficient sequence $u(k)$ be the system impulse response. However, it is more convenient to model the *known* reference pulse $p(k)$ as the impulse response of a finite-dimensional system and let $u(k)$ be the input to the system as shown in Figure 4.1 (b). Based on this practical approach, the backscattered signal can be expressed by means of the following state-space equations:

$$\mathbf{x}(k+1) = \mathbf{F}\mathbf{x}(k) + \mathbf{G}u(k) \tag{4.2}$$

$$\begin{aligned} z(k) &= y(k) + v(k) \\ &= \mathbf{H}\mathbf{x}(k) + v(k), \end{aligned} \tag{4.3}$$

where $\mathbf{x}(k)$ is the $N \times 1$ system state vector, $\mathbf{F}$ is the $N \times N$ state transition matrix,

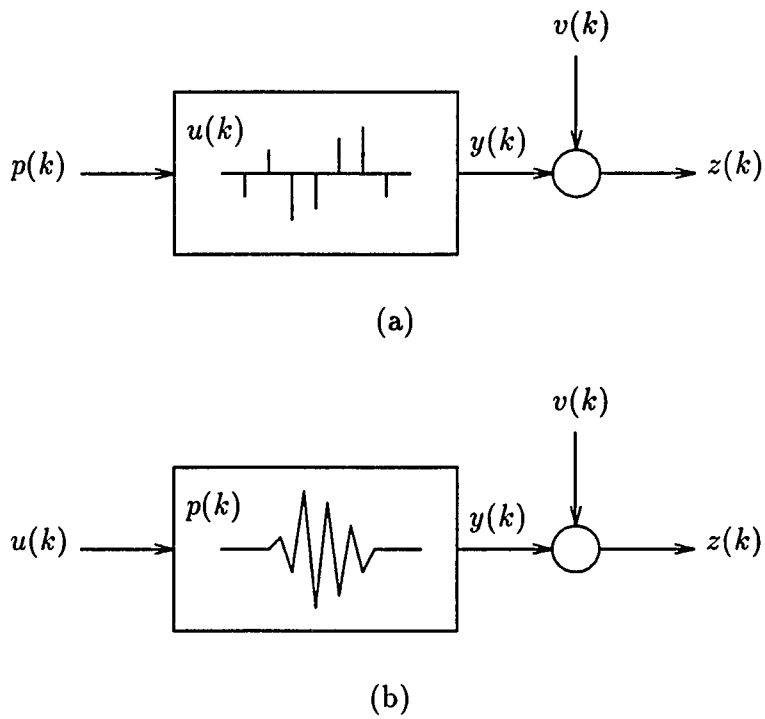


Figure 4.1: Signal models: (a) intuitive model, (b) equivalent model

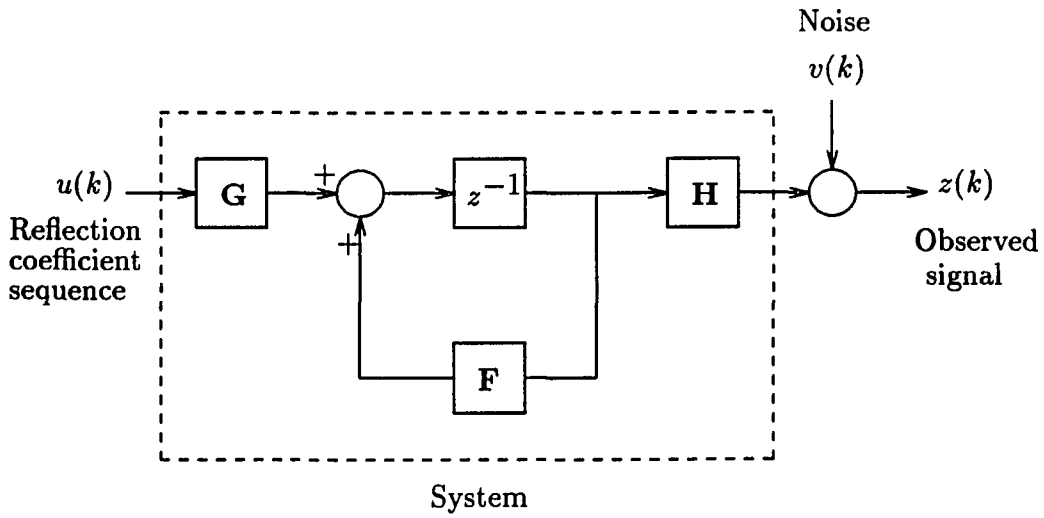


Figure 4.2: Block diagram of state-space model

**G** is the $N \times 1$ input matrix, and **H** is the $1 \times N$ measurement matrix. In Equations (4.2) and (4.3), the matrices **F**, **G**, and **H** together describe the system and must be chosen such that the system impulse response $s(k)$ approximates the reference pulse $p(k)$ using the $N$-th order ARMA (Auto Regressive Moving Average) system model. The system matrices in Equations (4.2) and (4.3) can be easily modified such that they can be time indexed. Thus, the state-space formulations (4.2) and (4.3) naturally allow for time (or space) varying systems (in this case, the reference pulse) and/or nonstationary statistics. The system equations (4.2) and (4.3) are illustrated in block diagram form in Figure 4.2.

In the state-space formulation of an ultrasonic backscattered signal, the input $u(k)$ and the measurement noise $v(k)$ are assumed to be zero-mean, white noise sequences with respective variances of $Q$ and $R$ and to be mutually uncorrelated.

Mathematically, these assumptions are expressed as

$$E\{u(k)u(j)\} = Q\delta(k-j) \tag{4.4}$$

$$E\{v(k)v(j)\} = R\delta(k-j) \tag{4.5}$$

$$E\{u(k)v(j)\} = 0, \tag{4.6}$$

where $E\{\cdot\}$ is the expectation operator and $\delta(\cdot)$ is the Kronecker delta function which is equal to one if $k$ and $j$ are equal, and to zero in the other cases.

In modeling the system, we employ the $N$-th order ARMA (Auto Regressive Moving Average) difference equation

$$\begin{aligned} y(k) + \alpha_1 y(k-1) + \alpha_2 y(k-2) + \cdots + \alpha_N y(k-N) \\ = \beta_1 u(k-1) + \beta_2 u(k-2) + \cdots + \beta_N u(k-N). \end{aligned} \tag{4.7}$$

The $2N$ system coefficients, $(\alpha_i, \beta_i, i = 1, 2, \cdots, N)$, are chosen to minimize the average mean squared error between $p(k)$ and the system impulse response $s(k)$ over an appropriate time window. Given a system equation, several state-space realizations are possible, i.e., there are several choices for the system matrices $\mathbf{F}$, $\mathbf{G}$, and $\mathbf{H}$. Using the controllable canonical form realization (Chen, 1984), the state-space equations realizing the system equation in (4.7) can be written as

$$\mathbf{F} = \begin{bmatrix} 0 & 1 & \cdots & 0 & 0 \\ 0 & 0 & \cdots & 0 & 0 \\ \vdots & \vdots & & \vdots & \vdots \\ 0 & 0 & \cdots & 0 & 1 \\ -\alpha_N & -\alpha_{N-1} & \cdots & -\alpha_2 & -\alpha_1 \end{bmatrix} \tag{4.8}$$

$$\mathbf{G} = \begin{bmatrix} 0 & 0 & \cdots & 0 & 1 \end{bmatrix}^T \tag{4.9}$$

$$\mathbf{H} = \begin{bmatrix} \beta_N & \beta_{N-1} & \cdots & \beta_2 & \beta_1 \end{bmatrix}. \tag{4.10}$$

## Minimum-Variance Estimation

In this section, we present elements of estimation theory that are essential for the development of a Kalman filter based deconvolution algorithm. The first step in the deconvolution problem is to obtain an estimate of the system vector $\mathbf{x}(k)$ from the noise corrupted measurements $z(k)$. Once we have such an estimate, we can obtain the estimate of $u(k)$ that is linearly related to $\hat{\mathbf{x}}(k)$ by means of linear transformations.

Throughout this chapter, the notation $\hat{\mathbf{x}}(k|j)$ denotes the estimate of $\mathbf{x}$ at time $k$ based on the measurements up to and including $j$-th, and $\tilde{\mathbf{x}}(k|j)$ denotes the estimation error,

$$\tilde{\mathbf{x}}(k|j) = \mathbf{x}(k) - \hat{\mathbf{x}}(k|j). \tag{4.11}$$

In terms of notation $\hat{\mathbf{x}}(k|j)$, three cases can be distinguished. When estimation time $k$ is greater than measurement time $j$, i.e., $k > j$, $\hat{\mathbf{x}}(k|j)$ is an optimal predicted estimate of $\mathbf{x}(k)$; when $k = j$, $\hat{\mathbf{x}}(k|j)$ is an optimal filtered estimate of $\mathbf{x}(k)$; and when $k < j$, $\hat{\mathbf{x}}(k|j)$ is an optimal smoothed estimate of $\mathbf{x}(k)$.

In estimation theory, we choose $\hat{\mathbf{x}}(k|j)$ in such a manner that some measure of $\hat{\mathbf{x}}(k|j)$ is minimized. Many different measures of error can be used, but the most common measure is the mean-squared error (Meditch, 1969; Van Trees, 1968). The information available to us is measurements $z(k)$. Given these measurements, we have to find an estimate of $\mathbf{x}(k|j)$ as a function of $z(k)$ such that the mean-squared error $E\{\tilde{\mathbf{x}}^T(k|j)\tilde{\mathbf{x}}(k|j)\}$ is minimized. This is equivalent to minimizing the conditional

mean-squared error,

$$J[\tilde{\mathbf{x}}(k|j)] = E\Big\{\tilde{\mathbf{x}}^T(k|j)\tilde{\mathbf{x}}(k|j)|\mathbf{z}(j)\Big\}, \tag{4.12}$$

where $\mathbf{z}(j) = [\ z(1)\ \ z(2)\ \ \cdots\ \ z(j)\ ]^T$. The solution to this problem is given in Equation (4.13), which is known as the fundamental theorem of estimation theory (Mendel, 1983)

$$\hat{\mathbf{x}}(k|j) = E\{\mathbf{x}(k)|\mathbf{z}(j)\}. \tag{4.13}$$

When $\mathbf{x}(k)$ and $\mathbf{z}(j)$ are jointly Gaussian, the estimator that minimizes the mean-squared error (4.12) becomes

$$\hat{\mathbf{x}}(k|j) = E\{\mathbf{x}(k)\} + \mathbf{P_{xz}}(k,j)\mathbf{P_{zz}^{-1}}(j,j)\Big[\mathbf{z}(j) - E\{\mathbf{z}(j)\}\Big], \tag{4.14}$$

where covariance matrices $\mathbf{P_{xz}}$ and $\mathbf{P_{zz}}$ are defined as

$$\mathbf{P_{xz}}(k,j) = E\Big\{\Big[\mathbf{x}(k) - E\{\mathbf{x}(k)\}\Big]\Big[\mathbf{z}(j) - E\{\mathbf{z}(j)\}\Big]^T\Big\} \tag{4.15}$$

$$\mathbf{P_{zz}}(j,j) = E\Big\{\Big[\mathbf{z}(j) - E\{\mathbf{z}(j)\}\Big]\Big[\mathbf{z}(j) - E\{\mathbf{z}(j)\}\Big]^T\Big\}. \tag{4.16}$$

Estimator (4.13) is true for all values of $k$ and $j$; hence, in principle, it can be used to provide optimal predicted, filtered, or smoothed estimates of $\mathbf{x}(k)$. This mean-squared error estimator has important properties. It is unbiased and has minimum error variance. Thus, this estimator is a minimum-variance estimator. (It is also referred to as an efficient estimator.)

Because our deconvolution problem is closely related to the filtered and smoothed estimates of $\mathbf{x}(k)$, we describe only filtered and smoothed estimates of $\mathbf{x}(k)$ in the next two sections.

## Optimal filtering

The object of optimal filtering is to find the minimum-variance estimates of $\mathbf{x}(k)$ based on the past and present measurements. A recursive minimum-variance optimal filtering algorithm was developed by Kalman and is known as the Kalman filter (Kalman, 1960; Kalman and Bucy, 1961). A very popular form of the Kalman filter algorithm to estimate the optimal filtered estimate $\hat{\mathbf{x}}(k|k)$ is the following so-called predictor-corrector formula (Meditch, 1969; Sorenson, 1980).

Predictor

$$\hat{\mathbf{x}}(k|k-1) = \mathbf{F}\hat{\mathbf{x}}(k-1|k-1) \tag{4.17}$$

$$\mathbf{P}(k|k-1) = \mathbf{F}\mathbf{P}(k-1|k-1)\mathbf{F}^T + Q\mathbf{G}\mathbf{G}^T \tag{4.18}$$

Innovations

$$\tilde{z}(k|k-1) = z(k) - \mathbf{H}\hat{\mathbf{x}}(k|k-1) \tag{4.19}$$

$$\eta(k) = \mathbf{H}\mathbf{P}(k|k-1)\mathbf{H}^T + R \tag{4.20}$$

Corrector

$$\mathbf{K}(k) = \mathbf{P}(k|k-1)\mathbf{H}^T\eta^{-1}(k) \tag{4.21}$$

$$\hat{\mathbf{x}}(k|k) = \hat{\mathbf{x}}(k|k-1) + \mathbf{K}(k)\tilde{z}(k|k-1) \tag{4.22}$$

$$\mathbf{P}(k|k) = \left[\mathbf{I} - \mathbf{K}(k)\mathbf{H}\right]\mathbf{P}(k|k-1) \tag{4.23}$$

In these equations, $\hat{\mathbf{x}}(k|k)$ and $\hat{\mathbf{x}}(k|k-1)$ denote respectively the estimates of the state vector $\mathbf{x}(k)$ based on the measurements $z(0)$ through $z(k)$ and $z(0)$ through $z(k-1)$. The corresponding estimation error covariance matrices are denoted respectively as $\mathbf{P}(k|k)$ and $\mathbf{P}(k|k-1)$. In addition, $\tilde{z}(k|k-1)$ denotes the innovations process (also known as the measurement residual process or prediction error process), $\eta(k)$ denotes

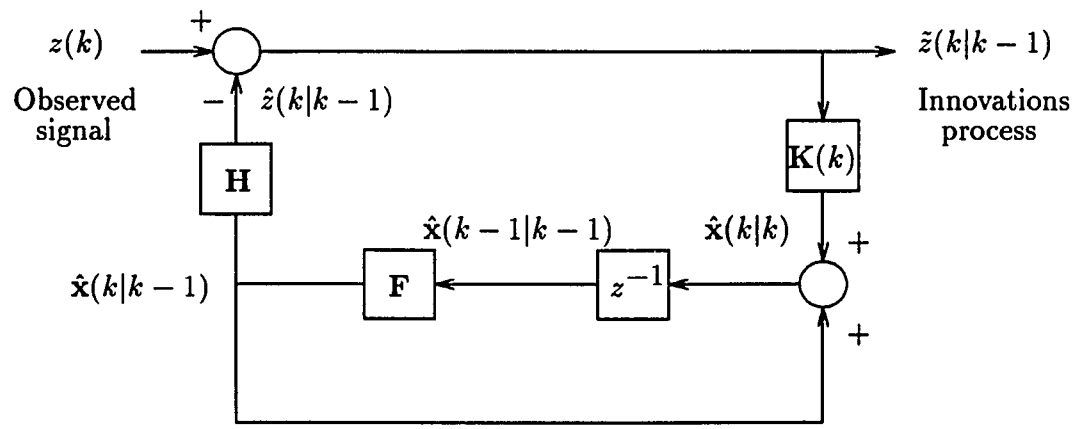


Figure 4.3: Block diagram of Kalman filter

its variance, and $\mathbf{K}(k)$ is called the Kalman gain vector.

The Kalman filter recursion is started by assuming suitable values for $\hat{\mathbf{x}}(0|0)$ and $\mathbf{P}(0|0)$. The innovations process $\tilde{z}(k|k-1)$, the output of Kalman filter, will be used in the optimal smoothed estimation of $\mathbf{x}(k)$. The block diagram of a Kalman filter which produces the innovations process is shown in Figure 4.3.

### Optimal smoothing

The smoothing problem deals with estimates of $\mathbf{x}(k)$, $\hat{\mathbf{x}}(k|j)$ for $k < j$. We can distinguish three types of smoothing; fixed-interval, fixed-point, and fixed-lag. The fixed-interval smoothing estimate is $\hat{\mathbf{x}}(k|L)$, where $L$ is fixed measurement interval. The fixed-interval estimate of state vector $\mathbf{x}(k)$ is based on all the available measurement data ($z(i)$, $i = 1, 2, \cdots, L$). The fixed-point smoothed estimate is $\hat{\mathbf{x}}(k|k+l)$, where $k$ is fixed and $l$ is varied. A fixed-lag estimate is $\hat{\mathbf{x}}(k|k+l)$, where $l$ is fixed and $k$ is varied. Fixed-point and fixed-lag estimates usually do not make use of all data. On the other hand, fixed-interval smoothing estimate uses all measurement

data. Therefore, we cannot expect better estimation by other forms of smoothing than by fixed-interval smoothing.

The recursive fixed-interval smoothing estimate and its error covariance matrix equations are given as follows:

$$\hat{\mathbf{x}}(k|L) = \hat{\mathbf{x}}(k|k-1) + \mathbf{P_X}(k|k-1)\mathbf{r}(k|L) \tag{4.24}$$

$$\mathbf{P_X}(k|L) = \mathbf{P_X}(k|k-1) - \mathbf{P_X}(k|k-1)\mathbf{S}(k|L)\mathbf{P_X}(k|k-1), \tag{4.25}$$

where $k = L-1, L-2, \cdots, 1$. The $N \times 1$ vector $\mathbf{r}(k|L)$, called the residual state vector, and its $N \times N$ covariance matrix $\mathbf{S}(k|L)$ are defined as

$$\mathbf{r}(k|L) = \mathbf{P_X^{-1}}(k|k-1)\left[\hat{\mathbf{x}}(k|L) - \hat{\mathbf{x}}(k|k-1)\right] \tag{4.26}$$

$$\mathbf{S}(k|L) = E\{\mathbf{r}(k|L)\mathbf{r}^T(k|L)\}. \tag{4.27}$$

The residual state vector and its covariance matrix $\mathbf{S}(k|L)$ can be computed using the following backward recursive equations.

$$\mathbf{r}(k|L) = \left[\mathbf{I} - \mathbf{K}(k)\mathbf{H}\right]^T \mathbf{F}^T \mathbf{r}(k+1|L) + \mathbf{H}^T \eta^{-1}(k)\tilde{z}(k|k-1) \tag{4.28}$$

$$\mathbf{S}(k|L) = \left[\mathbf{I} - \mathbf{K}(k)\mathbf{H}\right]^T \mathbf{F}^T \mathbf{S}(k+1|L)\mathbf{F}\left[\mathbf{I} - \mathbf{K}(k)\mathbf{H}\right] + \mathbf{H}^T \eta^{-1}(k)\mathbf{H}, \tag{4.29}$$

where $k = L, L-1, \cdots, 1$, $\mathbf{r}(L+1|L) = \mathbf{0}$, and $\mathbf{S}(L+1|L) = \mathbf{0}$. In the above equations, the innovations process $\tilde{z}(k|k-1)$, its variance $\eta^{-1}(k)$, and Kalman filter gain vector $\mathbf{K}(k)$ are available from Kalman filter calculations described in the previous section.

## Deconvolution Algorithm

In the previous section, we pointed out that the goal of the deconvolution problem was to obtain the optimal estimates of reflection coefficient sequence $u(k)$ from

the noisy measurements $z(k)$. We also obtained the optimal filtered and optimal smoothed estimates of state vector $\mathbf{x}(k)$. From the optimal smoothed estimate of $\mathbf{x}(k)$, we can derive the optimal smoothed estimate of $u(k)$. The optimal estimates of $\mathbf{x}(k)$ and $u(k)$ are seen to have the following relationship from Equation (4.2),

$$\mathbf{G}\hat{u}(k|L) = \hat{\mathbf{x}}(k+1|L) - \mathbf{F}\hat{\mathbf{x}}(k|L). \tag{4.30}$$

From this equation, we can derive following fixed-interval smoother for $\hat{u}(k)$:

$$\hat{u}(k|L) = Q\mathbf{G}^T\mathbf{r}(k|L) \tag{4.31}$$

$$\mathbf{P}_u(k|L) = Q - Q\mathbf{G}^T\mathbf{S}(k|L)\mathbf{G}Q \tag{4.32}$$

In these equations, $\hat{u}(k|L)$ is the optimal (minimum-variance) fixed-interval smoothed estimate of $u(k)$ and $\mathbf{P}_u(k|L)$ is its smoothing error variance. The quantity $\mathbf{r}(k|L)$ and its covariance matrix $\mathbf{S}(k|L)$ can be computed from Equations (4.28) and (4.29).

Mendel has derived a two-pass fixed-interval algorithm from Equations (4.28), (4.29), (4.31), and (4.32) (Mendel, 1977a). During the first pass of the algorithm, data are processed in a forward manner by means of Kalman filter Equations (4.17)–(4.23); the quantities $\mathbf{K}(k)$ and $\eta^{-1}(k)$ are stored for use in the second pass, and the innovations process $\tilde{z}(k|k-1)$ is computed. During the second pass, a residual state vector $\mathbf{r}(k|L)$ and its covariance matrix $\mathbf{S}(k|L)$ are generated in a backward manner from Equations (4.28) and (4.29), and finally the fixed-interval estimate $\hat{u}(k|L)$ and its error variance $\mathbf{P}_u(k|L)$ are computed from Equations (4.31) and (4.32). The flow diagram of Kalman filter based deconvolution algorithm is shown in Figure 4.4.

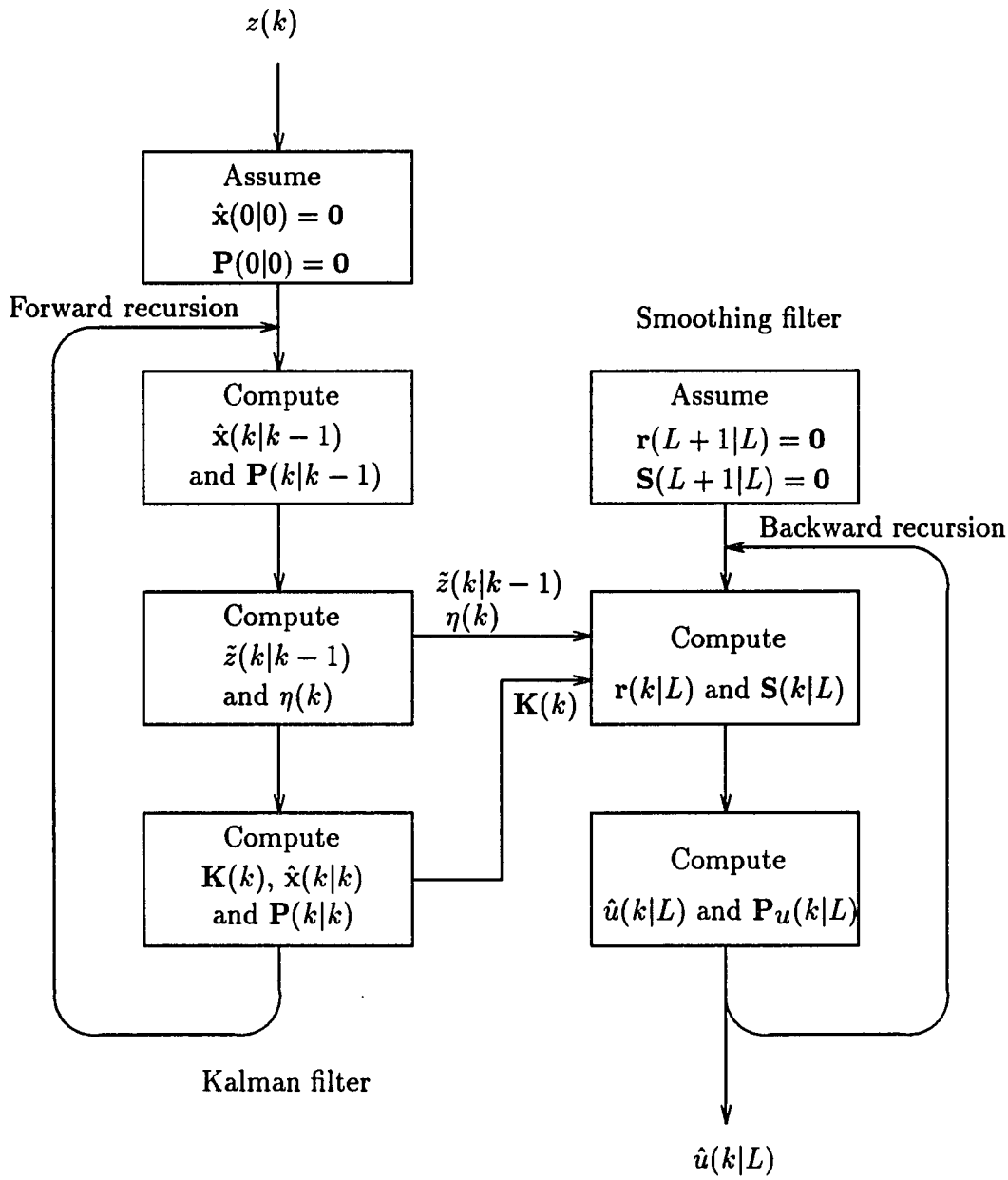


Figure 4.4: Flow diagram of Kalman filter based deconvolution algorithm

Table 4.1: System modeling performances of different order system models

| Model order | Signal-to-noise ratio (dB) |
|---|---|
| 2nd | 5.239 |
| 4th | 13.741 |
| 6th | 20.933 |
| 8th | 38.010 |
| 10th | 40.375 |

### Application Examples

The deconvolution algorithm described in the previous section was implemented in software and tested extensively using simulated and actual ultrasonic data. In these examples, the system model was designed by matching its impulse response $s(k)$ with a given reference pulse $p(k)$ in the least squares sense. A nonlinear least square function in the MATLAB Optimization Toolbox (Grace, 1992) which implements the Levenberg-Marquardt algorithm was used for this purpose. It was found that the system order has a significant influence on the modeling accuracy. For instance, consider the reference pulse $p(k)$ shown in Figure 4.5. This signal was obtained experimentally by sampling signals from a 15 MHz transducer at a 100 MHz sampling rate. Second, sixth, and tenth order system models were designed to match this pulse. System modeling performances of different order system models are compared in Table 4.1. The impulse responses of these systems are shown respectively in Figures 4.6, 4.7, and 4.8. The frequency domain representation (DFT) of the different signals are also shown in the figures. It is seen that the higher the model order, the better the approximation of its impulse response is to the given pulse. As a compromise, we have selected a sixth order model in this example.

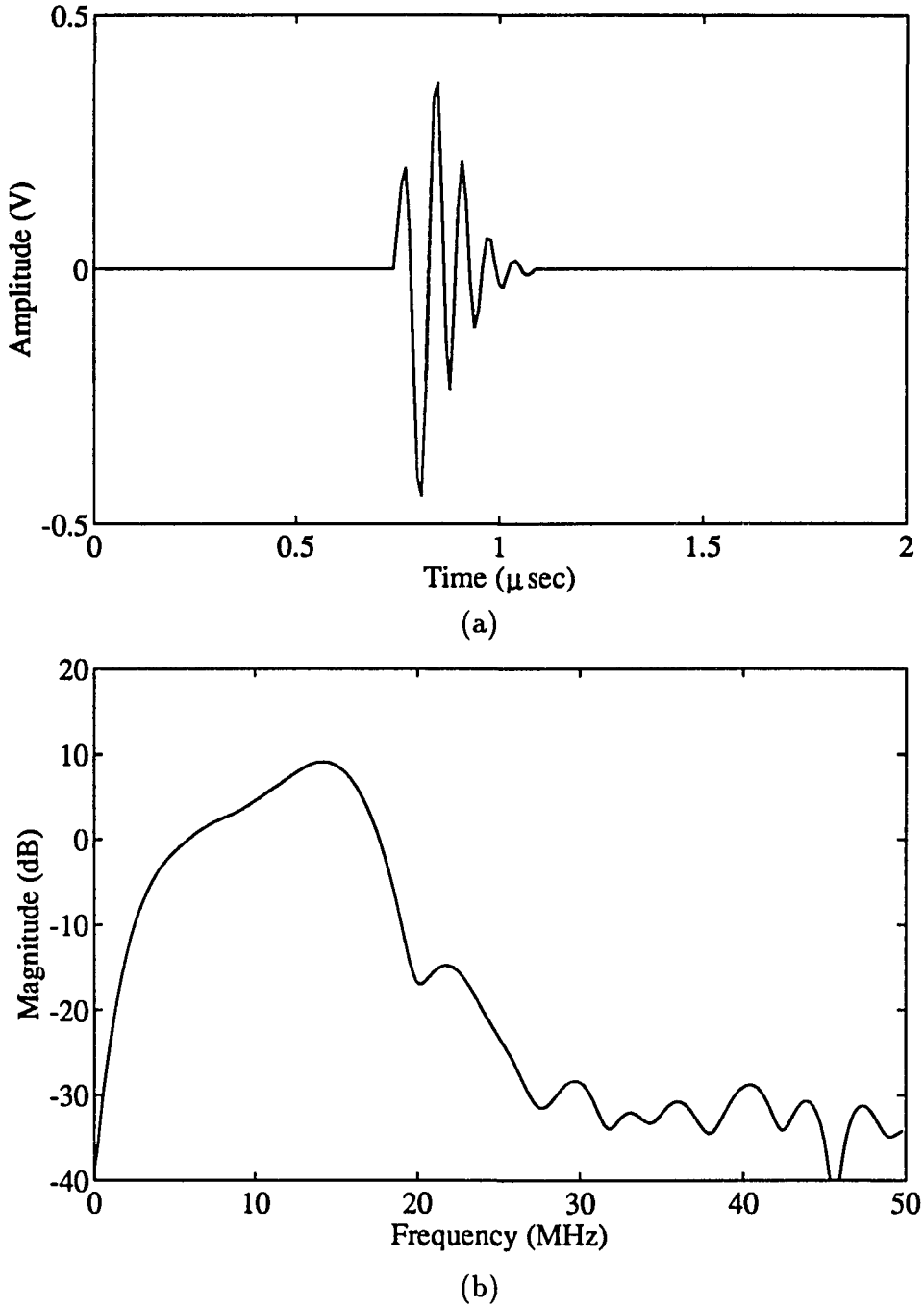


Figure 4.5: Reference pulse: (a) time-domain signal, (b) magnitude spectrum

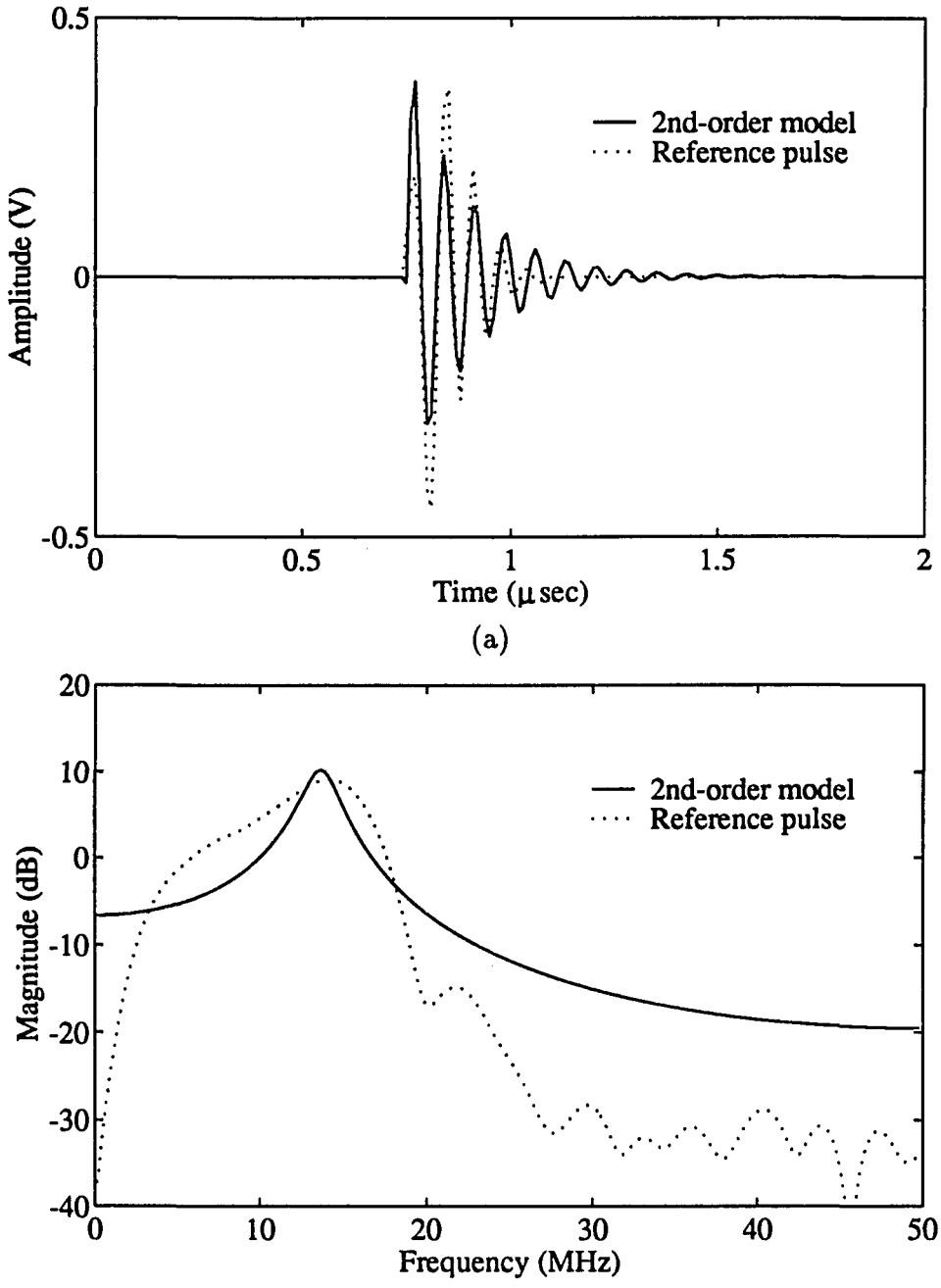


Figure 4.6: Second-order system model: (a) impulse response, (b) magnitude spectrum

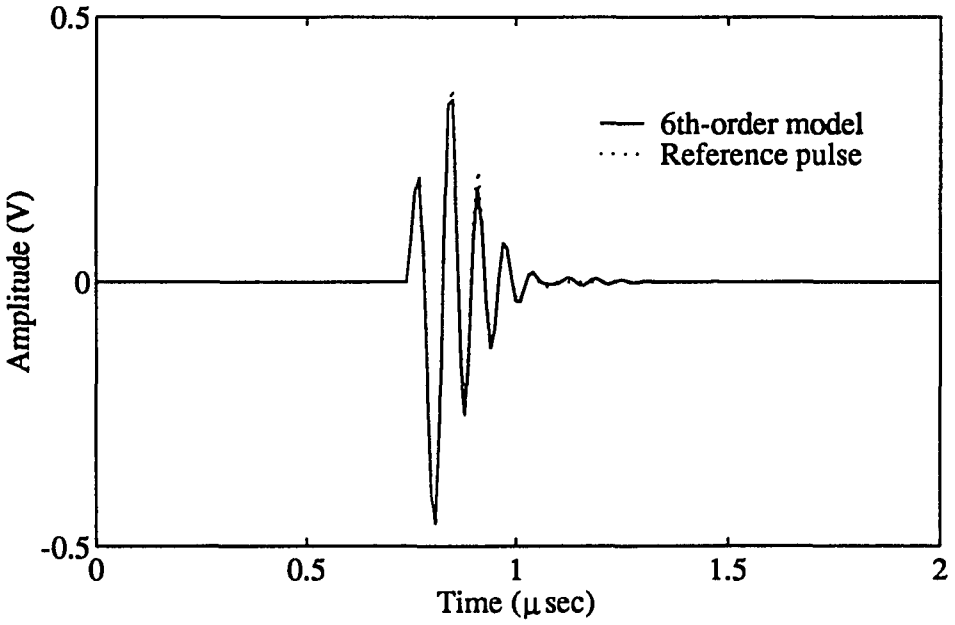


(a)

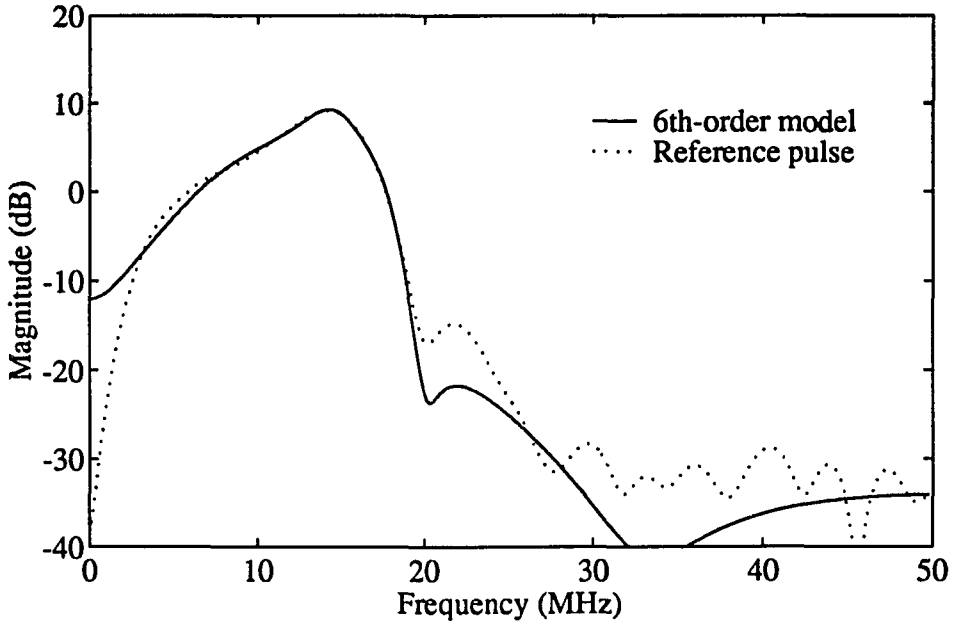


(b)

Figure 4.7: Sixth-order system model: (a) impulse response, (b) magnitude spectrum

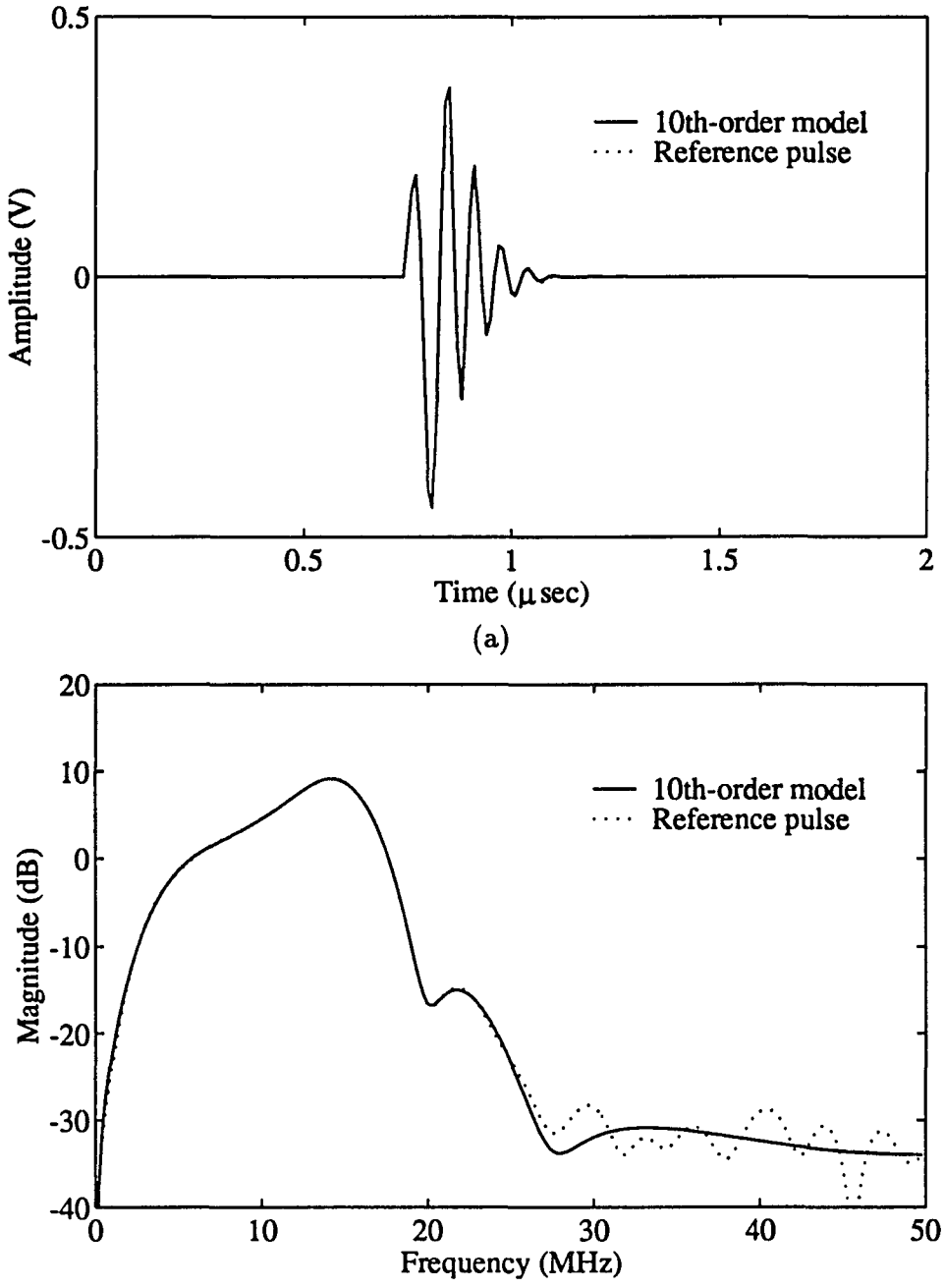


Figure 4.8: Tenth-order system model: (a) impulse response, (b) magnitude spectrum

In many situations, it turns out that only the shape of the system impulse response is of importance and not its absolute magnitude. In this case, we can normalize the impulse response such that its energy is unity, i.e.,

$$\sum |s(k)|^2 = 1. \tag{4.33}$$

Such a normalization makes the power in the (noiseless) output signal $y(k)$ equal to $Q$, the variance of the input $u(k)$. Assuming that the observed backscattered signal $z(k)$ has a high SNR in a certain section $w_{z1}$, we can obtain an estimate of $Q$ by calculating the power

$$P_{z1} = \frac{1}{N_{z1}} \sum_{w_{z1}} |z(k)|^2 \approx P_y = Q, \tag{4.34}$$

where $N_{z1}$ is the number of samples in $w_{z1}$. The choice of the window $w_{z1}$ depends on a number of factors: (1) it must enclose the signal of interest, (2) it must have enough sample points to provide a good estimate of $P_{z1}$, (3) it must not be so long that signal attenuation becomes a significant factor, etc. Estimating the variance $R$ of the observed noise is somewhat difficult. If there is a section $w_{z2}$ of $z(k)$ where the signal $y(k)$ is known to be quite small, then $R$ can be estimated by the expression

$$P_{z2} = \frac{1}{N_{z2}} \sum_{w_{z2}} |z(k)|^2 \approx P_v = R, \tag{4.35}$$

where $N_{z2}$ is the number of samples in $w_{z2}$. Otherwise, additional experiments may have to be performed or a trial-and-error technique may have to be employed to obtain an estimate of $R$. Notice that with $Q$ and $R$ estimated as above (using Equations (4.34) and (4.35)), the ratio $Q/R = P_y/P_v$ is nothing but the SNR of the observed signal $z(k)$.

### Example 1

In this example, we study the performance of the deconvolution algorithm using synthetic data. The backscattered signal $z(k)$ was first assumed to be the reference pulse $p(k)$ shown in Figure 4.5 (a). The result of the deconvolution $\hat{u}(k)$ when $Q/R$ is 10 dB is shown in Figure 4.9 (a). Ideally, the deconvolved signal must be an impulse with a flat spectrum corresponding to a single reflector in the path of the reference pulse. The actual signal $\hat{u}(k)$ differs from this ideal because of two reasons: (1) the system impulse response $s(k)$ does not quite match the reference pulse $p(k)$, and (2) the SNR of the backscattered signal is not high enough at all frequencies. To study how SNR affects the performance, the deconvolution was done for two other values of $Q/R$. The results are shown in Figure 4.9 (b) and (c). The spectra of the different deconvolved outputs and that of $z(k)$ (also $s(k)$ in this case) are shown in Figure 4.9 (d). It is observed that the effect of the deconvolution is essentially to flatten the spectrum of $z(k)$ at those frequencies for which the SNR is high compared to the assumed value of $Q/R$.

The resolving capability of the deconvolution algorithm was studied next by using a backscattered signal $z(k)$ generated by adding the reference pulse in Figure 4.5 (a) with a delayed version of itself, the delay corresponding to 12 samples ($0.12\mu$s). The reflected signal by double reflector and its deconvolved signal $\hat{u}(k)$ are shown in Figure 4.10 (a) and (b). The deconvolved signal $\hat{u}(k)$ indicates that the algorithm has done a good job of separating the two impulses.

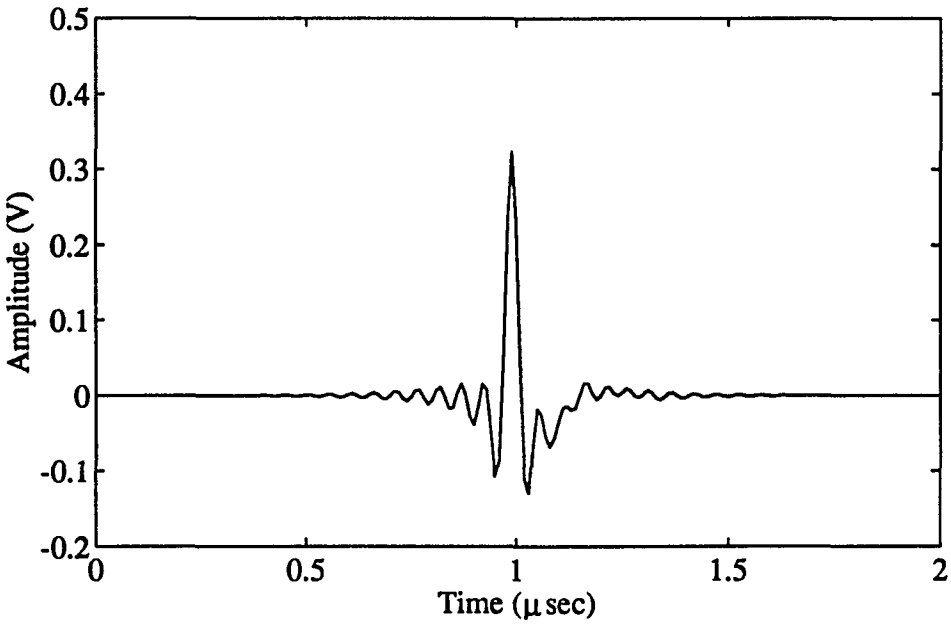


(a)

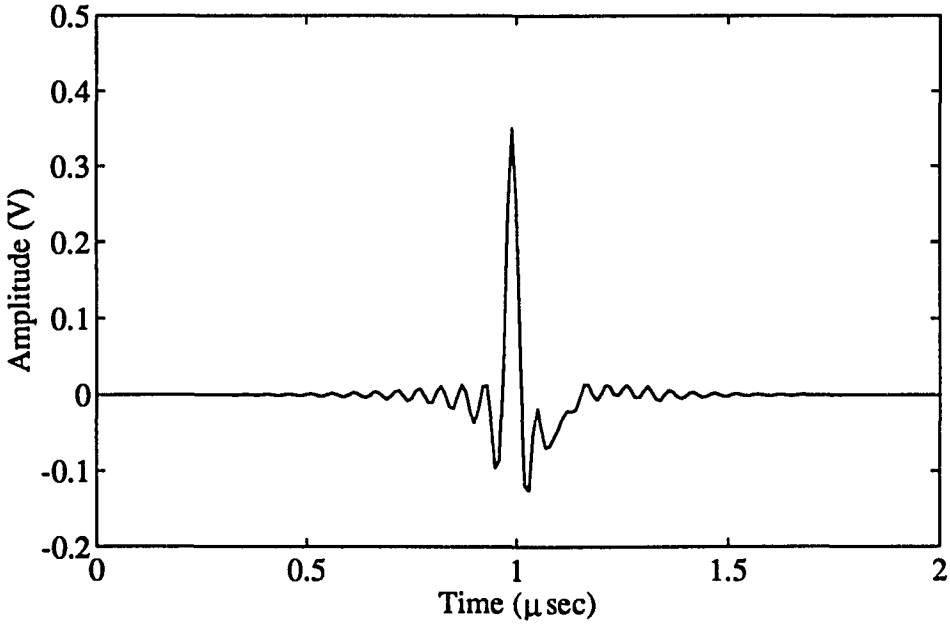


(b)

Figure 4.9: Deconvolution of single reflector: (a) $Q/R$=10dB, (b) $Q/R$=13dB, (c) $Q/R$=20dB, (d) deconvolved signal magnitude spectra

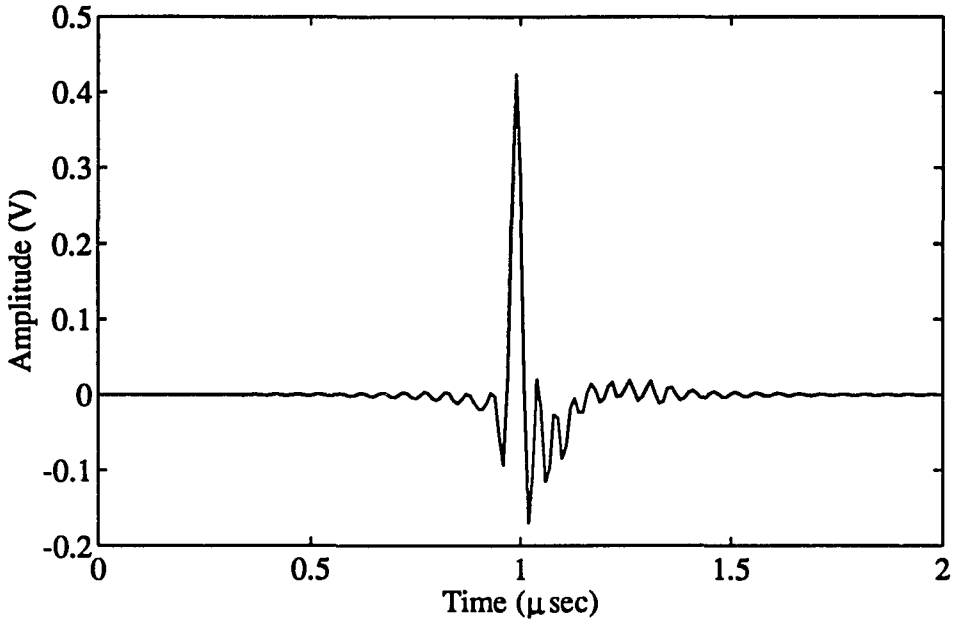


(c)

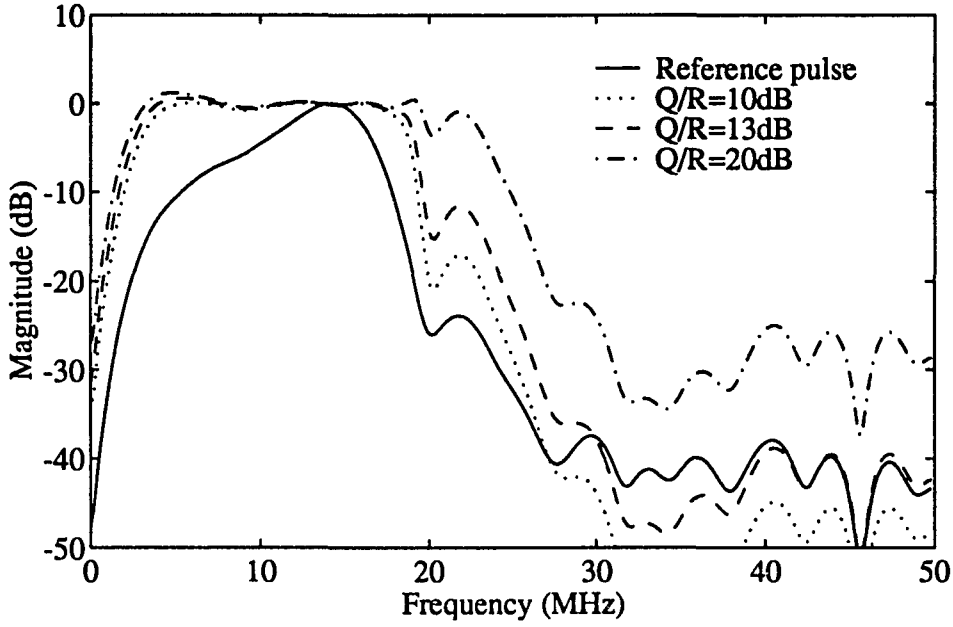


(d)

Figure 4.9 (Continued)

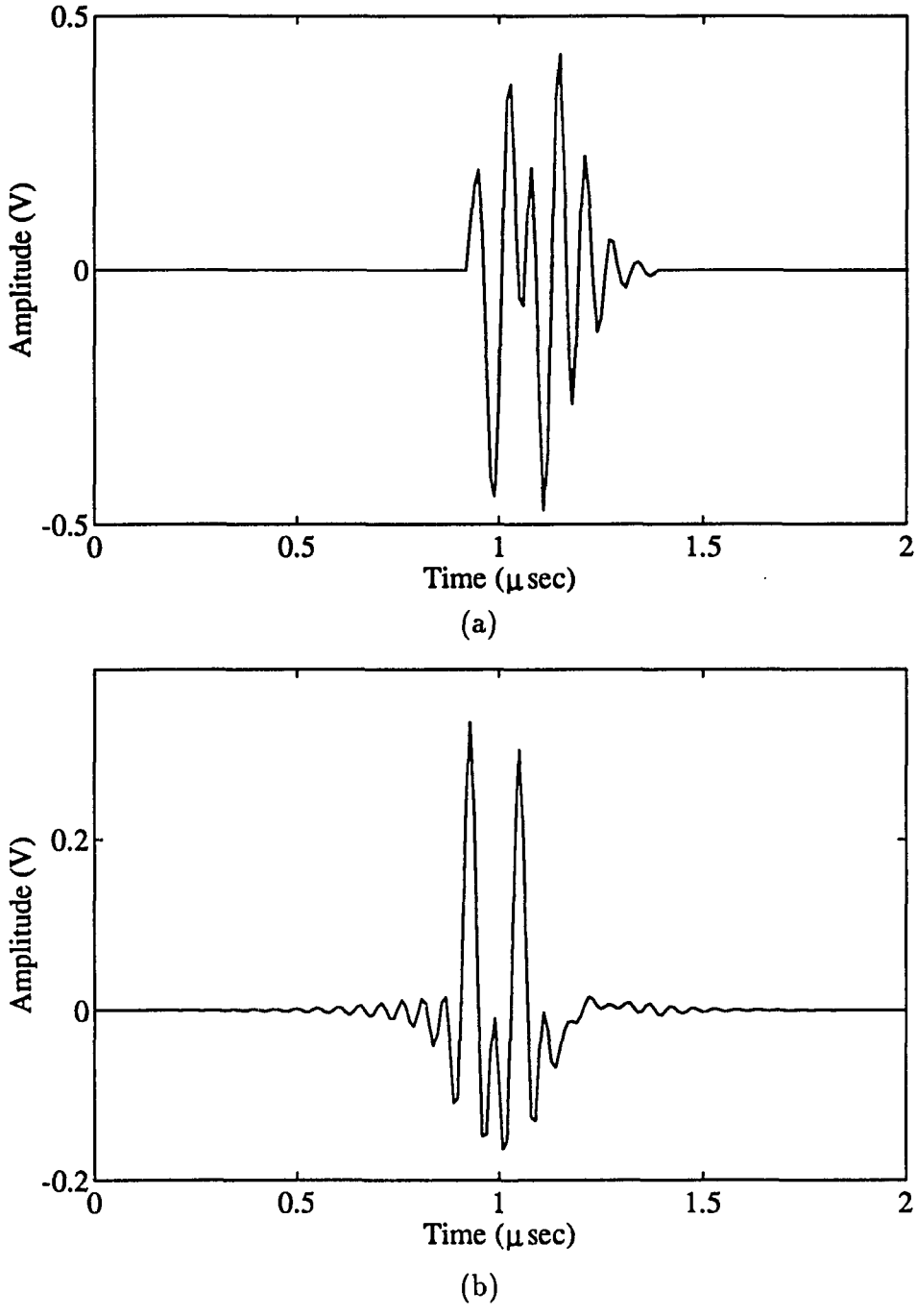


Figure 4.10: Deconvolution of double reflector: (a) reflected signal, (b) deconvolved signal ($Q/R$=10dB)

### Example 2

The deconvolution algorithm is used in this example to deconvolve the backscattered signal from a flaw to extract its impulse response. The data for the example were obtained using a diffusion bonded disk made of Ti-6Al-4V alloy with 5.08 cm radius and 2.54 cm thickness. The disk contained a 200 × 400 $\mu$m (semiaxes) oblate spheroidal cavity in the diffusion bond plane with the major axes parallel to the flat disk surfaces. A planar 10 MHz transducer with a radius of 0.635 cm was used in the experiment which was performed in a water immersion tank. The data were collected through $L \rightarrow L$ backscattering measurements at normal incidence to the flat surface of the disk. The data corresponding to the reference pulse were obtained from the front surface reflection of the disk. Both the flaw-backscattered signal and the reference pulse were digitized at 100 MHz. Additional details of the experiment can be found in Thompson and Gray (1983).

The flaw signal $z(k)$ and the reference pulse $p(k)$ are shown in Figure 4.11. The deconvolved signal is shown in Figure 4.12 (a). For comparison purposes, the deconvolved signal using a Wiener filter is shown in Figure 4.12 (b). It is observed that the performance of the algorithm is quite similar to that of the Wiener filter based algorithm.

### Example 3

In this example, the algorithm is used to characterize a layered composite material. The backscattered signal data for this example were obtained using a sample of graphite fiber reinforced epoxy resin composite. The sample was 1.27 cm thick and contained 100 layers with one layer at 90 degrees for every three layers at 0 degrees

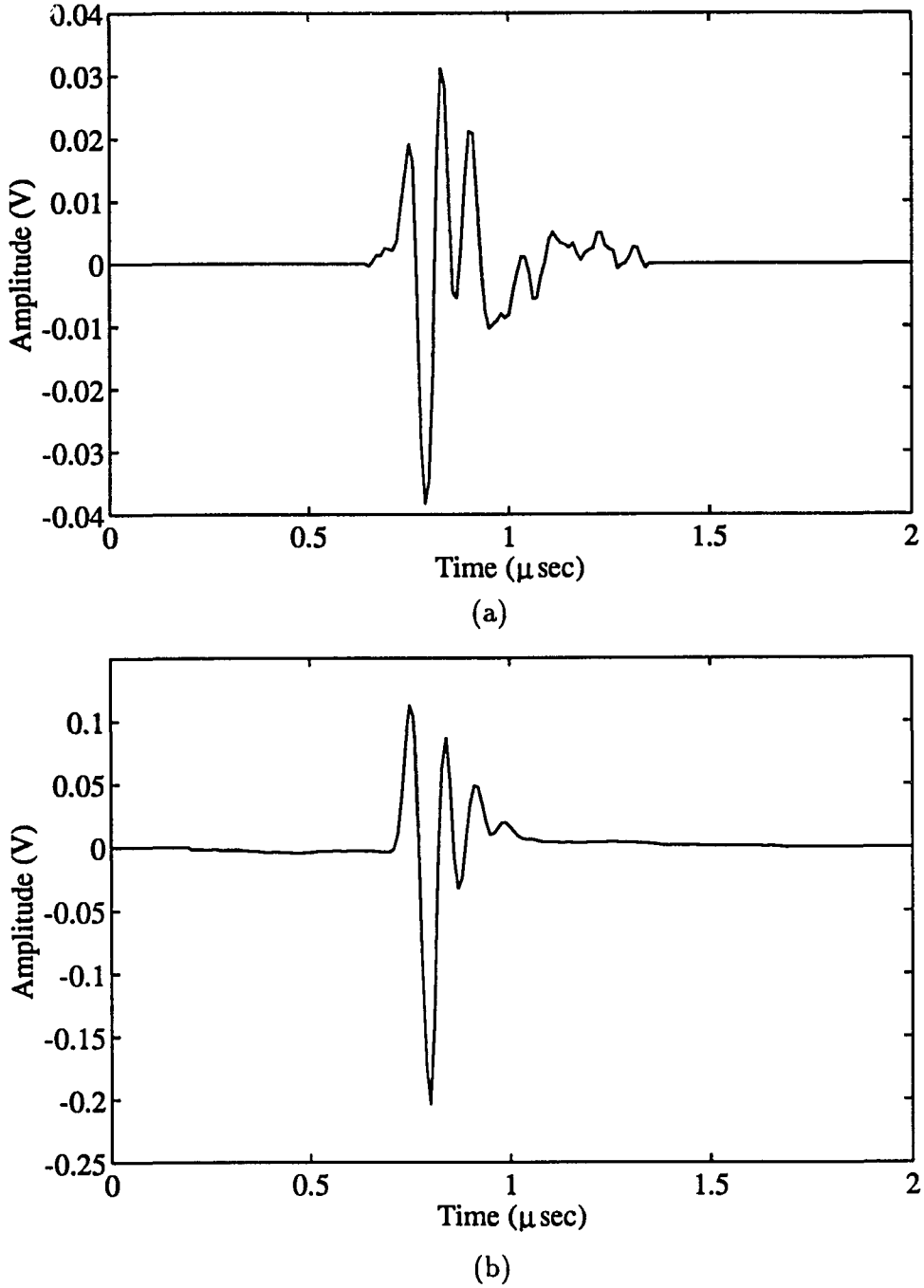


Figure 4.11: Experimental flaw data: (a) flaw signal, (b) reference pulse

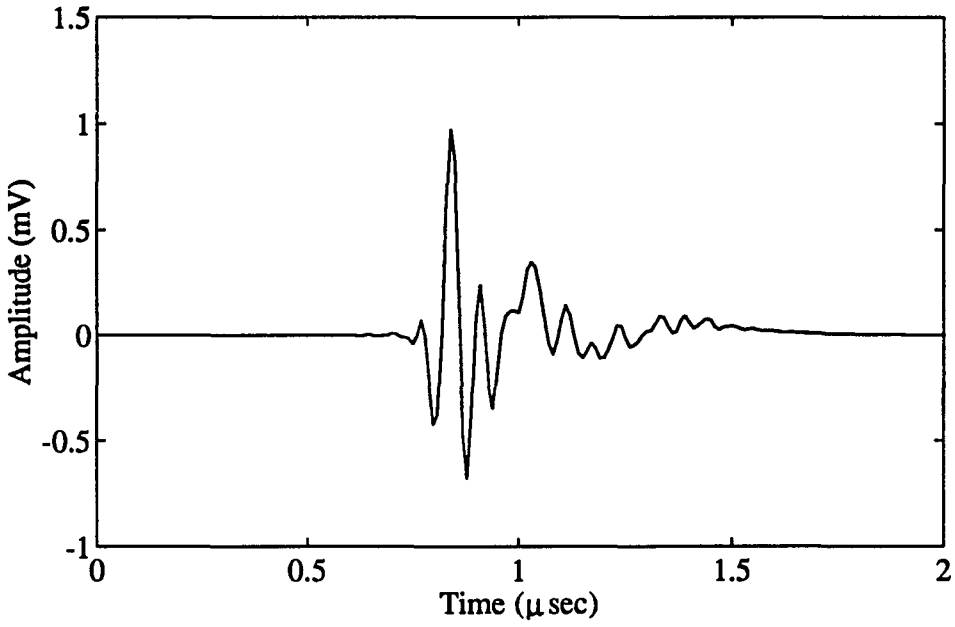


(a)

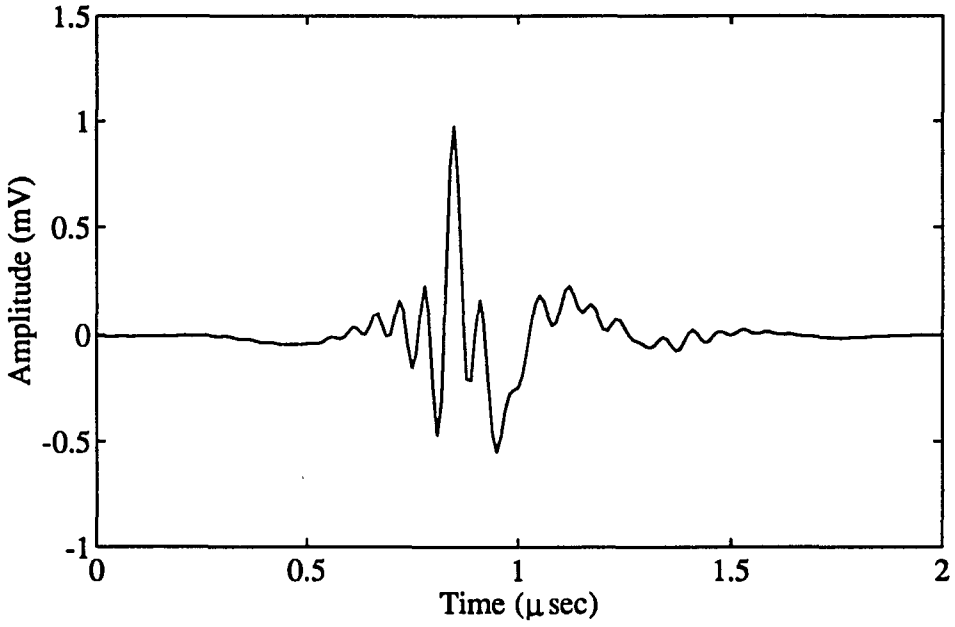


(b)

Figure 4.12: Deconvolution of flaw data: (a) deconvolved signal ($Q/R$=13dB), (b) deconvolved signal using Wiener filter algorithm

($0^3/90$ layup). A 20 MHz planar transducer with 0.318 cm radius was used in the experiment. The data were collected through backscattering measurements with the UT field normally incident on the flat surface of the sample. Both the sample and the transducer were immersed in a water bath and separated by a distance of about 5 cm. The data corresponding to the reference pulse were obtained by replacing the composite sample with a fused-quartz sample and measuring its front surface reflection. Both the reference pulse and the backscattered signal from the composite were digitized at 100 MHz.

The reference pulse $p(k)$ and its spectrum are shown in Figure 4.13. A section of the backscattered signal $z(k)$ and the magnitude spectrum of the backscattered signal are shown respectively in Figure 4.14 (a) and (b). The reflection coefficient sequence $\hat{u}(k)$ and its magnitude spectrum are shown in Figure 4.15. Figure 4.16 is the magnitude spectrum of the reflection coefficient sequence which was estimated by averaging the squared magnitude spectra corresponding to 20 different locations. The spectral peak at about 11.5 MHz can be easily related to the layer thickness (0.0127 cm) and the speed of ultrasound in the material (0.292 cm/$\mu$s).

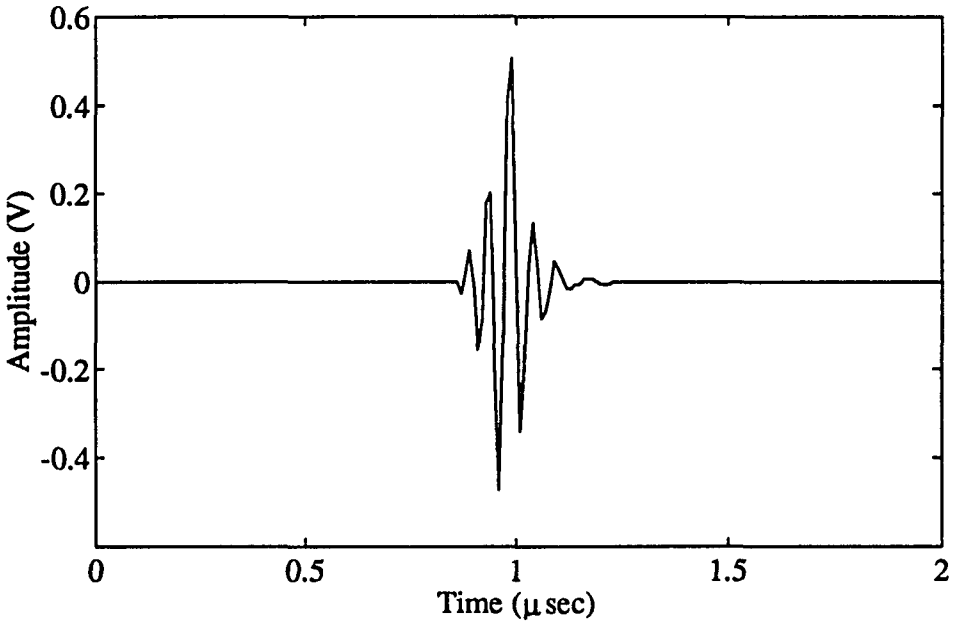


(a)

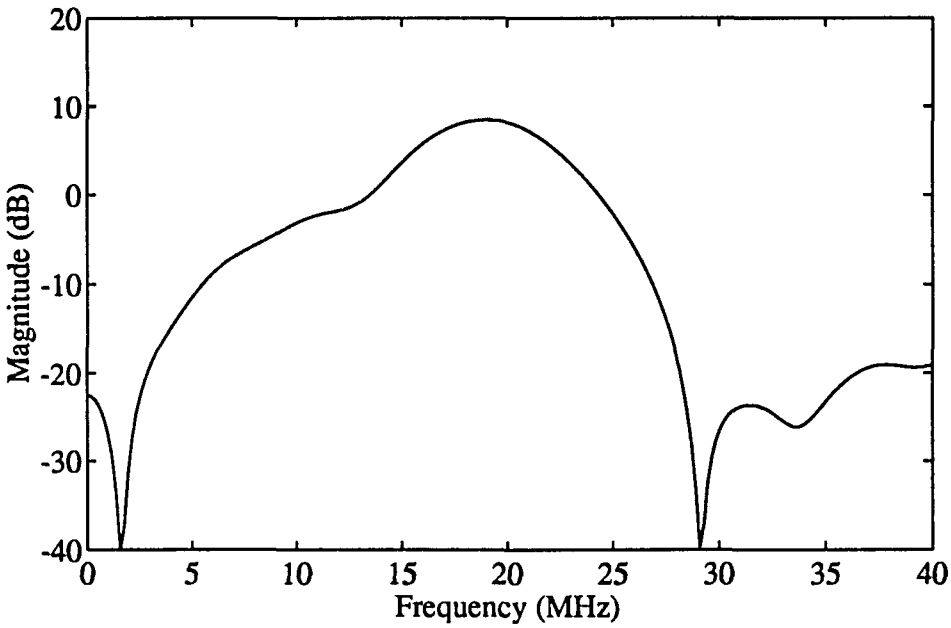


(b)

Figure 4.13: Reference pulse measured from layered material: (a) time domain signal, (b) magnitude spectrum

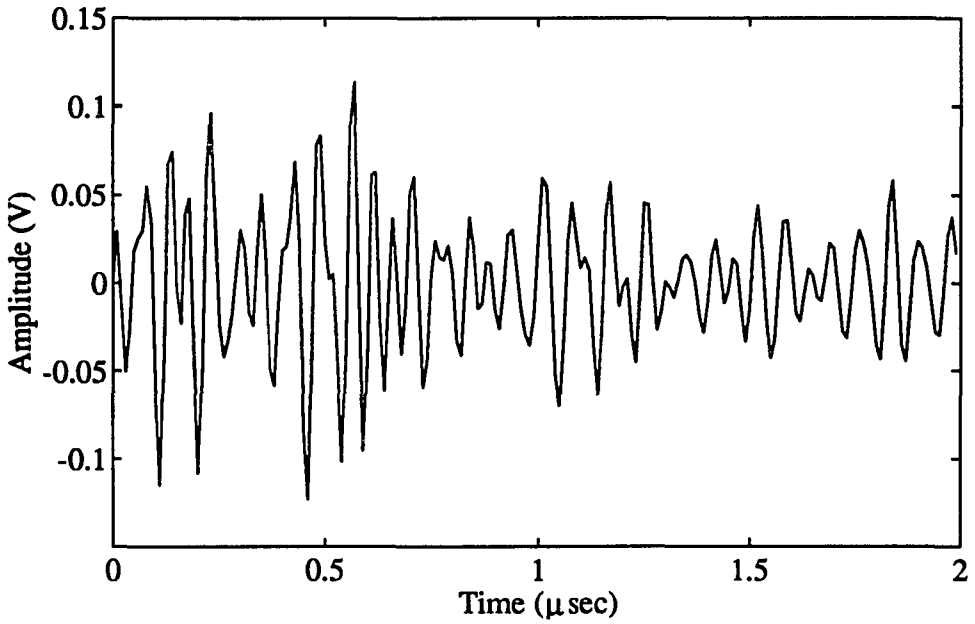


(a)

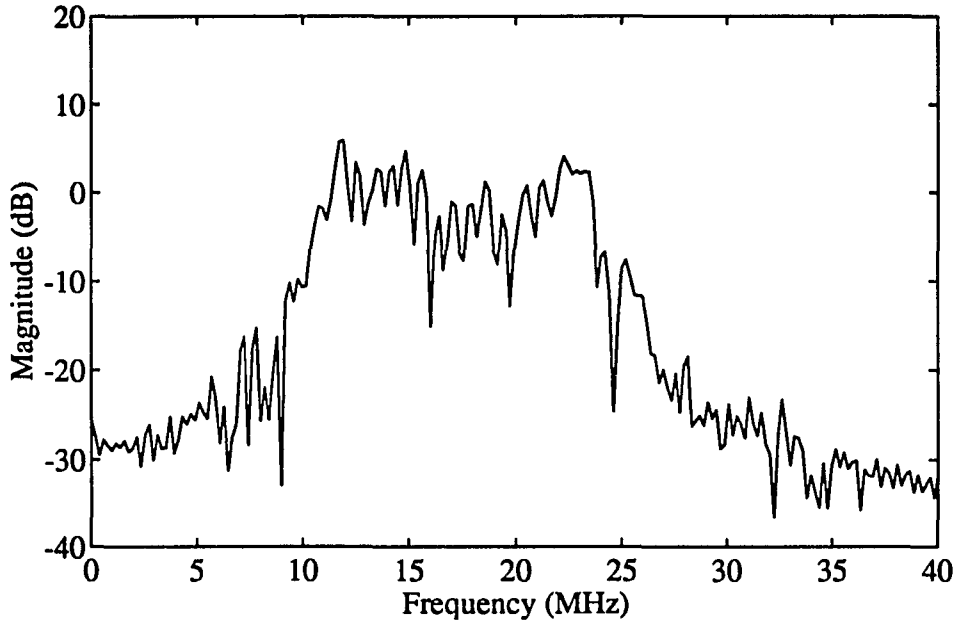


(b)

Figure 4.14: Measured data from layered material: (a) time domain signal, (b) magnitude spectrum

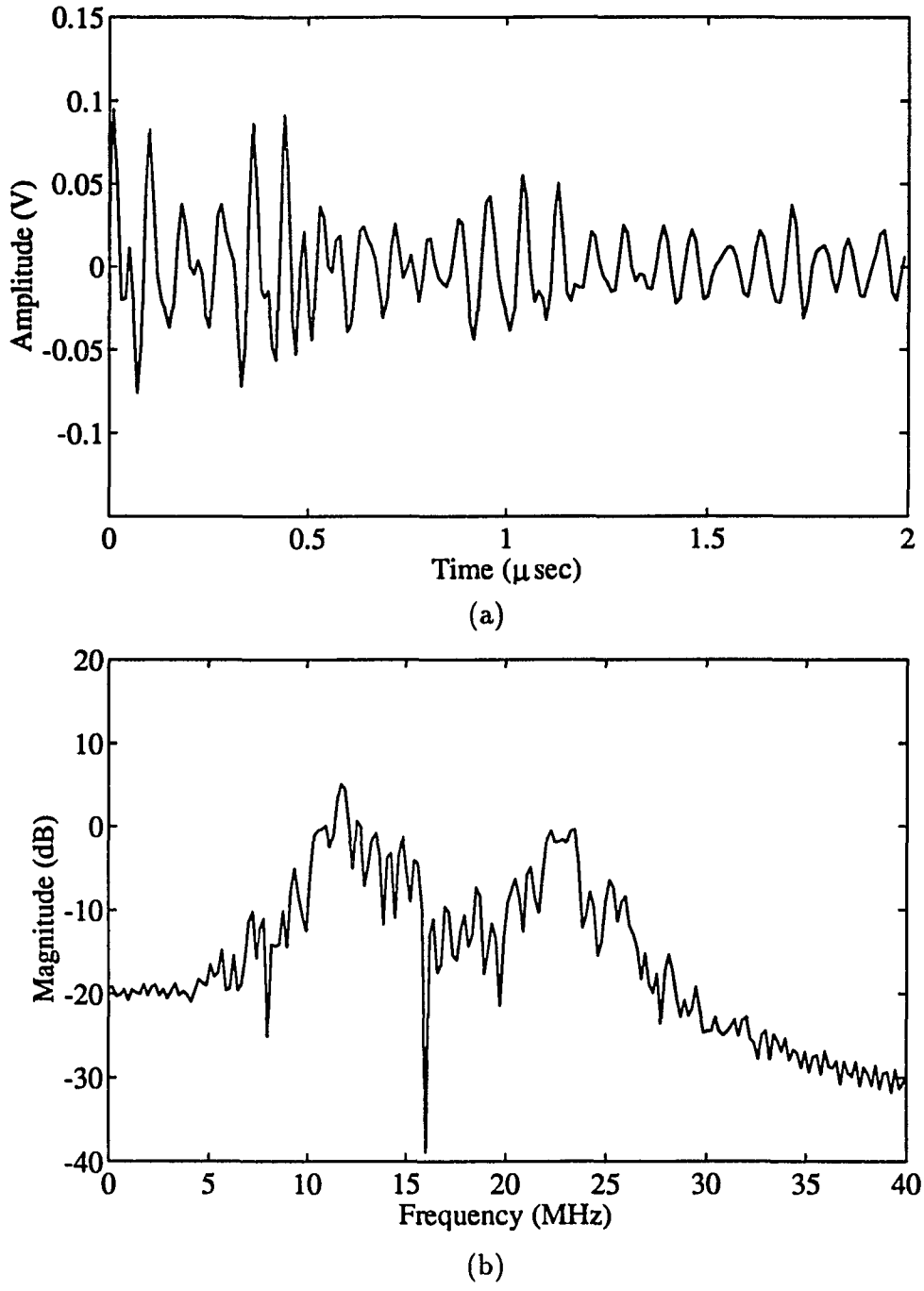


Figure 4.15: Deconvolution of measured data from layered material: (a) deconvolved signal, (b) magnitude spectrum

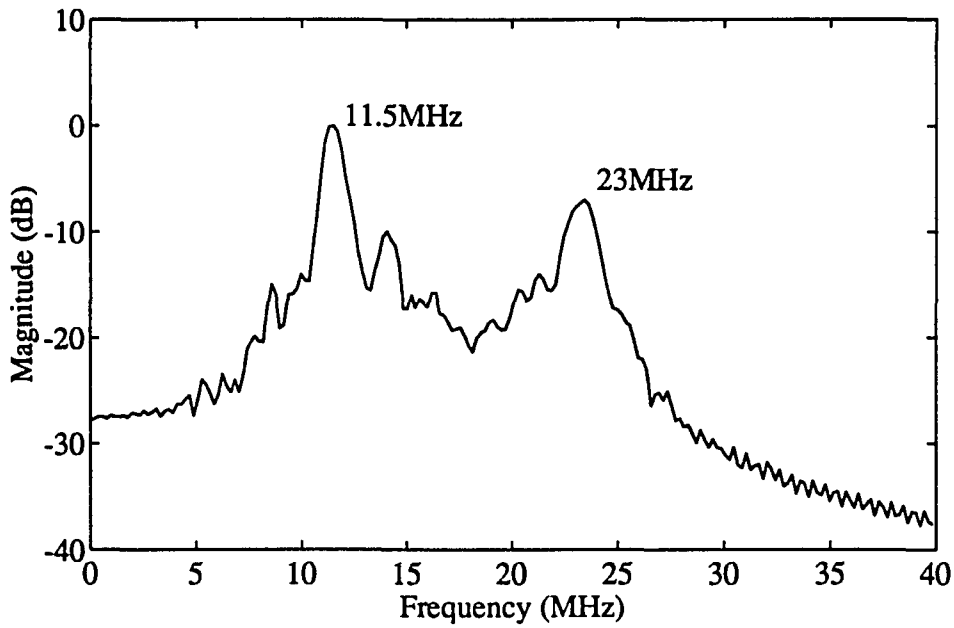


Figure 4.16: Averaged magnitude spectrum of deconvolved data from layered material

# CHAPTER 5. COLORED SEQUENCE ESTIMATION

The Kalman filter based deconvolution algorithm discussed in the previous chapter assumes that the reflection coefficient sequence $u(k)$ is white and provides a minimum variance estimate of this signal. This assumption, however, is not valid when processing grain backscattered data from materials to obtain an estimate of the corresponding reflection coefficient sequences. It is known that the scattered energy due to grains of a material increases with frequency under the usual situation in which the wavelength of the ultrasonic pulse is large compared to the average grain diameter (Krautkrämer, 1991). Thus the signal to be estimated, viz., the reflection coefficient sequence, is also frequency dependent (or colored) illustrating the need for developing algorithms to handle such situations. In this chapter, we propose a simple iterative scheme for this purpose (Yoon and Ramabadran, 1991). The colored system modeling of an ultrasonic signal is discussed first. After describing the proposed iterative scheme, some simulation results are presented.

## Colored System Model

In the deconvolution of an ultrasonic backscattered signal, the signal to be estimated is modeled as the input to a known system and assumed to be white. However, in the nondestructive characterization of materials using ultrasonic techniques, the

material dependent reflection coefficient sequence is known to be colored. In order to estimate such a colored sequence, we model it as the output of a shaping (or coloring) filter excited by a zero-mean, white noise sequence. The shaping filter model equations are given by

$$\mathbf{x}_s(k+1) = \mathbf{F}_s\mathbf{x}_s(k) + \mathbf{G}_s w(k) \tag{5.1}$$

$$u(k) = \mathbf{H}_s\mathbf{x}_s(k) + w(k), \tag{5.2}$$

where $w(k)$ is the white noise input and subscript $s$ denotes the shaping filter. The matrices $\mathbf{F}_s$, $\mathbf{G}_s$, and $\mathbf{H}_s$ together describe the shaping filter and are not known initially. These are determined with the estimates of the shaping filter coefficients during iteration. In modeling an unknown shaping filter, we express the input-output relationship of the shaping filter by means of the $M$-th order AR (Auto-Regression) equation

$$u(k) + \gamma_1 u(k-1) + \gamma_2 u(k-2) + \cdots + \gamma_M u(k-M) = w(k). \tag{5.3}$$

In Equation (5.3), the $M$ shaping filter coefficients, $(\gamma_i,\ i = 1, 2, \cdots, M)$ are not known *a priori*. They are estimated iteratively by the scheme starting from initial values of 0's. Using controllable canonical form realization of (5.3), the shaping filter matrices can be written as

$$\mathbf{F}_s = \begin{bmatrix} 0 & 1 & \cdots & 0 & 0 \\ 0 & 0 & \cdots & 0 & 0 \\ \vdots & \vdots & & \vdots & \vdots \\ 0 & 0 & \cdots & 0 & 1 \\ -\gamma_M & -\gamma_{M-1} & \cdots & -\gamma_2 & -\gamma_1 \end{bmatrix} \tag{5.4}$$

$$\mathbf{G}_s = \begin{bmatrix} 0 & 0 & \cdots & 0 & 1 \end{bmatrix}^T \tag{5.5}$$

$$\mathbf{H}_s = \begin{bmatrix} -\gamma_M & -\gamma_{M-1} & \cdots & -\gamma_2 & -\gamma_1 \end{bmatrix}. \tag{5.6}$$

We now have a cascade of two systems as shown in Figure 5.1. The shaping filter is followed by the system modeling the measurement system. These two systems can be combined to form the augmented system described by the state-space equations.

$$\mathbf{x}_a(k+1) = \mathbf{F}_a\mathbf{x}_a(k) + \mathbf{G}_a w(k) \tag{5.7}$$

$$z(k) = \mathbf{H}_a\mathbf{x}_a(k) + v(k), \tag{5.8}$$

where the subscript $a$ denotes the augmented system. From system model equations (4.2), (4.3) and shaping filter equations (5.1), (5.2), the augmented state vector $\mathbf{x}_a(k)$ and the augmented system matrices $\mathbf{F}_a$, $\mathbf{G}_a$, and $\mathbf{H}_a$ are given by

$$\mathbf{x}_a(k) = \begin{bmatrix} \mathbf{x}(k) \\ \mathbf{x}_s(k) \end{bmatrix} \tag{5.9}$$

$$\mathbf{F}_a = \begin{bmatrix} \mathbf{F} & \mathbf{G}\mathbf{H}_s \\ \mathbf{0} & \mathbf{F}_s \end{bmatrix} \tag{5.10}$$

$$\mathbf{G}_a = \begin{bmatrix} \mathbf{G} \\ \mathbf{G}_s \end{bmatrix} \tag{5.11}$$

$$\mathbf{H}_a = \begin{bmatrix} \mathbf{H} & \mathbf{0} \end{bmatrix}. \tag{5.12}$$

Notice that the input to the augmented system is the zero-mean, white sequence $w(k)$ which can be assumed to be uncorrelated with $v(k)$. This is expressed as

$$E\{w(k)w(j)\} = Q\delta(k-j) \tag{5.13}$$

$$E\{w(k)v(j)\} = 0. \tag{5.14}$$

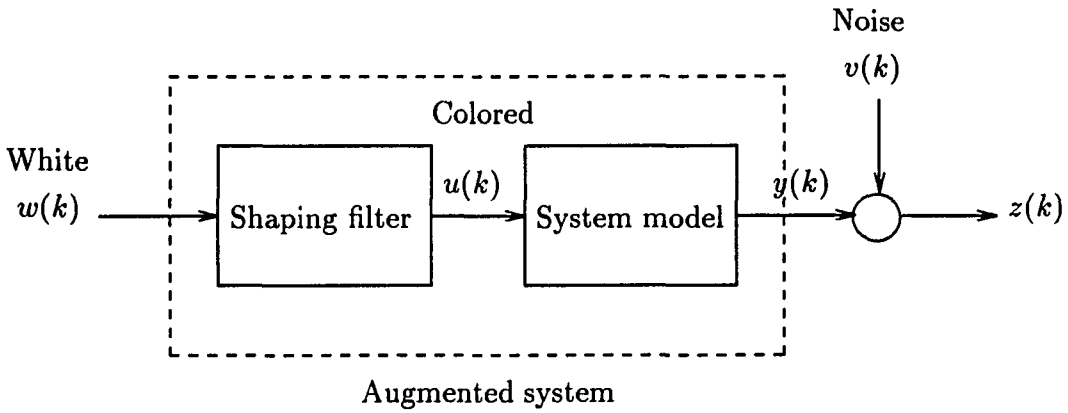


Figure 5.1: Block diagram of augmented system

In the deconvolution of an augmented system, the shaping filter is considered as part of the system and the system order is augmented to $N + M$. The proposed iterative scheme estimates the shaping filter coefficients ($\gamma_i$, $i = 1, 2, \cdots, M$) iteratively using the Kalman filter based deconvolution algorithm.

### Iterative Scheme

In order to estimate the colored input sequence, a simple iterative scheme is proposed. In this scheme, the system model was augmented with a shaping filter excited by a zero-mean white noise sequence. The shaping filter coefficients are initially not known and are estimated using Burg algorithm (Marple, 1987) at each iteration. Figure 5.2 shows a flow diagram of the iterative scheme which works as follows. Initially, the shaping filter coefficients are assumed to be zero which means that the shaping filter is essentially an identity system, i.e., $u(k) = w(k)$. At the beginning of each iteration step, the augmented system is constructed. Next, the Kalman filter based deconvolution algorithm is used to estimate the white noise

sequence $w(k)$, and subsequently the colored input sequence $u(k)$. The shaping filter coefficients for the next iteration are then computed from the current estimate of $u(k)$ using the Burg algorithm. The iteration continues until the change in the values of the shaping filter coefficients is quite small. The estimate of $u(k)$ at the last step is then used as the final estimate.

## Simulation Results

The iterative scheme described in the previous section was tested using simulated data. The signal to be deconvolved $z(k)$ was generated using two system models, viz., a second order and a sixth order model shown in Figure 4.6 and 4.7. These models were chosen to be minimum phase and their impulse responses were designed to approximate an experimentally obtained reference pulse shown in Figure 4.5. The energies of the impulse responses were normalized to be unity. The system input, i.e., colored sequence $u(k)$, was obtained by passing a zero-mean, white, Gaussian noise sequence through a second order shaping filter. Two low pass filters LPF1 and LPF2 and two high pass filters HPF1 and HPF2 were used for this purpose. The AR coefficients of these filters are respectively given by (−0.8, 0.16), (−1.4, 0.49), (0.8, 0.16) and (1.4, 0.49). The frequency responses of the shaping filters and system models are compared in Figure 5.3. It is seen that LPF2 and HPF2 have more coloring effect than LPF1 and HPF1.

In deconvolving $z(k)$ obtained as above, it was assumed that the system model and the measurement noise variance were known exactly. Two deconvolution methods were employed, viz., the Kalman filter based minimum-variance deconvolution (MVD) algorithm described in Chapter 4 and the proposed iterative scheme. In the

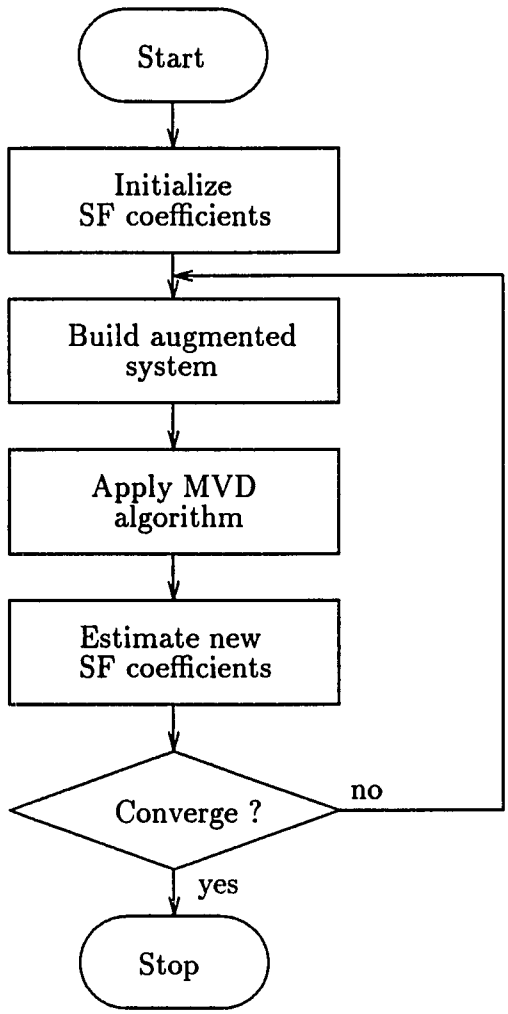


Figure 5.2: Flow diagram of iterative scheme

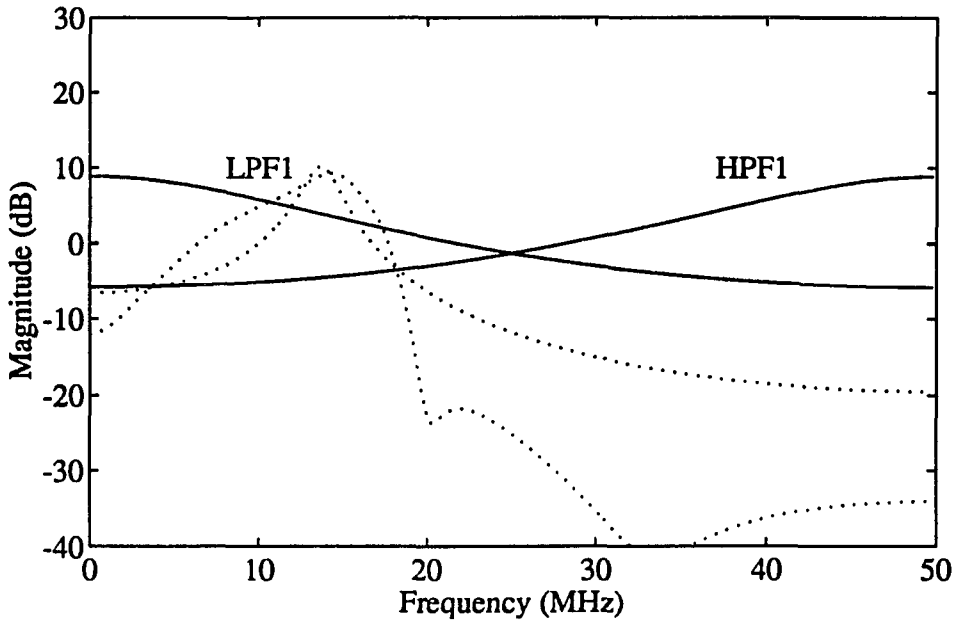


(a)

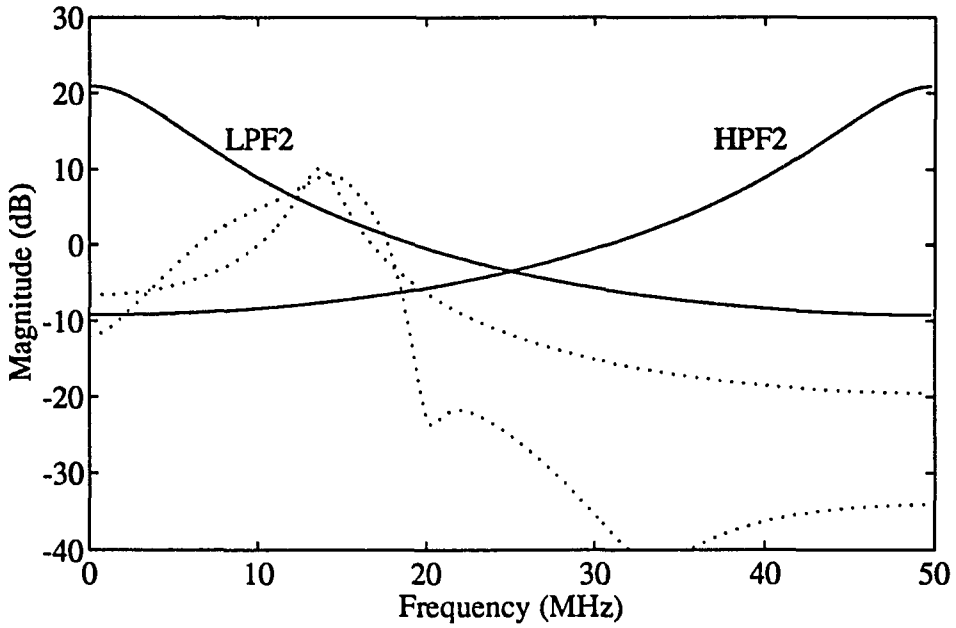


(b)

Figure 5.3: Frequency responses of shaping filters: (a) LPF1 (−0.8, 0.16) and HPF1 (0.8, 0.16), (b) LPF2 (−1.4, 0.49) and HPF2 (1.4, 0.49)

case of the iterative scheme, the order of the shaping filter was taken to be two and the updating of the filter coefficients was terminated after 10 iterations. The results of deconvolution using the two methods, the MVD algorithm and the iterative scheme, are compared in terms of error variance in estimating $u(k)$ expressed as a percentage of the variance of $u(k)$. In this example, the results were averaged for 100 realizations of the colored noise sequence. The results of the deconvolution are shown in Table 5.1. It is seen that the iterative scheme performs better than the MVD algorithm in general for a second order system model, low-pass colored noise, and strong low and high-pass colored noise (LPF2 and HPF2). Its performance, however, is worse for low SNR high-pass colored noise.

It was observed that whenever the iterative scheme performed well, the coefficients of the shaping filter converged to values close to the ideal values, i.e., coefficient values of the filter used in generating the data. Similarly, poor performance of the scheme was typically accompanied by shaping filter coefficient values farther away from their ideal values. The changes in the shaping filter coefficients and error variances for the second order system are plotted in Figures 5.4, 5.5, 5.6 and 5.7, and those for the sixth order system are plotted in Figures 5.8, 5.9, 5.10 and 5.11 for the four different shaping filters, LPF1, HPF1, LPF2 and HPF2. We can see that the error variances are generally decreasing for high-pass filters. However, the error variances for low-pass filters are increasing when SNR is greater than 20 dB. The shaping filter coefficients are converging to some values for the low-pass filters even though SNR is very low. For high-pass filter cases, shaping filter coefficients are converging to the actual values very closely for high SNR, but for low SNR, the converged filter coefficients are completely different from actual values.

Table 5.1: Estimation error variances for different system models and shaping filters

| System model | Coloring filter | SNR (dB) | Error variances | | |
|---|---|---|---|---|---|
| | | | MVD algorithm (%) | Iterative scheme (%) | Exact deconv. (%) |
| 2nd order | LPF1 | 10 | 27.23 | 21.50 | 21.64 |
| | | 20 | 14.40 | 8.90 | 9.35 |
| | | 30 | 3.23 | 2.66 | 2.66 |
| | HPF1 | 10 | 71.84 | 85.84 | 42.38 |
| | | 20 | 18.32 | 5.50 | 5.25 |
| | | 30 | 1.20 | 0.63 | 0.63 |
| 6th order | LPF1 | 10 | 30.86 | 32.19 | 30.25 |
| | | 20 | 21.94 | 19.73 | 20.12 |
| | | 30 | 22.70 | 14.28 | 15.08 |
| | HPF1 | 10 | 94.12 | 95.08 | 92.42 |
| | | 20 | 87.29 | 91.48 | 72.99 |
| | | 30 | 55.45 | 43.06 | 27.61 |
| 2nd order | LPF2 | 10 | 15.31 | 5.71 | 5.81 |
| | | 20 | 6.33 | 2.13 | 2.13 |
| | | 30 | 1.64 | 0.90 | 0.85 |
| | HPF2 | 10 | 79.55 | 7.00 | 7.54 |
| | | 20 | 21.39 | 0.82 | 0.82 |
| | | 30 | 1.02 | 0.10 | 0.10 |
| 6th order | LPF2 | 10 | 22.65 | 11.46 | 10.00 |
| | | 20 | 8.04 | 6.04 | 5.33 |
| | | 30 | 9.53 | 4.30 | 4.20 |
| | HPF2 | 10 | 99.84 | 99.51 | 65.45 |
| | | 20 | 92.60 | 93.11 | 18.61 |
| | | 30 | 54.18 | 4.37 | 3.88 |

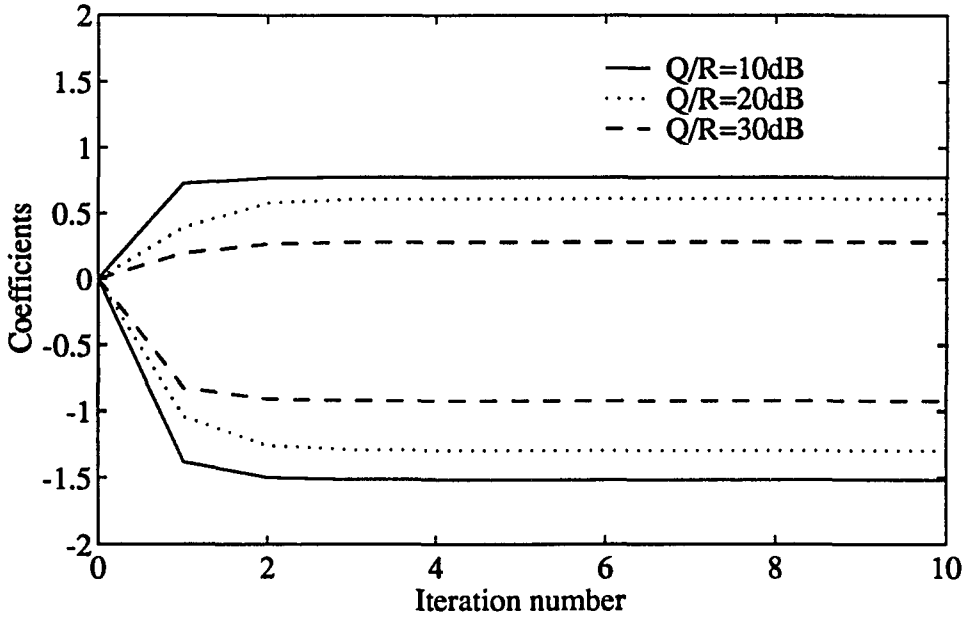


(a)

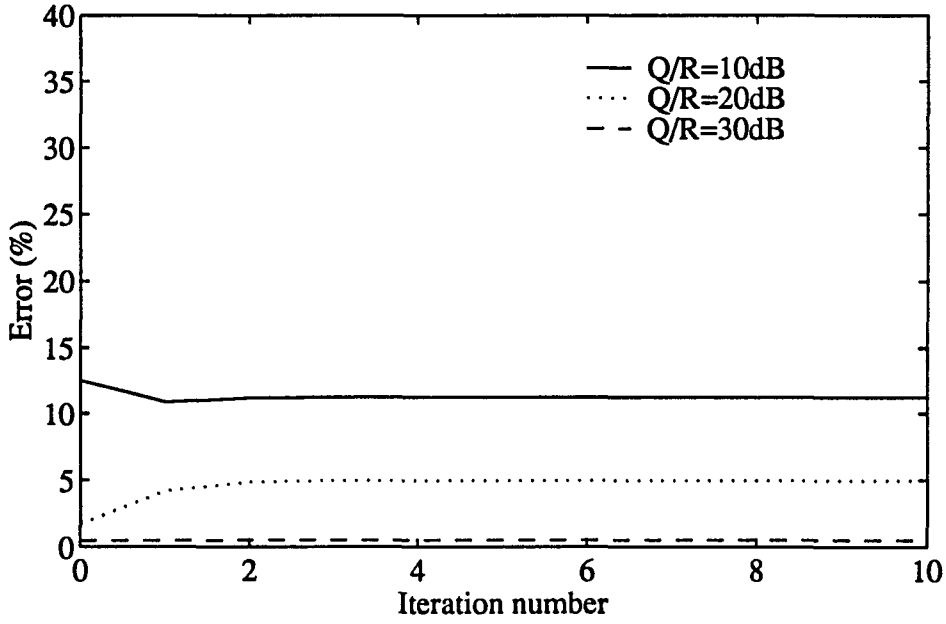


(b)

Figure 5.4: Change in coefficients and error variances for 2nd order system and LPF1: (a) AR coefficients $(-0.8, 0.16)$, (b) error variances

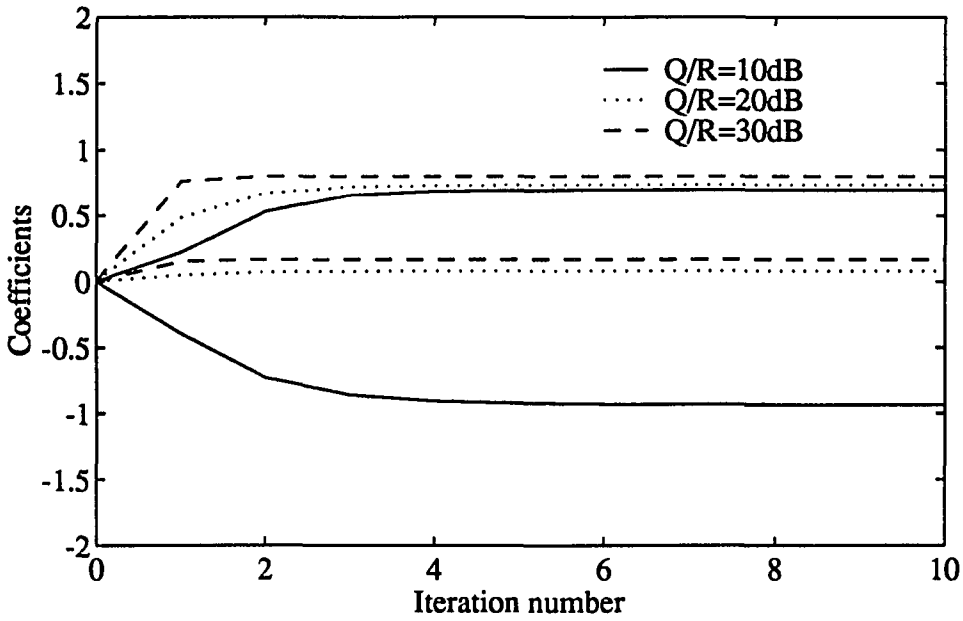


(a)

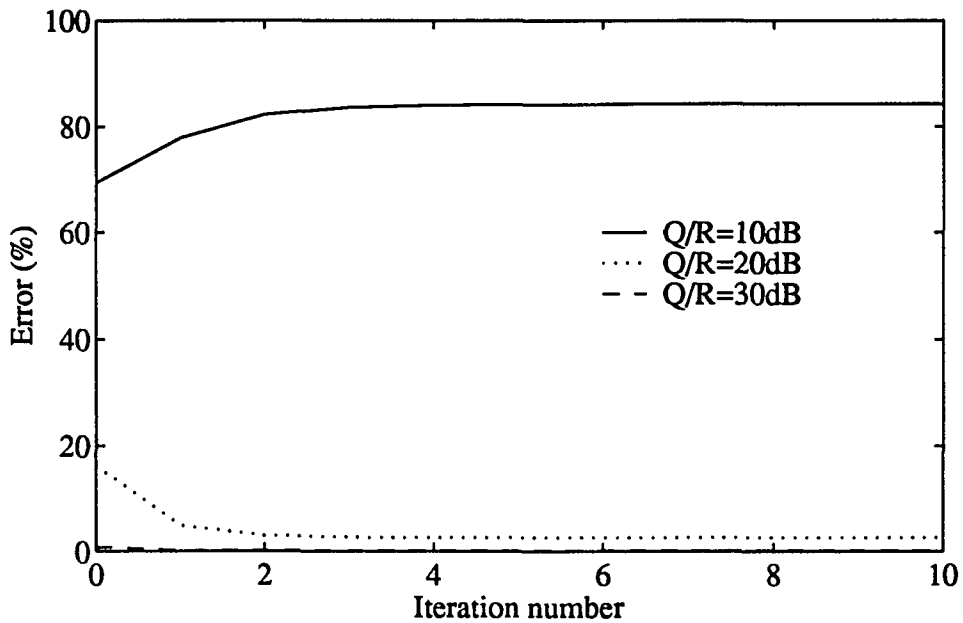


(b)

Figure 5.5: Change in coefficients and error variances for 2nd order system and HPF1: (a) AR coefficients (0.8, 0.16), (b) error variances

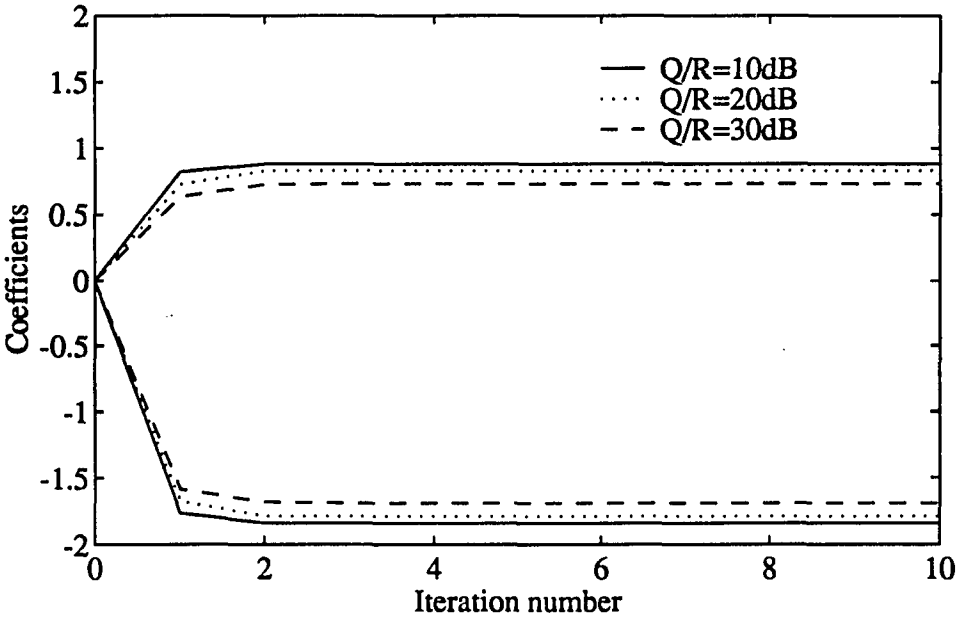


(a)

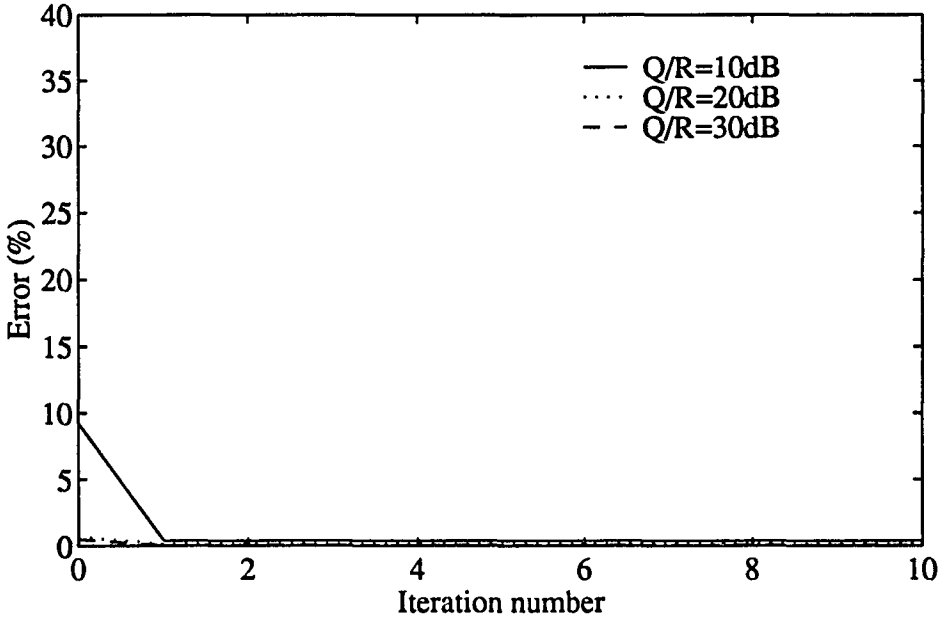


(b)

Figure 5.6: Change in coefficients and error variances for 2nd order system and LPF2: (a) AR coefficients (−1.4, 0.49), (b) error variances

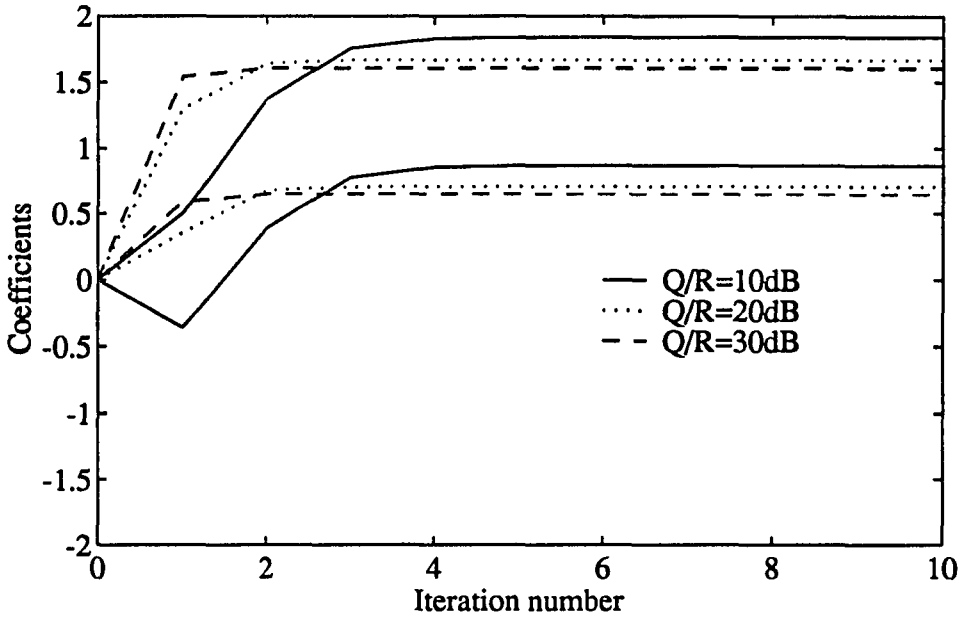


(a)

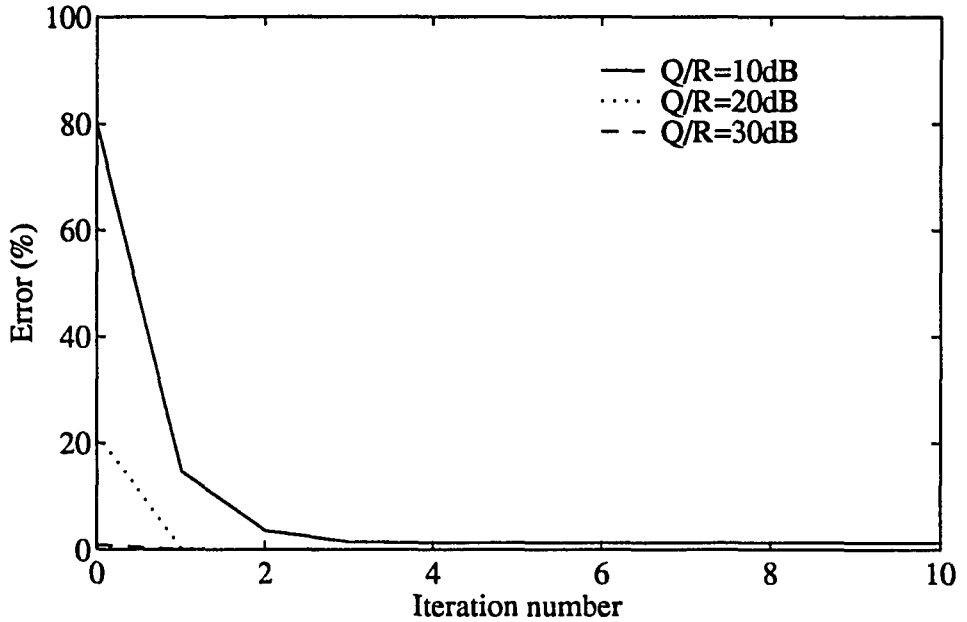


(b)

Figure 5.7: Change in coefficients and error variances for 2nd order system and HPF2: (a) AR coefficients (1.4, 0.49), (b) error variances

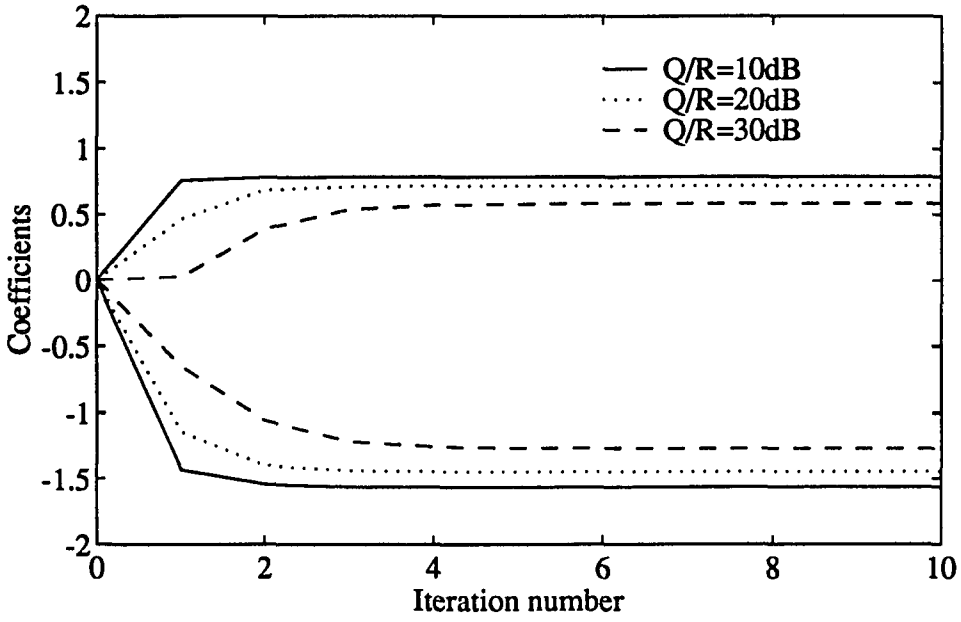


(a)

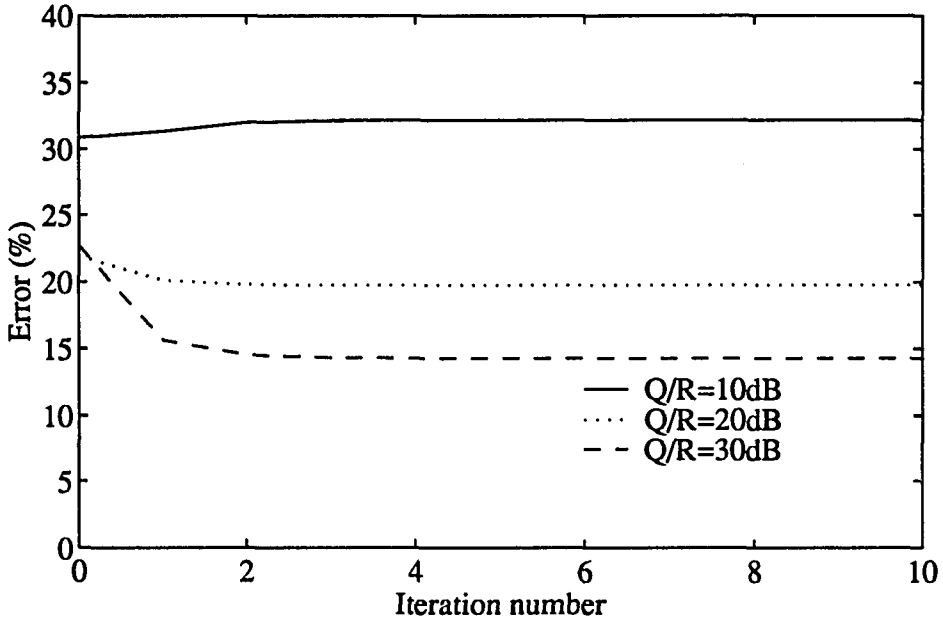


(b)

Figure 5.8: Change in coefficients and error variances for 6th order system and LPF1: (a) AR coefficients (−0.8, 0.16), (b) error variances

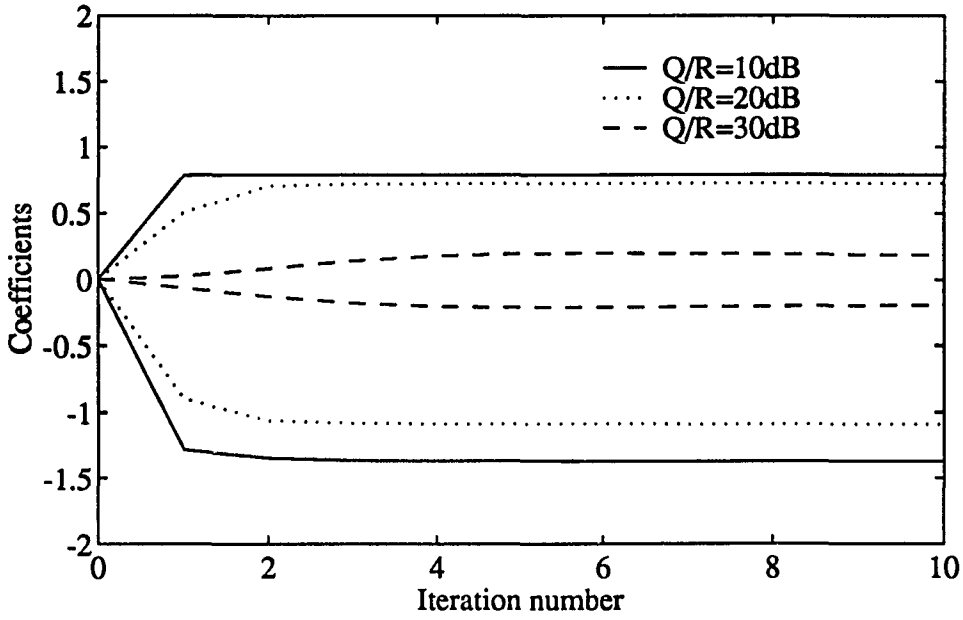


(a)

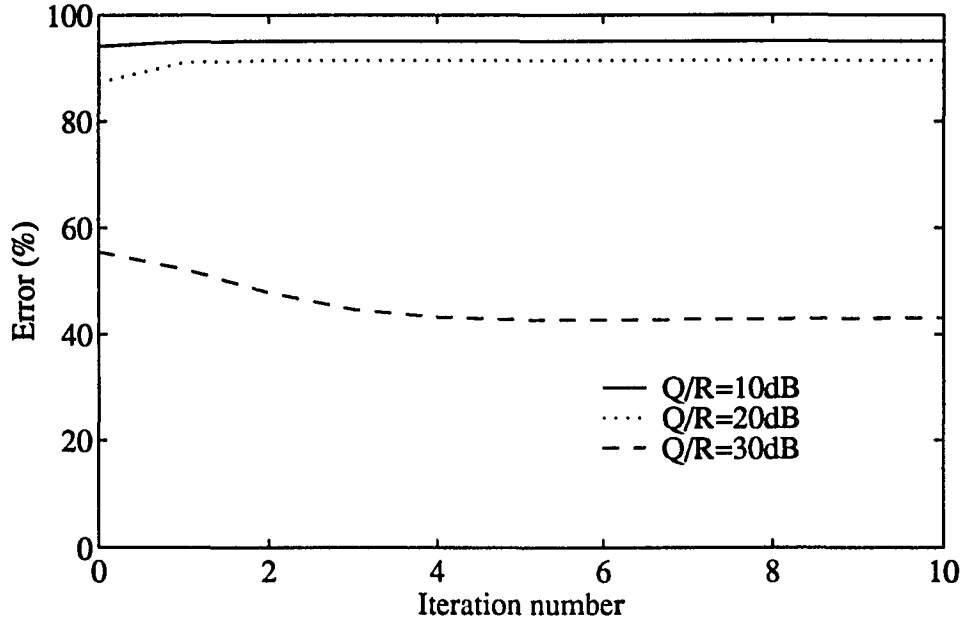


(b)

Figure 5.9: Change in coefficients and error variances for 6th order system and HPF1: (a) AR coefficients (0.8, 0.16), (b) error variances

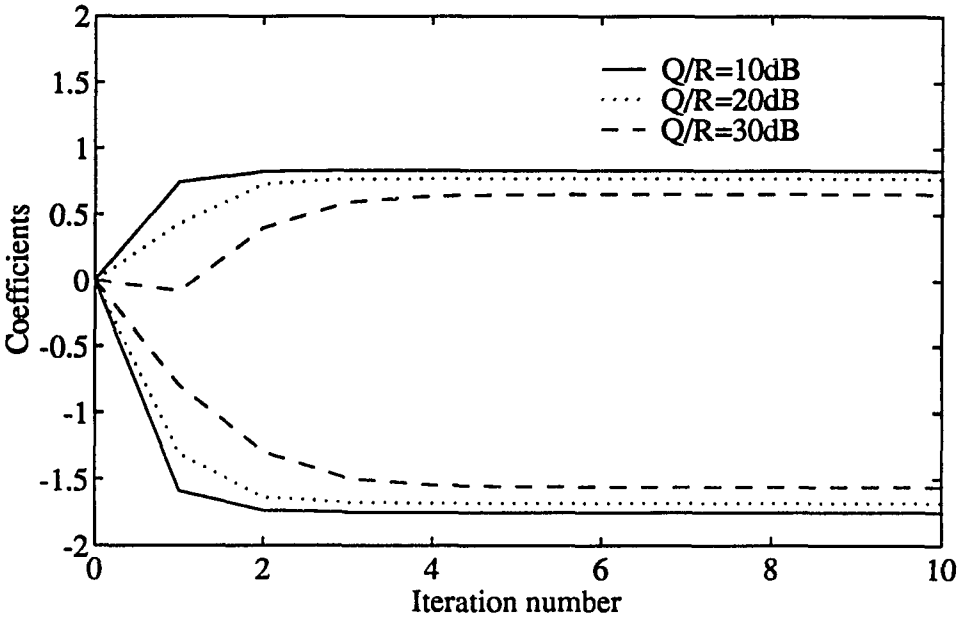


(a)

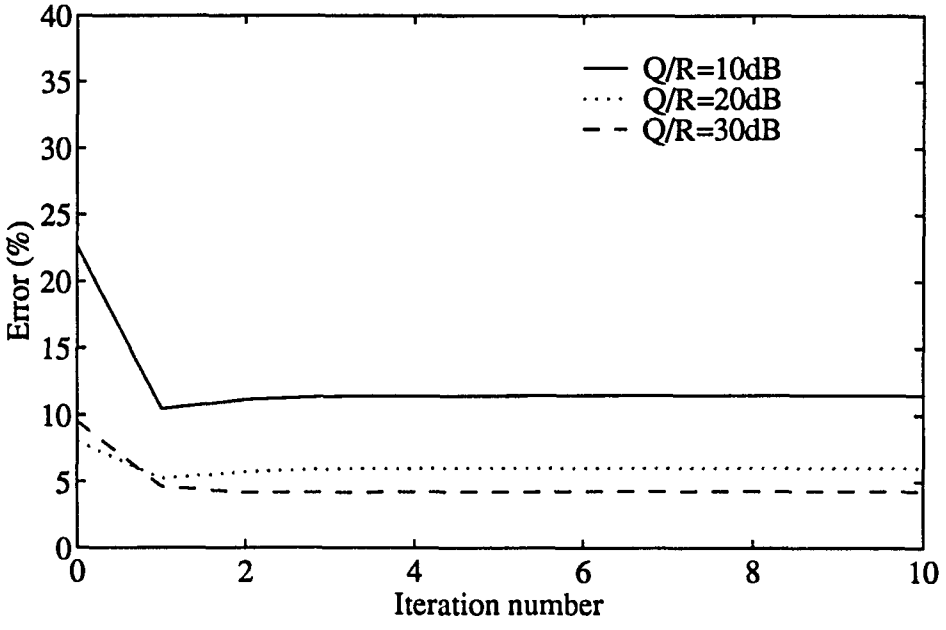


(b)

Figure 5.10: Change in coefficients and error variances for 6th order system and LPF2: (a) AR coefficients (−1.4, 0.49), (b) error variances

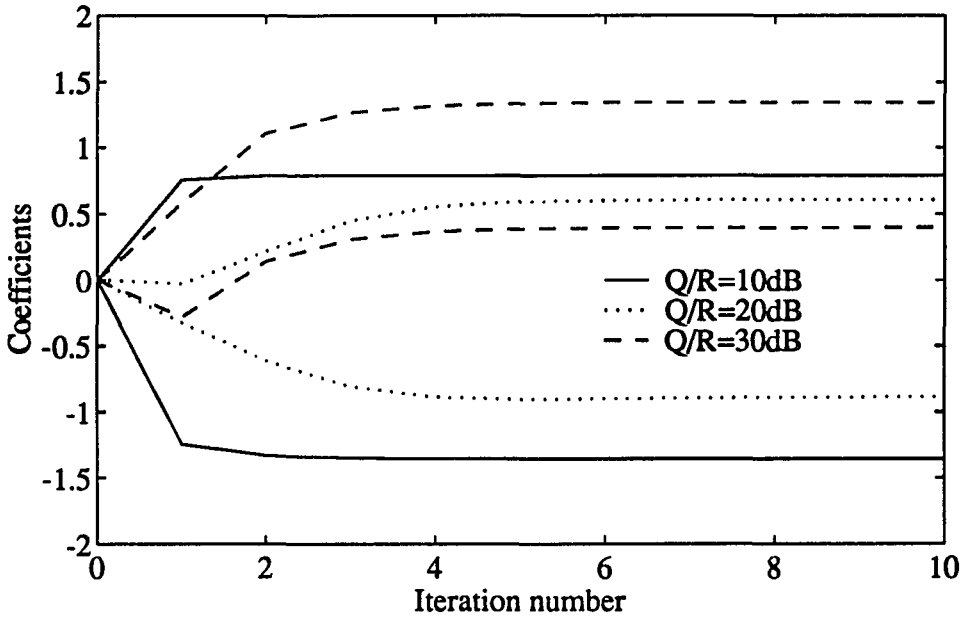


(a)

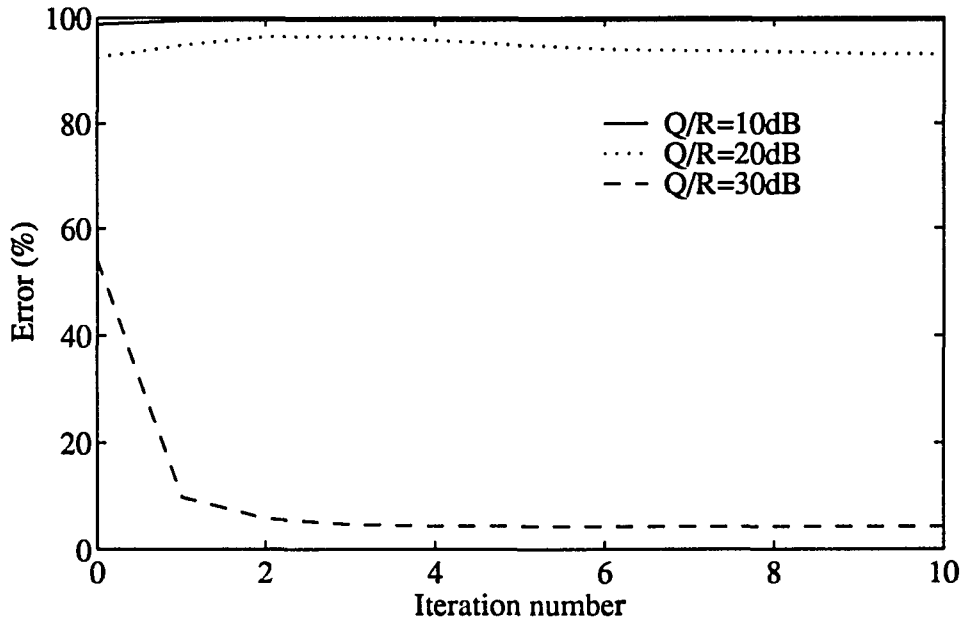


(b)

Figure 5.11: Change in coefficients and error variances for 6th order system and HPF2: (a) AR coefficients (1.4, 0.49), (b) error variances

# CHAPTER 6. SPACE VARYING DECONVOLUTION

In ultrasonic NDE of materials, deconvolution techniques are widely used to improve time/space resolution, minimize spectral coloring, and compensate for different experimental settings, e.g., transducer variations, pulser-receiver energy/damping settings, etc. The reference signal that is used for deconvolution is typically obtained as the front (or back) surface echo from a suitable sample under conditions identical to those used in acquiring the signal to be processed (deconvolved). When the signal to be processed is acquired from an attenuating medium, the effect of signal attenuation should be appropriately accounted for in the deconvolution technique. If the signal arises from a localized inhomogeneity as in the case of flaw scattered signals, this is easily accomplished by suitably modifying the reference signal; for instance, in the Wiener filter based deconvolution technique (Thompson and Gray, 1983), the frequency dependent attenuation corresponding to the flaw location is determined and incorporated into the reference signal spectrum. When the inhomogeneities are distributed throughout the material as in the case of grain backscattered signals, the correction for attenuation should vary along the depth of the material. A suitable deconvolution technique for incorporating such correction is based on the Kalman filter (Ramabadran and Yoon, 1991; Yoon and Ramabadran, 1992). In this technique, the reference signal and the signal to be processed are modeled respectively as the

impulse response of a system and the system output. The input to the system is the deconvolved signal that has to be estimated. The Kalman filter algorithm processes the data sequentially and its formulation allows the system parameters to change at each step. This property can be taken advantage of in providing varying amounts of correction for attenuation along the depth of the material.

In this chapter, we investigate the use of a model parameter interpolation method to provide suitable correction for space varying attenuation (Yoon and Ramabadran, 1993). System models (AR or ARMA) are first built for the front and back surface echoes obtained from a suitable sample. The parameters of these models are then interpolated to obtain models corresponding to intermediate depths. The impulse responses of the interpolated models represent the reference signals corrected for attenuation. The effectiveness of this approach is evaluated using experimentally obtained signals from copper samples of different thicknesses (1/4, 1/2, 3/4 and 1 inches).

## Space Varying System Model

In the Kalman filter based deconvolution technique, the signal to be processed, e.g., grain backscattered signal, is modeled as Equation (4.1). We can rewrite this equation in space varying form to get

$$\begin{aligned} z(k) &= y(k) + v(k) \\ &= p_k(j) * u(k) + v(k) \\ &= \sum_{j=0}^{k} p_k(j) u(k-j) + v(k), \end{aligned} \tag{6.1}$$

where $k$ denotes the sample index, $*$ denotes convolution, $z(k)$ is the measured signal to be processed, $v(k)$ is the measurement noise, $p_k(j)$ is the space varying reference signal, and $u(k)$ is the deconvolved signal to be estimated. If we regard $p_k(j)$ as the space varying model of a system and $u(k)$ as the system input, the measured signal $z(k)$ is just the system output $y(k)$ corrupted by the additive noise $v(k)$. Using state-space notation, Equation (6.1) can be expressed as follows:

$$\mathbf{x}(k+1) = \mathbf{F}_k\mathbf{x}(k) + \mathbf{G}_k u(k) \tag{6.2}$$

$$z(k) = \mathbf{H}_k\mathbf{x}(k) + v(k), \tag{6.3}$$

where $\mathbf{x}(k)$ is the $N \times 1$ system state vector, $\mathbf{F}_k$ is the $N \times N$ state transition matrix, $\mathbf{G}_k$ is the $N \times 1$ input matrix, and $\mathbf{H}_k$ is the $1 \times N$ measurement matrix. The matrices $\mathbf{F}_k$, $\mathbf{G}_k$ and $\mathbf{H}_k$ which describe the space varying system are determined from the space varying reference signal $p_k(j)$.

In the state-space formulation of an ultrasonic backscattered signal, the input $u(k)$ and the measurement noise $v(k)$ are assumed to be zero-mean, white noise sequences with respective variances of $Q$ and $R$ and to be mutually uncorrelated. Mathematically, these assumptions are expressed as

$$E\{u(k)u(j)\} = Q\delta(k-j) \tag{6.4}$$

$$E\{v(k)v(j)\} = R\delta(k-j) \tag{6.5}$$

$$E\{u(k)v(j)\} = 0, \tag{6.6}$$

where $E\{\cdot\}$ is the expectation operator and $\delta(\cdot)$ is the Kronecker delta function.

Two of the popular system models to describe a system are the ARMA (Auto-Regressive Moving Average) and the AR (Auto-Regressive) models. The difference

equation relating the input and output of an $N$-th order ARMA model is given by

$$y(j) + \alpha_{1,k}y(j-1) + \alpha_{2,k}y(j-2) + \cdots + \alpha_{N,k}y(j-N)$$
$$= \beta_{1,k}u(j-1) + \beta_{2,k}u(j-2) + \cdots + \beta_{N,k}u(j-N), \quad (6.7)$$

where $j$ is the sample index, $k$ is space index, and ($\alpha_{i,k}$ and $\beta_{i,k}$, $i = 1, 2, \cdots, N$) represent the space varying system parameters at space index $k$. These parameters are determined from the parameters of space invariant reference signals, $p_0(j)$ and $p_L(j)$, by an interpolation method. The space-invariant reference signals $p_0(j)$ and $p_L(j)$ are obtained from the front and back surface echoes, and the system parameters of these signals are chosen to minimize the average squared errors between $p_0(j)$, $p_L(j)$ and the system impulse responses at $k = 0, L$, i.e., $y(j)$'s when $u(j)$'s are the unit sample sequences. This is accomplished using a nonlinear least squares optimization technique, viz., Levenberg-Marquardt method. In $z$-transform notation, the system function of the ARMA model in (4.4) is represented by

$$H_k(z) = \frac{\beta_{1,k}z^{-1} + \beta_{2,k}z^{-2} + \cdots + \beta_{N,k}z^{-N}}{1 + \alpha_{1,k}z^{-1} + \alpha_{2,k}z^{-2} + \cdots + \alpha_{N,k}z^{-N}}. \quad (6.8)$$

The system matrices corresponding to the ARMA model in Equation (6.7) are realized in the controllable canonical form as follows:

$$\mathbf{F}_k = \begin{bmatrix} 0 & 1 & \cdots & 0 & 0 \\ 0 & 0 & \cdots & 0 & 0 \\ \vdots & \vdots & & \vdots & \vdots \\ 0 & 0 & \cdots & 0 & 1 \\ -\alpha_{N,k} & -\alpha_{N-1,k} & \cdots & -\alpha_{2,k} & -\alpha_{1,k} \end{bmatrix} \quad (6.9)$$

$$\mathbf{G}_k = \begin{bmatrix} 0 & 0 & \cdots & 0 & 1 \end{bmatrix}^T \quad (6.10)$$

$$\mathbf{H}_k = \begin{bmatrix} \beta_{N,k} & \beta_{N-1,k} & \cdots & \beta_{2,k} & \beta_{1,k} \end{bmatrix}. \tag{6.11}$$

In the case of an AR system model, Equations (6.9), (6.10) and (6.11) are modified so that $\beta_{1,k} = 1$ and $\beta_{i,k} = 0$ for $i = 2, 3, \cdots, N$.

### Parameter Interpolation

Suppose system parameters ($\alpha_{i,0}$ and $\beta_{i,0}$, $i = 1, 2, \cdots, N$) and ($\alpha_{i,L}$ and $\beta_{i,L}$, $i = 1, 2, \cdots, N$) represent the parameters of the systems obtained respectively using the front and back surface echoes from a suitable sample as reference signals. The system model parameters at any intermediate depth $k$ are then obtained by interpolation of these parameters. The interpolations corresponding to $\alpha_{i,k}$ and $\beta_{i,k}$ are given by the following equations:

$$\alpha_{i,k} = \alpha_{i,0} + f\left(\frac{k}{L}\right)\left(\alpha_{i,L} - \alpha_{i,0}\right) \tag{6.12}$$

$$\beta_{i,k} = \beta_{i,0} + f\left(\frac{k}{L}\right)\left(\beta_{i,L} - \beta_{i,0}\right), \tag{6.13}$$

for $i = 1, 2, \ldots, N$ and $f(\cdot)$ is used to control the type of interpolation, e.g., $f(k/L) = k/L$ corresponds to linear interpolation and $f(k/L) = \sqrt{k/L}$ corresponds to a non-linear interpolation.

If Equation (6.12) is used to interpolate $\alpha_{i,k}$'s, the stability of the resulting system cannot be guaranteed. To overcome this problem, we first convert the $\alpha_{i,k}$'s into an equivalent set of parameters $\gamma_{i,k}$'s called the PARCOR (Partial Correlation) coefficients. These coefficients are interpolated using Equation (6.12) and the resulting values are converted back to $\alpha_{i,k}$'s. Such an interpolated system will always be stable if the systems corresponding to $k = 0$ and $k = L$ are stable. The procedure for

converting $\alpha_{i,k}$'s to $\gamma_{i,k}$'s and vice versa is described below (Proakis and Manolakis, 1988). Let $\{a_m(i),\ i = 1, 2, \cdots, m \text{ and } a_m(0) = 1\}$ denote the coefficients of the denominator polynomial of an $m$-th order system function. The conversion of $\alpha_{i,k}$'s to $\gamma_{i,k}$'s proceeds as follows. First, set

$$a_N(i) = \alpha_{i,k}, \qquad i = 1, 2, \cdots, N. \tag{6.14}$$

Next, for $m = N, N-1, \cdots, 1$, compute

$$\mathsf{k}_m = a_m(m), \tag{6.15}$$

and

$$a_{m-1}(i) = \frac{a_m(i) - \mathsf{k}_m a_m(m-i)}{1 - \mathsf{k}_m^2}, \tag{6.16}$$

for $i = 1, 2, \cdots, m-1$. Then the PARCOR coefficients $\gamma_{i,k}$ are given by

$$\gamma_{i,k} = \mathsf{k}_i, \qquad i = 1, 2, \cdots, N. \tag{6.17}$$

Conversion of $\gamma_{i,k}$'s to $\alpha_{i,k}$'s is done as follows. First, set

$$\mathsf{k}_i = \gamma_{i,k}, \qquad i = 1, 2, \cdots, N. \tag{6.18}$$

Next, for $m = 1, 2, \cdots, N$, compute

$$a_m(m) = \mathsf{k}_m, \tag{6.19}$$

and

$$a_m(i) = a_{m-1}(i) + \mathsf{k}_m a_{m-1}(m-i), \tag{6.20}$$

for $i = 1, 2, \cdots, m-1$. Then $\alpha_{i,k}$'s can be determined as

$$\alpha_{i,k} = a_N(i), \qquad i = 1, 2, \cdots, N. \tag{6.21}$$

The partial correlation coefficient satisfy the condition $|k_m| < 1$ for all $m = 1, 2, \cdots, N$, if the system has all its roots inside the unit circle. So the interpolated system using partial correlation coefficients will always be stable. This property is also used to check the stability of an AR system and is known as Schür-Chon stability test (Proakis and Manolakis, 1988).

## Space Varying Deconvolution

In Chapter 4, we pointed out that the Kalman filter based deconvolution algorithm can handle time (or space) varying situation very easily. This section describes the space varying form of this algorithm. The Kalman filter based deconvolution algorithm consists of two steps. In the first step, the Kalman filter equations are used to extract the innovations $\tilde{z}(k)$ from the measurements $z(k)$. In the second step, the innovations $\tilde{z}(k)$ are smoothed to obtain the minimum variance estimate $\hat{u}(k)$ of reflection coefficient sequence. The recursive Kalman filter equations are given below.

Predictor

$$\hat{\mathbf{x}}(k|k-1) = \mathbf{F}_{k-1}\hat{\mathbf{x}}(k-1|k-1) \tag{6.22}$$

$$\mathbf{P}(k|k-1) = \mathbf{F}_{k-1}\mathbf{P}(k-1|k-1)\mathbf{F}_{k-1}^T + Q\mathbf{G}_{k-1}\mathbf{G}_{k-1}^T \tag{6.23}$$

Innovations

$$\tilde{z}(k|k-1) = z(k) - \mathbf{H}_k\hat{\mathbf{x}}(k|k-1) \tag{6.24}$$

$$\eta(k) = \mathbf{H}_k\mathbf{P}(k|k-1)\mathbf{H}_k^T + R \tag{6.25}$$

Corrector

$$\mathbf{K}(k) = \mathbf{P}(k|k-1)\mathbf{H}_k^T\eta^{-1}(k) \tag{6.26}$$

$$\hat{\mathbf{x}}(k|k) = \hat{\mathbf{x}}(k|k-1) + \mathbf{K}(k)\tilde{z}(k|k-1) \tag{6.27}$$

$$\mathbf{P}(k|k) = \left[\mathbf{I} - \mathbf{K}(k)\mathbf{H}_k\right]\mathbf{P}(k|k-1) \tag{6.28}$$

In these equations, $\hat{\mathbf{x}}(k|k)$ and $\hat{\mathbf{x}}(k|k-1)$ denote respectively the estimate of the state vector $\mathbf{x}(k)$ based on the measurements $z(0)$ through $z(k)$ and $z(0)$ through $z(k-1)$. The corresponding estimation error covariance matrices are denoted respectively as $\mathbf{P}(k|k)$ and $\mathbf{P}(k|k-1)$. Additionally, $\tilde{z}(k|k-1)$ denotes the innovations process, $\eta(k)$ denotes its variance, and $\mathbf{K}(k)$ is called the Kalman gain vector.

The fixed-interval smoothing algorithm can be expressed as

$$\hat{u}(k|L) = Q\mathbf{G}_k^T\mathbf{r}(k|L) \tag{6.29}$$

$$\mathbf{P}_u(k|L) = Q - Q\mathbf{G}_k^T\mathbf{S}(k|L)\mathbf{G}_kQ. \tag{6.30}$$

In these equations, $\hat{u}(k|L)$ is the optimal (minimum-variance) fixed-interval smoothed estimate of $u(k)$ and $\mathbf{P}_u(k|L)$ is its smoothing error variance. The quantity $\mathbf{r}(k|L)$, called the residual state vector, is defined in Equation (4.26). The residual state vector and its covariance matrix $\mathbf{S}(k|L)$ can be computed using the following recursive equations.

$$\mathbf{r}(k|L) = \left[\mathbf{I} - \mathbf{K}(k)\mathbf{H}_k\right]^T\mathbf{F}_k^T\mathbf{r}(k+1|L) + \mathbf{H}_k^T\eta^{-1}(k)\tilde{z}(k|k-1) \tag{6.31}$$

$$\mathbf{S}(k|L) = \left[\mathbf{I} - \mathbf{K}(k)\mathbf{H}_k\right]^T\mathbf{F}_k^T\mathbf{S}(k+1|L)\mathbf{F}_k\left[\mathbf{I} - \mathbf{K}(k)\mathbf{H}_k\right] + \mathbf{H}_k^T\eta^{-1}(k)\mathbf{H}_k, \tag{6.32}$$

where $k = L, L-1, \cdots, 1$, $\mathbf{r}(L+1|L) = \mathbf{0}$, and $\mathbf{S}(L+1|L) = \mathbf{0}$.

## Experimental Results

The effectiveness of the model parameter interpolation method was verified using experimentally obtained signals from copper samples of different thicknesses (1/4,

1/2, 3/4 and 1 inches). Front and back surface echoes obtained from the 1 inch thick sample were used to build the 14-th order ARMA models and 20-th order AR models. The parameters of these models were interpolated to obtain the system models and their impulse responses at depths of 1/4, 1/2 and 3/4 inches. These signals were then compared with experimentally obtained back surface echoes from the 1/4, 1/2 and 3/4 inches thick copper samples.

In obtaining the front and back surface echoes, a 15 MHz focused transducer (radius: 0.25 inches, focal length: 3.5 inches) was used and was adjusted to focus respectively on the front and back surfaces of the samples. The back surface echoes obtained from the samples were normalized by accounting for transmission and reflection coefficients and phase inversion. The front and back surface echo signals obtained from the copper samples and their frequency spectra are shown in Figure 6.1. Figure 6.2 shows the interpolated signals and their frequency spectra using 14-th order ARMA models; Figure 6.3 shows the interpolated signals and their frequency spectra using 20-th order AR models. Table 6.1 compares the performances of the model parameter interpolation method using both AR and ARMA models with the performance of Wiener filter based method. The performance measure is the signal-to-noise ratio (SNR) in dB computed using the actual (measured) back surface echo and the difference between the actual and interpolated signals. The nonlinear weighting function used here is $f(x) = \sqrt{x}$. In the Wiener filter based method, the spectrum of the attenuated signal $F_k(\omega)$ is computed as

$$F_k(\omega) = F_0(\omega)e^{-\alpha(\omega)k}. \tag{6.33}$$

An estimate of the frequency dependent attenuation $\alpha(\omega)$ in Equation (6.33) is ob-

Table 6.1: Comparison of performances of model parameter interpolation method and Wiener filter method

| Interpolation method | SNR | | |
|---|---|---|---|
| | 1/4" BS echo (dB) | 1/2" BS echo (dB) | 3/4" BS echo (dB) |
| ARMA model | | | |
| Linear | 8.48 | 4.93 | 4.46 |
| Nonlinear | 8.16 | 6.58 | 4.46 |
| AR model | | | |
| Linear | 5.28 | 4.62 | 5.86 |
| Nonlinear | 7.43 | 7.70 | 5.70 |
| Wiener filter | | | |
| $Q = 1\%$ | 5.57 | 2.78 | 4.10 |
| $Q = 0.1\%$ | 6.41 | 3.99 | 5.77 |
| $Q = 0.01\%$ | 6.63 | 4.20 | 6.02 |

tained as follows:

$$e^{-\alpha(\omega)L} = \frac{F_L(\omega)F_0^*(\omega)}{|F_0(\omega)|^2 + Q|F_0(\omega)|^2_{\max}}, \tag{6.34}$$

where $F_0(\omega)$ and $F_L(\omega)$ respectively denote the spectra of front and back surface echoes, $*$ denotes complex conjugate, and $Q$ is a desensitizing factor that avoids division by zero. The performance of the Wiener filter method was computed for different values of $Q$ (1%, 0.1%, 0.01%) as shown in Table 6.1.

Both ARMA and AR system models with nonlinear interpolation yield reasonably good results. The parameter interpolation method is especially suited for use with a Kalman filter based deconvolution technique.

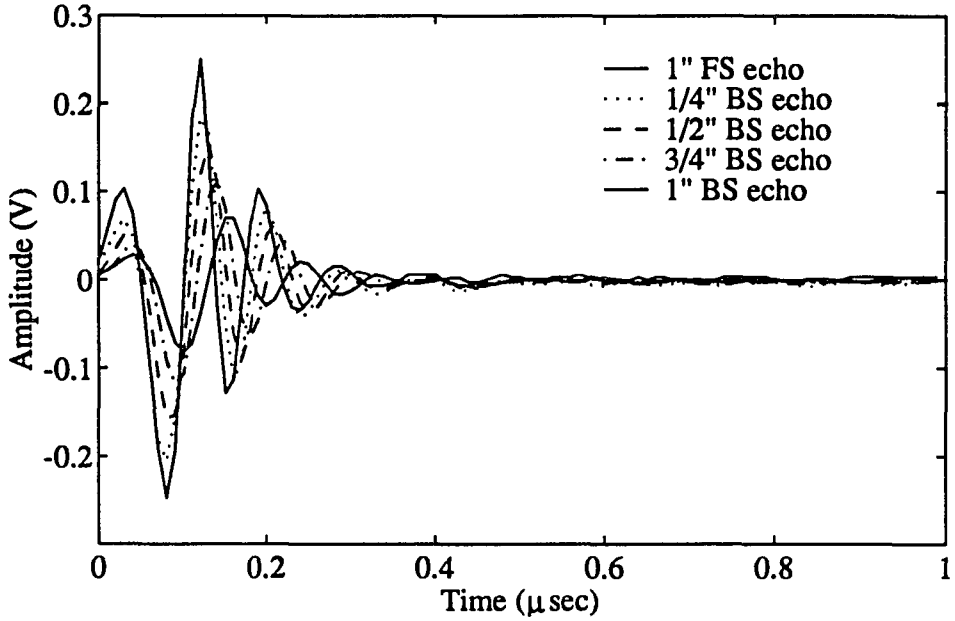


(a)

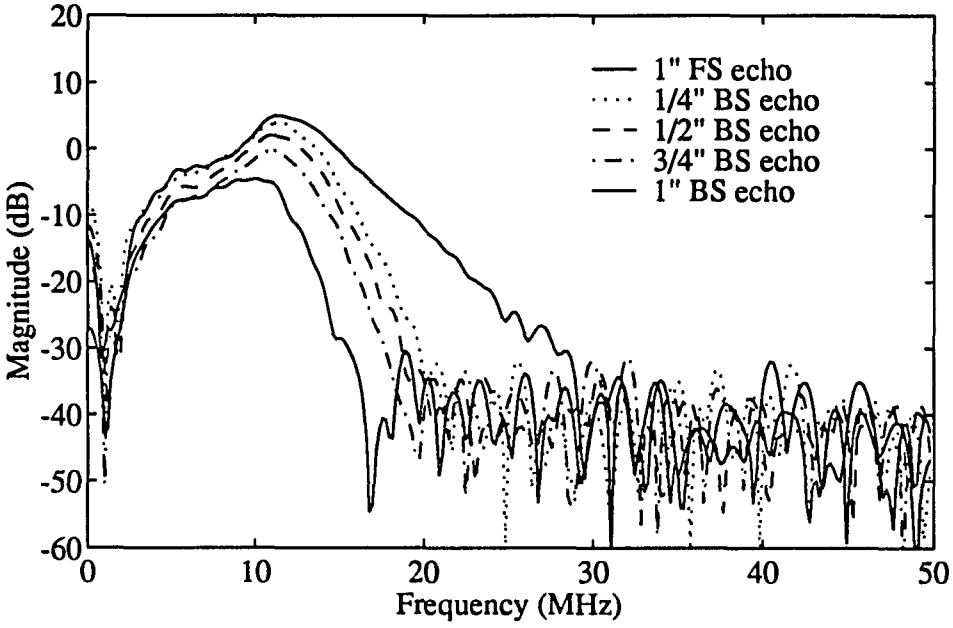


(b)

Figure 6.1: Measured signals from copper samples of different thicknesses: (a) time-domain signals, (b) magnitude spectra

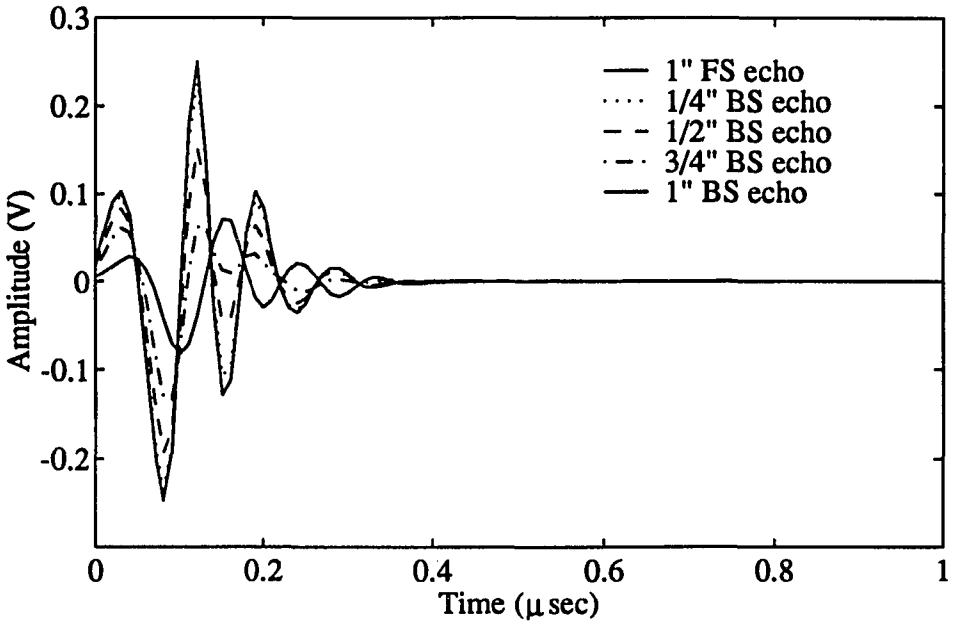


(a)

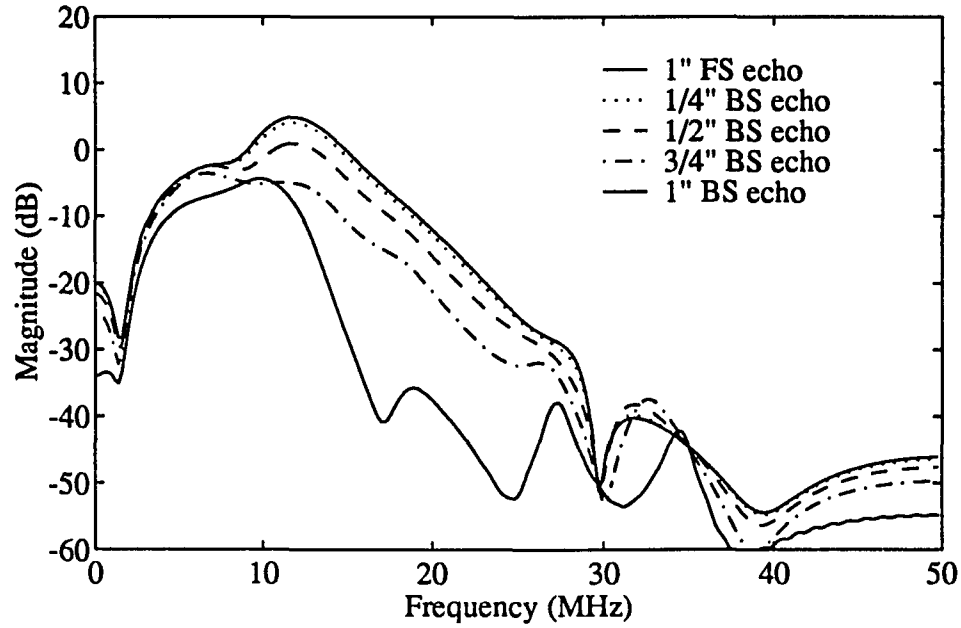


(b)

Figure 6.2: Interpolated signals using 14-th order ARMA models: (a) impulse responses, (b) magnitude spectra

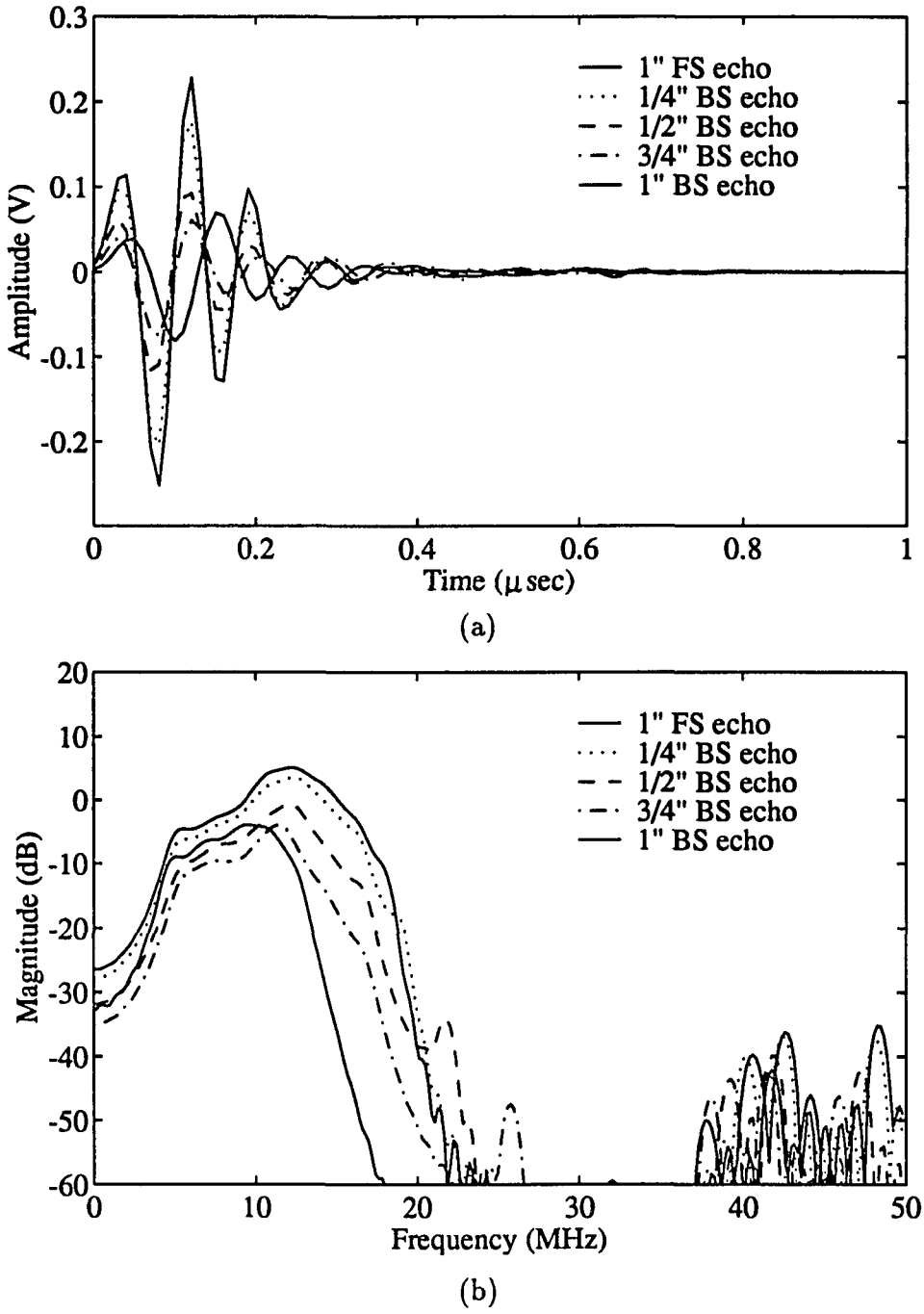


Figure 6.3: Interpolated signals using 20-th order AR models: (a) impulse responses, (b) magnitude spectra

# CHAPTER 7. MATERIAL CHARACTERIZATION USING KALMAN FILTER BASED DECONVOLUTION

The use of grain backscattered ultrasonic signals for the estimation of grain size has been studied extensively (Beecham, 1966; Fay *et al.*, 1976; Goebbels and Holler, 1980; Saniie and Bilgutay, 1986). Several techniques to process the grain backscattered signals and extract information related to grain size have been reported in Saniie and Bilgutay (1986). In this chapter, we describe a new technique to process these signals and extract features that can be used for material characterization (Yoon and Ramabadran, 1992). The technique consists of the three steps: deconvolution, spectrum estimation, and feature extraction. The extracted features are related to the average scattered energy and the rate of change of scattered energy with frequency, both computed within the bandwidth of the ultrasonic transducer. The spectral features so extracted are influenced by the microstructural properties of a material pertaining to scattering, e.g., average grain diameter, and can be used in the characterization of these properties.

In this chapter, we first examine the grain scattering process in some detail and then describe the signal processing steps. Experimental results involving characterization of some pure titanium samples with different grain sizes are next presented. The results include the effect of different spectral estimation methods and windows

sizes on the features.

## Grain Scattering

The scattering of ultrasonic waves at the grain boundaries is influenced by several factors such as grain anisotropy, grain orientation, grain geometry, average grain diameter, and frequency. The effect of grain scattering is best seen through the attenuation of an ultrasonic wave traveling through a material. The frequency-dependent attenuation coefficient $\alpha$ of a material can be expressed as

$$\alpha = \alpha_a + \alpha_s, \tag{7.1}$$

where $\alpha_a$ is the absorption coefficient and $\alpha_s$ is the scattering coefficient (Krautkrämer, 1991). Attenuation due to absorption is relatively small and is caused by the direct conversion of ultrasonic energy into heat. The absorption coefficient is essentially independent of the average grain diameter and varies linearly with frequency $f$ over a wide range as given by

$$\alpha_a = C_1 f, \tag{7.2}$$

where $C_1$ is a constant.

The scattering coefficient, on the other hand, has different expressions depending on the relative values of the average grain diameter $\bar{D}$ and the acoustic wavelength $\lambda$. In the Rayleigh region where $\lambda > \bar{D}$, the scattering coefficient is expressed as

$$\alpha_s = C_2 \bar{D}^3 f^4. \tag{7.3}$$

In the stochastic region where $\lambda \approx \bar{D}$, the scattering coefficient is given by

$$\alpha_s = C_3 \bar{D} f^2. \tag{7.4}$$

In the diffusion region where $\lambda < \bar{D}$, it is given by

$$\alpha_s = C_4 \bar{D}^{-1}. \tag{7.5}$$

The constants $C_2$, $C_3$, and $C_4$ account for factors such as grain anisotropy, grain geometry, and grain orientation. From the above expressions for $\alpha_s$, it can be inferred that the scattered ultrasonic energy as viewed through the frequency window provided by a (broadband) transducer will have different average values and different slopes (rate of change with frequency) depending on the material microstructure as shown in Figure 7.1. Features related to these quantities can therefore be quite useful for material characterization purposes.

## Signal Processing

This section describes a new technique which was developed to process the grain backscattered signals and extract features that can be used for material characterization. This technique consists of the following three steps: (1) deconvolution of the backscattered signal to remove the effect of the measurement system, (2) estimation of the spectrum of the resulting reflection coefficient sequence, and (3) extraction of features from the spectrum related to the average scattered energy and the rate of change of scattered energy with frequency, both computed within the bandwidth of the ultrasonic transducer. The flow diagram of this signal processing technique is shown in Figure 7.2.

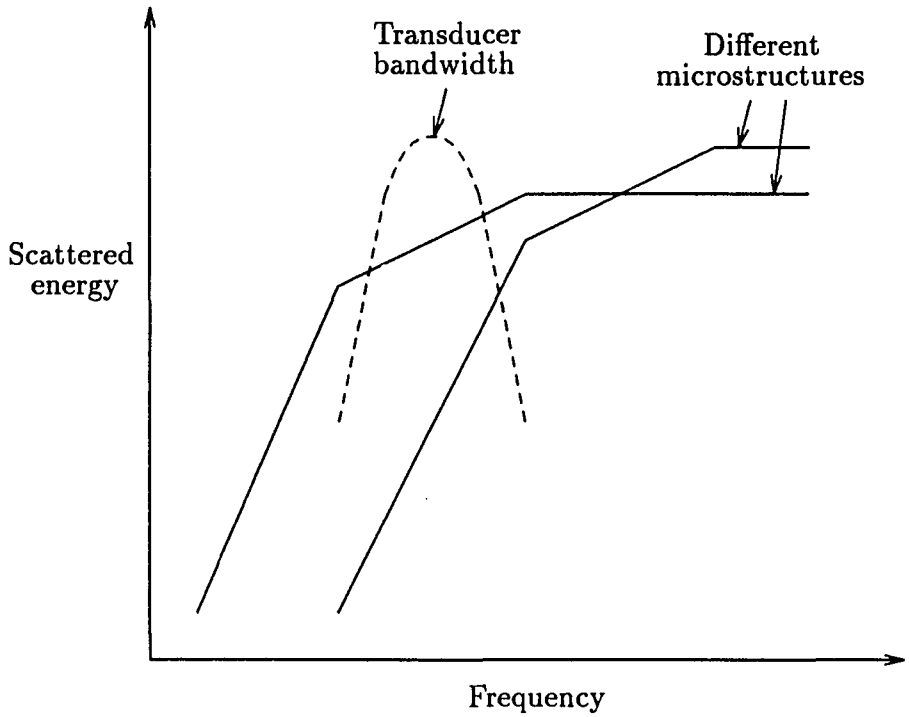


Figure 7.1: Frequency dependent scattered energies of different microstructures

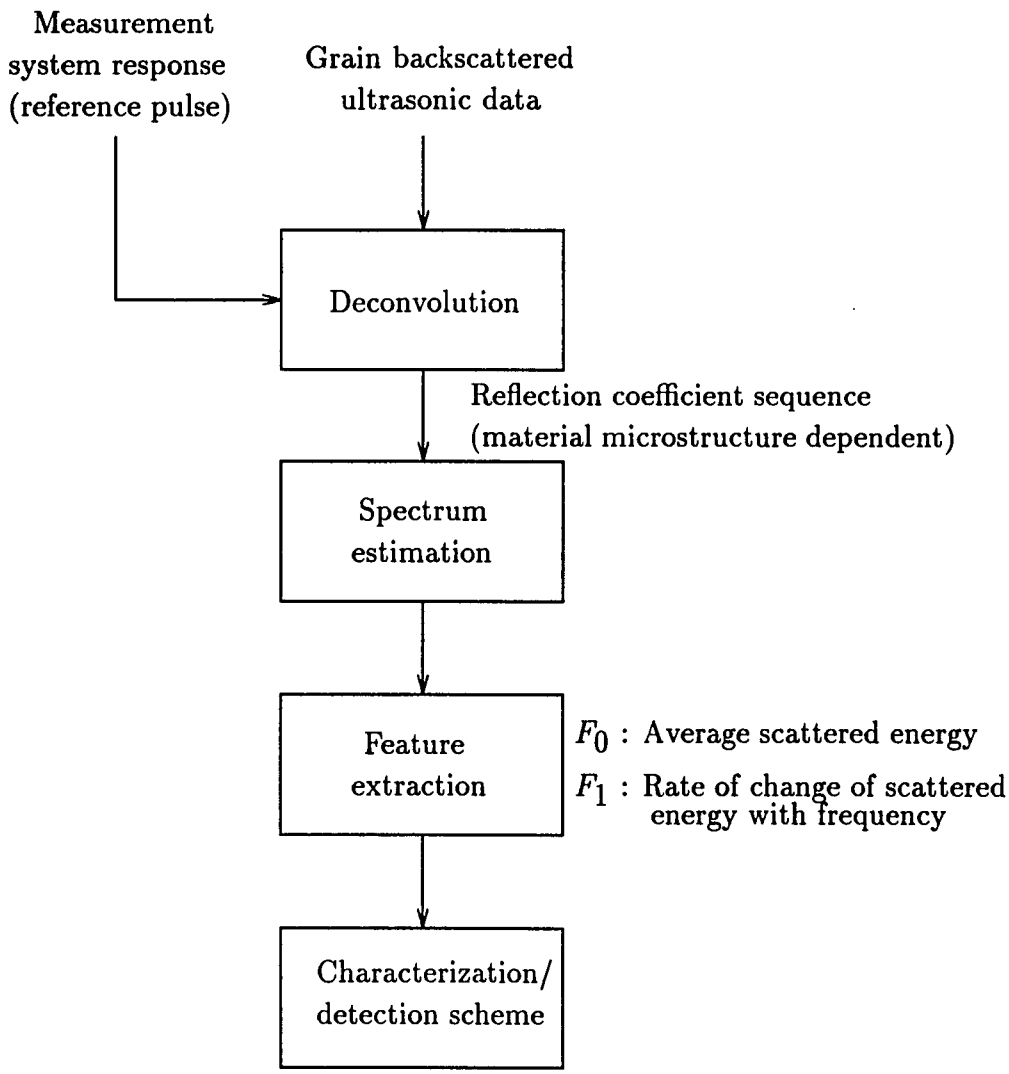


Figure 7.2: Flow diagram of signal processing method

### Deconvolution

The grain backscattered signal obtained from a material sample is obviously colored by the measurement system response. Deconvolution of this signal with the help of a reference pulse (representing the measurement system response) allows us to obtain a signal which is dependent only on the material microstructure. The deconvolution algorithm used here was described in Chapter 4.

### Spectrum estimation

Once the reflection coefficient sequence $\hat{u}(k)$ has been estimated, its spectrum can be obtained using different methods (Kay and Marple, 1981; Marple, 1987). Two methods considered here are the periodogram (PER) method and the Auto-Regressive (AR) method. In the periodogram method, the spectrum of a given sequence of $L$ samples is computed as follows.

$$P_{\mathrm{PER}}(f) = \left| \sum_{k=0}^{L-1} u(k) e^{-j2\pi fk} \right|^2 \tag{7.6}$$

The periodogram method is computationally efficient, but provides a poor estimate when the data record is short, i.e., $L$ is small. In the AR spectrum estimation method, the AR coefficients $a_i$, $i = 1, 2, \cdots, q$ are first computed, and the spectrum is estimated by

$$P_{\mathrm{AR}}(f) = \frac{K}{\left| 1 + \sum_{i=1}^{q} a_i e^{-j2\pi fi} \right|^2}. \tag{7.7}$$

The AR spectrum estimation method generally gives a better estimate when the data record is short.

### Feature extraction

After estimating the spectrum of the reflection coefficient sequence, two features are extracted from it, viz., $F_0$ related to the average scattered energy, and $F_1$ related to the rate of change of scattered energy with frequency. The values of these features are obtained by least-squares fitting a portion of the spectrum within the transducer bandwidth with respectively a zeroth order and a first order polynomial.

## Experimental Results

The signal processing technique described in the previous section was implemented in software: the deconvolution step was implemented through a C language program and the spectrum estimation and feature extraction steps were implemented through the MATLAB package. Backscattered signals were obtained from three pure titanium samples A, B, and C. These samples were prepared using powder metallurgy techniques starting from particles of different sizes. It is believed that the microstructures of these samples differ only in terms of their average grain diameters. The particle sizes used as well as the average grain diameters measured using three different methods are shown in Table 7.1. In the table, diameter is the average maximum grain diameter measured by hand, intercept is the average length of a randomly drawn line that intercepts the grain boundaries and is measured by hand, computer is the average length of a line which is inside the grain boundaries and is randomly drawn using Monte Carlo method by computer. A-scan data were obtained from each titanium sample at ten different locations using a 15 MHz focused transducer (radius: 0.635 cm, focal length: 8.89 cm) inside a water immersion tank. The data were then digitized at a sampling frequency of 100 MHz. In obtaining the grain backscattered

Table 7.1: Particle sizes and average grain diameters of the titanium samples A, B and C

| Sample | Particle size ($\mu$m) | Average grain diameter | | |
|---|---|---|---|---|
| | | Diameter ($\mu$m) | Intercept ($\mu$m) | Computer ($\mu$m) |
| A | $150 \sim 300$ | 44.94 | 24.52 | 25.42 |
| B | $125 \sim 150$ | 39.05 | 30.26 | 20.48 |
| C | $106 \sim 125$ | 48.85 | 22.88 | 26.78 |

data, the transducer was focused at the center of the samples. A reference pulse was obtained by focusing the transducer at the front surface of a sample. An experimental setup for measuring grain backscattered signal and reference pulse is shown in Figure 7.3. In this setup, the waterpath $D_w$ to focus transducer into the middle of sample is determined as

$$D_w = F - D_s \frac{v_s}{v_w}, \tag{7.8}$$

where $F$ is the focal length of transducer at water, $D_s$ is the focused depth inside the sample, $v_w$ is the wave speed in water, and $v_s$ is the wave speed in the sample.

### Material characterization

The processing of the backscattered signals for material characterization was accomplished as follows. An 8-th order ARMA (Auto-Regressive Moving Average) system model with its impulse response approximating the reference pulse was first built using a nonlinear least-squares fitting utility in the MATLAB Toolbox. The backscattered signals were then deconvolved to obtain the corresponding reflection coefficient sequences. A band-pass filter was next used to remove the DC and higher frequency components from the reflection coefficient sequences. The spectra of the

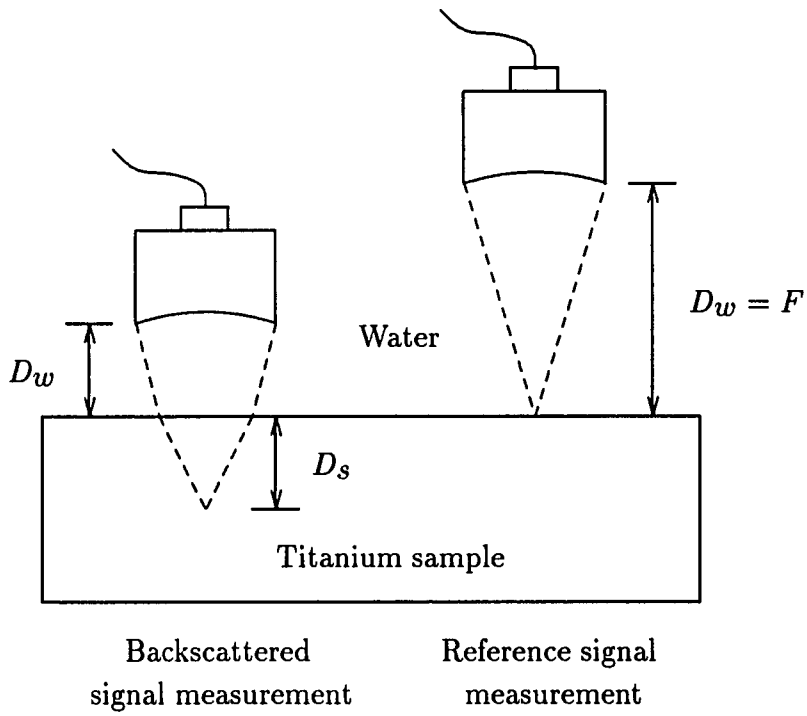


Figure 7.3: Experimental setup for measuring backscattered signal and reference pulse

reflection coefficient sequences were then estimated using both periodogram and AR methods. Using the frequency range from 5 to 15 MHz, the features $F_0$ and $F_1$ were finally extracted from these spectra. In estimating the spectra, different window sizes ($L$) and different AR model orders ($q$) were used.

The results corresponding to an AR (10) model and window sizes of 350, 256, 128 and 64 are shown in Figure 7.4. In this figure, the feature vector $\mathbf{x} = [\ F_0 \quad F_1\ ]^T$ of distribution class $i$ is assumed to have bivariate normal density function

$$p_i(\mathbf{x}) = \frac{1}{2\pi|\mathbf{R}_i|^{1/2}} \exp\Big[-\frac{1}{2}(\mathbf{x}-\mathbf{m}_i)^T \mathbf{R}_i^{-1}(\mathbf{x}-\mathbf{m}_i)\Big], \tag{7.9}$$

where mean vector $\mathbf{m}_i$ and covariance matrix $\mathbf{R}_i$ are defined as

$$\mathbf{m}_i = E\{\mathbf{x}_i\} \tag{7.10}$$

$$\mathbf{R}_i = E\Big\{(\mathbf{x}_i - \mathbf{m}_i)(\mathbf{x}_i - \mathbf{m}_i)^T\Big\}. \tag{7.11}$$

The ellipses in the figure indicate contours of constant probability density functions when the feature vectors corresponding to each sample were fitted with a two-dimensional Gaussian distribution. The lengths of the major and minor axes of each ellipse represent twice the standard deviation ($2\sigma$) along the respective directions. It is seen that features $F_0$ and $F_1$ can distinguish between the three titanium samples even though the order of the samples along the $F_0$ axis does not correspond to any of the orders of the average grain diameters indicated in Table 7.1. It is also seen that the three titanium samples are well separated in the feature space even when the window size used is relatively small. (Note: For titanium material and a 100 MHz sampling frequency, a distance of 1 mm corresponds to a window size $L$ of about 32.) This suggests the possibility of using the features for flaw detection as well when the microstructures of the host material and flaw are different.

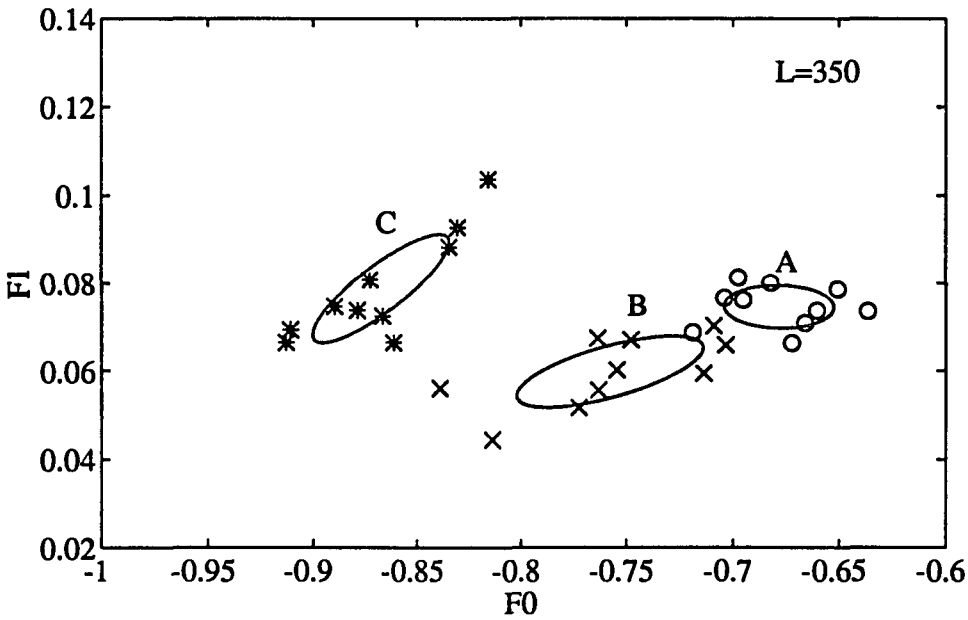


(a)

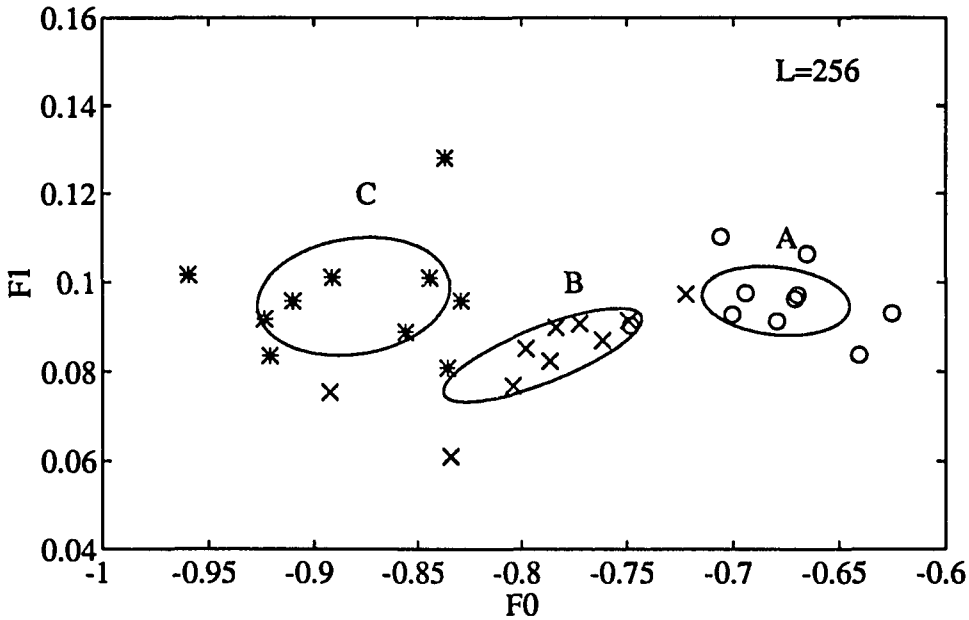


(b)

Figure 7.4: Feature vector distributions for AR (10) model: (a) $L = 350$, (b) $L = 256$, (c) $L = 128$, (d) $L = 64$

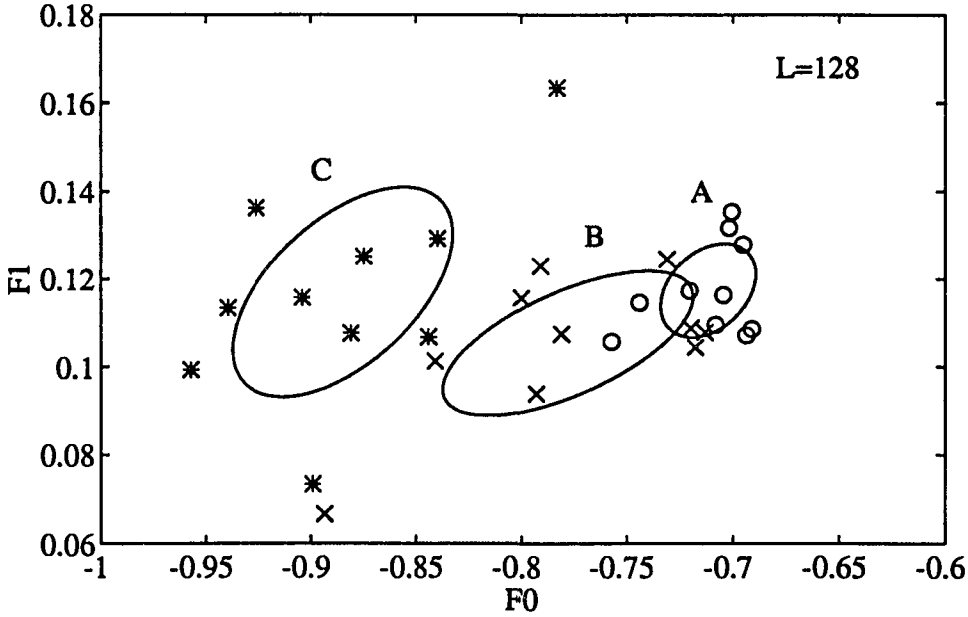


(c)

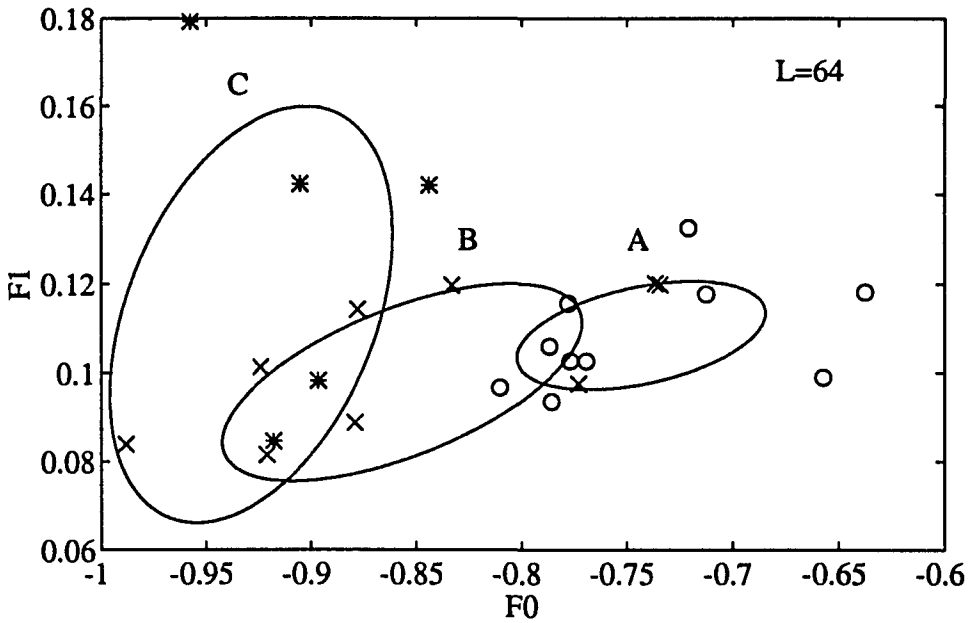


(d)

Figure 7.4 (Continued)

Table 7.2: Separability measure for different window sizes

| Method | Number of samples | | | |
|---|---|---|---|---|
| | $L = 350$ | $L = 256$ | $L = 128$ | $L = 64$ |
| Periodogram | 2.93 | 3.73 | 1.69 | 0.75 |
| AR (2) | 3.25 | 2.34 | 1.47 | 0.51 |
| AR (4) | 1.20 | 0.98 | 1.98 | 0.59 |
| AR (6) | 3.72 | 2.07 | 2.69 | 0.83 |
| AR (8) | 4.65 | 2.92 | 1.76 | 0.50 |
| AR (10) | 5.15 | 3.81 | 2.21 | 1.07 |

In order to quantify the separation between the different distributions in the feature space, a separability measure $J_4$ was used (Fukunaga, 1972; Parsons, 1987). This measure is defined as

$$J_4 = \frac{\text{tr } \mathbf{B}}{\text{tr } \mathbf{W}}, \tag{7.12}$$

where the pooled *intraclass* covariance matrix $\mathbf{W}$, and the *interclass* covariance matrix $\mathbf{B}$ are defined as

$$\mathbf{W} = E\{\mathbf{R}_i\} \tag{7.13}$$

$$\mathbf{B} = E\Big\{(\mathbf{m}_i - \mathbf{m})(\mathbf{m}_i - \mathbf{m})^T\Big\}. \tag{7.14}$$

In Equation (7.14), $\mathbf{m}$ is the mean of $\mathbf{m}_i$ over all distribution classes. This is a measure of the ratio of the variance of the means of the different distributions and the mean of their variances. For different window sizes and different orders of AR model, this separability measure is listed in Table 7.2. It is seen that the separability generally increases with the AR model order $q$ and that it decreases as the window size $N$ decreases.

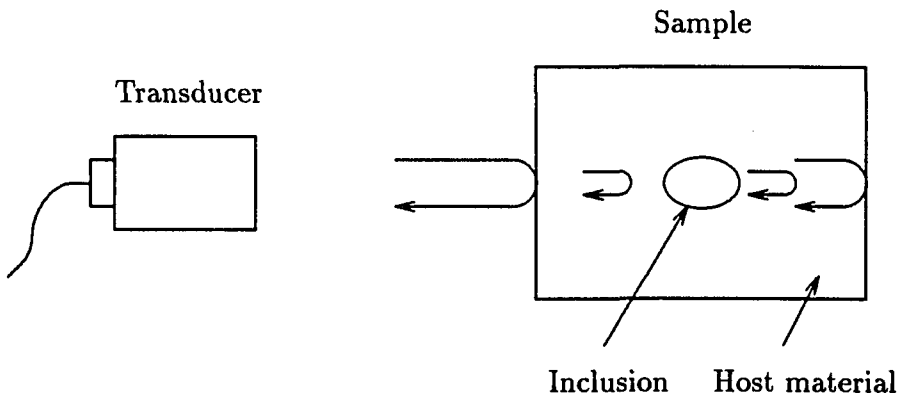


Figure 7.5: Basic concept of inclusion detection

### Inclusion detection

The signal processing method was also applied for detecting an inclusion which has different microstructure from the host material. Figure 7.5 shows the basic concept to distinguish between host material and inclusion, for example, nominal titanium alloy and hard alpha inclusions (Costa *et al.*, 1990). The simulated ultrasonic data were generated by inserting an appropriate number of samples of the reflection coefficient sequence of the the inclusion within the reflection coefficient sequence of the host material, and convolving it with a reference pulse. In generating simulated data, we can distinguish three different combinations of host material and inclusion: A host material and C inclusion (A:C), B host material and C inclusion (B:C), A host material and B inclusion (A:B). As shown in Figure 7.4, the distance between the feature vector distributions of A:B combination is the closest and A:C combination the furthest.

In the inclusion detection problem, we might select two hypothesis, viz. an inclusion is present or no inclusion is present. This is the binary hypothesis testing to

select null hypothesis ($H_0$), the event that no inclusion is present, or the alternative hypothesis ($H_1$), the event that an inclusion is present. Symbolically this can be written as

$$H_0: \quad \mathbf{x} \in \text{Host material} \tag{7.15}$$

$$H_1: \quad \mathbf{x} \in \text{Inclusion.} \tag{7.16}$$

We assume that the feature vectors of null and alternative hypotheses follow a Gaussian distribution.

$$H_0: \quad \mathbf{x} \sim N(\mathbf{m}_0, \mathbf{R}_0) \tag{7.17}$$

$$H_1: \quad \mathbf{x} \sim N(\mathbf{m}_1, \mathbf{R}_1), \tag{7.18}$$

where $\mathbf{m}_0$, $\mathbf{m}_1$ are sample means and $\mathbf{R}_0$, $\mathbf{R}_1$ are sample covariances of feature vectors of host material and inclusion, respectively. In order to simplify the hypothesis testing, we assume that the parent population of feature vectors of the host material and the inclusion has a covariance matrix that is the average of the covariance matrices of the host material and inclusion. Thus, we estimate $\mathbf{R}$ as

$$\mathbf{R} = \frac{1}{2}(\mathbf{R}_0 + \mathbf{R}_1). \tag{7.19}$$

In this case, the covariance matrices are common under both hypotheses. Based on feature vector observation, we must choose between these hypotheses. One reasonable decision criterion for this problem is to choose that hypothesis which is most likely to have occurred based on feature vector observation. Using this criterion, the decision rule is to choose $H_1$ if

$$P(H_0|\mathbf{x}) \leq P(H_1|\mathbf{x}), \tag{7.20}$$

and choose $H_0$ otherwise, where $P(H_i|\mathbf{x})$ is the conditional probability that $H_i$ is true for the given feature vector $\mathbf{x}$. This decision rule may also be expressed in terms of probability density functions. When $P(H_0)$ is the a priori probability that hypothesis $H_0$ is true, the decision rule may be rewritten using probability density functions: choose $H_1$ if

$$\frac{p_1(\mathbf{x})}{p_0(\mathbf{x})} \geq \frac{P(H_0)}{1-P(H_0)}, \tag{7.21}$$

and choose $H_0$ otherwise. In Equation (7.21), the ratio $p_1(\mathbf{x})/p_0(\mathbf{x})$ is of particular importance and is called *likelihood ratio.* It is frequently convenient to use *log-likelihood ratio* which is the natural logarithm of the likelihood ratio. From Equation (7.9), the log-likelihood ratio is

$$\begin{aligned} L(\mathbf{x}) &= \ln \frac{p_1(\mathbf{x})}{p_0(\mathbf{x})} \\ &= -\frac{1}{2}(\mathbf{x}-\mathbf{m}_1)^T\mathbf{R}^{-1}(\mathbf{x}-\mathbf{m}_1) + \frac{1}{2}(\mathbf{x}-\mathbf{m}_0)^T\mathbf{R}^{-1}(\mathbf{x}-\mathbf{m}_0) \\ &= (\mathbf{m}_1-\mathbf{m}_0)^T\mathbf{R}^{-1}\mathbf{x} - \frac{1}{2}(\mathbf{m}_1+\mathbf{m}_0)^T\mathbf{R}^{-1}(\mathbf{m}_1-\mathbf{m}_0). \end{aligned} \tag{7.22}$$

In Equation (7.22), the first term is the test statistic and is Gaussian distributed because it is a linear transform of the Gaussian distributed feature vector $\mathbf{x}$. This function is also called the Fisher's discriminant function (Johnson and Wichern, 1988).

$$y = (\mathbf{m}_1-\mathbf{m}_0)^T\mathbf{R}^{-1}\mathbf{x} \tag{7.23}$$

If we assume that host material and inclusion are equally probable (i.e., $P(H_0) = 1/2$), then the classification rule $y_0$ is

$$y_0 = \frac{1}{2}(\mathbf{m}_1+\mathbf{m}_0)^T\mathbf{R}^{-1}(\mathbf{m}_1-\mathbf{m}_0). \tag{7.24}$$

Thus, we choose $H_1$ if $y \geq y_0$ and choose $H_0$ if $y < y_0$. Figure 7.6 shows the

decision line determined from Equations (7.23) and (7.24) when host material is A and inclusion material is C with inclusion size of 4 mm.

In the inclusion detection problem, the a priori probabilities and the cost of each kind of error are difficult to determine. For this case, the Neyman-Pearson criterion (Scharf, 1991; Whalen, 1971) is commonly employed. The objective of this criterion is to maximize the probability of detection (POD) for a given probability of false alarm (POF). The POD results from using different materials and different sizes of inclusion are shown in Figure 7.7 when POF is 0.1. As shown in Figure 7.4, the distance between distributions of material A and B is closest and A and C furthest. This agrees with the POD results. The results show good probability when size of inclusion is larger than 4 mm.

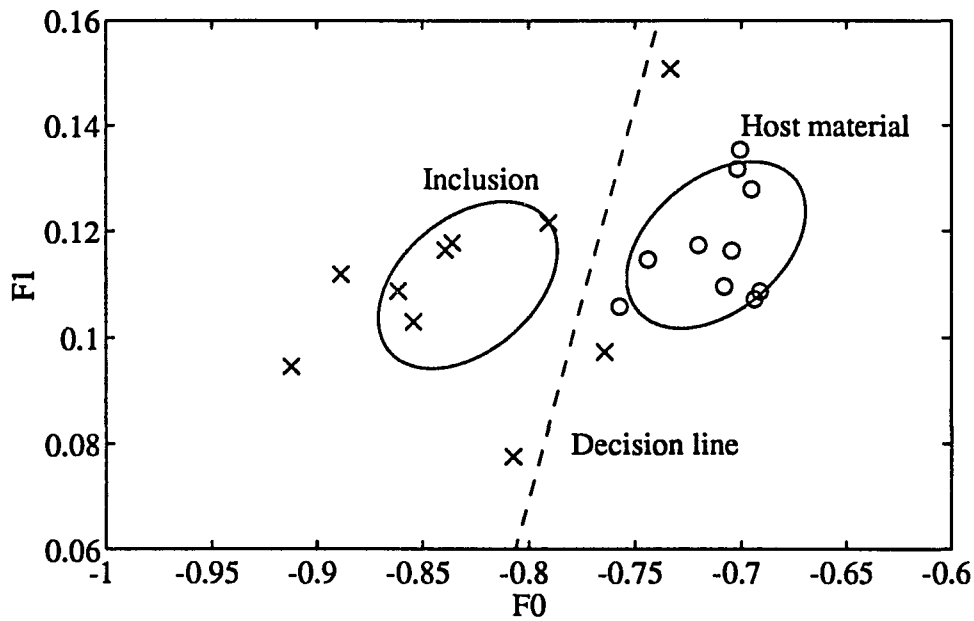


Figure 7.6: Decision line of host material A and inclusion C with inclusion size of 4 mm

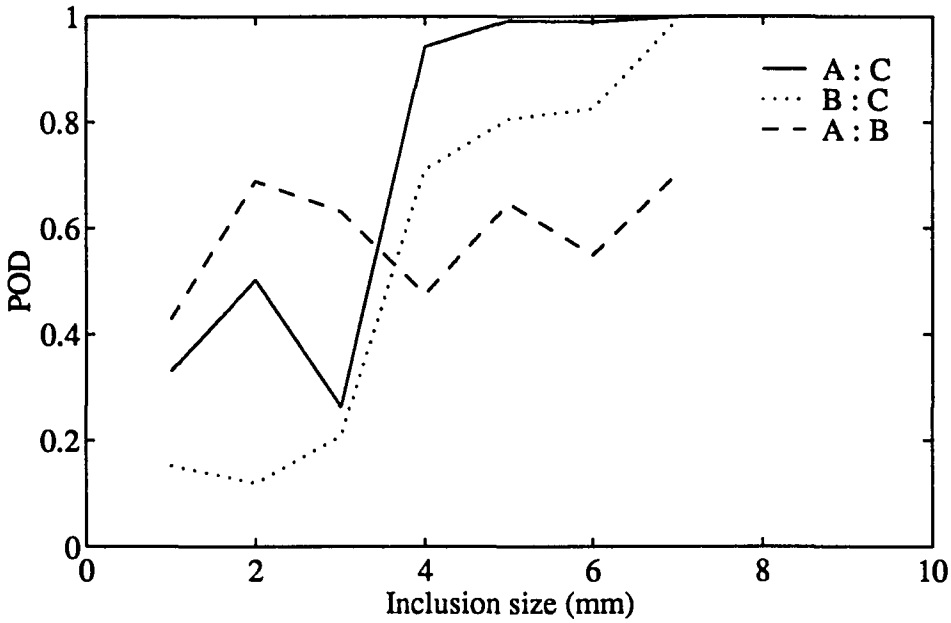


Figure 7.7: POD performances of different host materials and inclusions (POF=0.1)

# CHAPTER 8. SUMMARY AND CONCLUSIONS

A wavelet transform based signal processing method has been developed for ultrasonic flaw detection. The wavelet transform is a recently developed signal analysis tool that can provide a time-frequency description of a given signal. An engineering interpretation of the wavelet transform is a set of bandpass filters with different center frequencies and bandwidths. In the proposed signal processing method, the received ultrasonic signal is passed through several bandpass filters with different center frequencies but with the same bandwidth. The magnitude peaks of the filtered signals are then used in the detection process. Two types of features are extracted from these peaks: (1) relative peak location and (2) magnitude ratio with respect to one of the filtered signals regarded as reference. These features are also used in the detection process. The performance of the proposed method was evaluated using simulated ultrasonic data. In order to justify the usefulness of the selected features, the probability distributions of the features were derived under certain assumptions. The performance of the proposed technique was evaluated by means of a receiver operating characteristics (ROC) curve using simulated ultrasonic data and compared with the performance of the matched filter. It was shown that the detection performance achieved was close to that of the matched filter.

The wavelet transform based signal processing method has been applied to the

hard-alpha detection problem. Hard alpha inclusions represent brittle regions in titanium alloy materials that arise from high oxygen or nitrogen concentration. When components made of titanium alloy material, e.g. fan disks in aircraft engines, are subjected to stress, the hard-alpha inclusions may lead to cracks and eventual failure of the components. Detection of these inclusions is therefore an important NDE problem. In order to study the effectiveness of the wavelet transform based signal processing method in solving the hard-alpha detection problem, two data sets were prepared. Because of the difficulty in preparing actual hard-alpha inclusions, the flaw signals were simulated using the Thompson-Gray measurement model. The grain noise signals, however, were obtained from an actual titanium sample. In order to understand and characterize the grain noise data, statistical analysis of the data was performed. The detection performance of the wavelet transform based signal processing method was evaluated using the receiver operating characteristics (ROC), i.e., POD versus POF, curves. It was found that the detection performance of the proposed signal processing method is comparable to that of the matched filter.

A Kalman filter based deconvolution algorithm has been developed for estimating material reflection coefficient sequence. The Kalman filter based deconvolution algorithm is based on the state-space modeling of the ultrasonic measurement system. Since the Kalman filter can handle time-varying systems and non-stationary statistics quite naturally, it is better suited for such situations than the Wiener filter approach. The developed deconvolution algorithm was implemented in software using C and MATLAB programming language and tested extensively using simulated and actual ultrasonic data. The algorithm showed good resolving capability in test using single and double reflectors. Deconvolution performances of the Kalman filter and Wiener

filter based approach were compared using actual data measured from a titanium alloy sample. The algorithm was used to characterize a layered composite material. From the spectral peak of deconvolved signal, the layer thickness was easily identified by removing measurement system response. It is expected that the algorithm will be useful for different applications in the NDE area.

In applying the Kalman filter based deconvolution algorithm, the deconvolved sequence is typically assumed white. However, material reflection coefficient sequences which are the deconvolved sequences in the present case are generally colored. In order to handle this situation, a simple iterative for estimating colored input sequence using Kalman filter based deconvolution algorithm has been developed. In the iterative scheme, the colored input sequence is modeled as the output of shaping filter excited by white noise sequence. The shaping filter is considered as part of the system while applying the Kalman filter based deconvolution algorithm to estimate the noise sequence. To begin with, the shaping filter is just an identity filter. The estimated input sequence is then used to update its coefficients iteratively until the change in the coefficient values is small. The iterative scheme was tested using simulated data. The signal to be deconvolved was generated using two system models, viz., a second order and a sixth order model. The shaping filter was modeled as a second order AR model. Four different shaping filters which have different shaping effects were chosen for testing. Using simulated data, the deconvolution performance of the iterative scheme and the Kalman filter based minimum-variance deconvolution (MVD) algorithm were compared. It was seen that the iterative scheme performs better than MVD algorithm in general for second order system model, low-pass colored noise.

In deconvolution of ultrasonic signals acquired from an attenuating medium, the

effect of signal attenuation should be appropriately accounted for in the deconvolution technique. If the signal arises from a localized inhomogeneities as in the case of flaw scattered signals, this is easily accomplished by suitably modifying the reference signal. When the inhomogeneities are distributed throughout the material as in the case of grain backscattered signals, the correction for attenuation should vary along the depth of the material. A suitable deconvolution technique for incorporating such correction is based on the Kalman filter. The Kalman filter based deconvolution algorithm is implemented in the time-domain and can be easily modified to handle space-varying systems. A model parameter interpolation method to handle such space-varying systems to incorporate the effect of ultrasonic attenuation has been proposed. In this technique, the reference signal and the signal to be processed are modeled respectively as the impulse response of a system and the system output. The input to the system is the deconvolved signal that has to be estimated. The Kalman filter algorithm processes the data sequentially and its formulation allows the system parameters to change at each step. This property can be taken advantage of in providing varying amounts of correction for attenuation along the depth of the material. A model parameter interpolation method to provide suitable correction for space varying attenuation was investigated. System models (AR or ARMA) were first built for the front and back surface echoes obtained from a suitable sample. The parameters of these models were then interpolated to obtain models corresponding to intermediate depths. The impulse responses of the interpolated models represent the reference signals corrected for attenuation. The effectiveness of this approach was evaluated using experimentally obtained signals from copper samples of different thicknesses (1/4, 1/2, 3/4 and 1 inches). It was shown that the backscattered signals

estimated using the model parameter interpolation method were very close to those signals estimated using Wiener filter.

A new signal processing technique to process the grain backscattered signals and extract features that can be used for material characterization has been developed. The technique consists of the following three steps: (1) deconvolution of the backscattered signal to remove the effect of the measurement system, (2) estimation of the spectrum of the resulting reflection coefficient sequence, and (3) extraction of features from the spectrum related to the average scattered energy and the rate of change of scattered energy with frequency, both computed within the bandwidth of the ultrasonic transducer. The spectral features so extracted are influenced by the microstructural properties of a material pertaining to scattering, e.g., average grain diameter, and can be used in the characterization of these properties. The features were applied to the characterization of some pure titanium samples with different grain sizes. The features show good potential for material characterization and flaw detection as well. The signal processing technique was applied for detecting an inclusion which has different microstructure from the host material. The test results using simulated ultrasonic data showed good detection performance when inclusion size is larger than 4 mm.

# BIBLIOGRAPHY

Beecham, D. 1966. Ultrasonic scatter in metals: its properties and its application to grain size determination. Ultrasonics 4: 67–76.

Bilgutay, N. M., J. Saniie, E. S. Furgason and V. L. Newhouse. 1979. Flaw-to-grain echo enhancement. Proc. Ultrasonics International. pp. 152–157.

Bilgutay, N. M., J. S. Saniie and U. Bencharit. 1988. Spectral and spatial processing techniques for improved ultrasonic imaging of materials. Pages 71–85 in C. H. Chen ed. Proceedings of the NATO Advanced Research Workshop on Signal Processing and Pattern Recognition in Nondestructive Evaluation of Materials, Vol. F44, Springer-Verlag, Berlin, Germany.

Birks, A. S., R. E. Green, Jr., P. McIntire, eds. 1991. Nondestructive testing handbook, 2nd ed., Vol. 7: Ultrasonic testing. American Society for Nondestructive Testing, Columbus, OH.

Brown, R. G. 1983. Introduction to random signal analysis and Kalman filtering. John Wiley & Sons, New York, NY.

Chen, C. H. 1984. Linear system theory and design. Holt, Reinehart and Winston, New York, NY.

Chen, C. H. 1988. Signal processing in nondestructive evaluation of materials. Pages 661–682 in C. H. Chen, eds. Signal processing handbook, Marcer Dekker, New York, NY.

Chen, C. H., and S. K. Sin. 1990. On effective spectrum-based ultrasonic deconvolution techniques for hidden flaw characterization. J. Acoust. Soc. Am. Vol. 87: 976–987.

Chi, C. Y., and J. M. Mendel. 1984. Performance of minimum-variance deconvolution. IEEE Trans. ASSP. ASSP-32: 1145–1153.

Chiou, C. P., R. B. Thompson and L. W. Schmerr. 1993a. Model-based signal processing techniques for ultrasonic flaw detection: simulation studies. Pages 703–710 in D. O. Thompson and D. E. Chimenti, eds. Review of Progress in Quantitative NDE, Vol 12A, Plenum Press, New York.

Chiou, C. P., L. W. Schmerr and R. B. Thompson. 1993b. Ultrasonic flaw detection using neural network models and statistical analysis: simulation studies. Pages 789–795 in D. O. Thompson and D. E. Chimenti, eds. Review of Progress in Quantitative NDE, Vol 12A, Plenum Press, New York.

Costa, J. G., R. E. Gonzalez, R. E. Guyotte, D. P. Salvano, T. Swift and R. J. Koenig. 1990. Titanium rotating components review team report. Federal Aviation Administration, Washington, DC.

Daubechies, I. 1992. Ten lectures on wavelets. Society for Industrial and Applied Mathematics, Philadelphia, PA.

Fay, B., K. Brendel and G. Ludwig. 1976. Studies of inhomogeneous substances by ultrasonic backscattering. Ultrasound Med. Biol. 2: 195–198.

Fitting, D. W. and L. Adler. 1981. Ultrasonic spectral analysis for nondestructive evaluation. Plenum Press, New York, NY.

Frederick, J. R. and J. A. Seydel. 1973. Improved discontinuity detection using computer-aided ultrasonic pulse-echo technique. Welding Research Council Bulletin, 185: 1–23

Frisch, M. and H. Messer. 1992. The use of the wavelet transform in the detection of an unknown transient signal. IEEE Trans. on Information Theory. 38: 892–897.

Fukunaga, K. 1972. Introduction to statistical pattern recognition. Academic Press. New York, NY.

Furgason, E. S., V. L. Newhouse, N. M. Bilgutay and G. R. Cooper. 1975. Application of random signal correlation techniques to ultrasonic flaw detection. Ultrasonics. 13: 11–17.

Goebbels, K. and P. Holler. 1980. Quantitative determination of grain size and detection of inhomogeneities in steel by ultrasonic backscattering measurements. pages 1816–1824 in H. Berger and M. Linzer ed. Ultrasonic Materials Characterization, Special Publication 596. National Bureau of Standards, Gaithersburg, MD.

Grace, A. 1992. Optimization toolbox user's guide. The Math Works Inc., Natick, MA.

Grossmann, A and J. Morlet. 1984. Decomposition of Hardy functions into square integrable wavelets of constant shape. SIAM J. Math. Anal., 15: 724–736.

Hahn, G. J. and S. S. Shapiro. 1967. Statistical models in engineering. Wiley, New York, NY.

Jawerth, Björn, and Wim Sweldens. 1993. An overview of wavelet based multiresolution analyses.

Johnson, R. A., and D. W. Wichern. 1988. Applied multivariate statistical analysis. Prentice-Hall, Englewood Cliffs, NJ.

Kalman, R. E. 1960. A new approach to linear filtering and prediction problems. Trans. of the ASME Jour. of Basic Engr. series D, 82: 35–46.

Kalman , R. E. and R. S. Bucy. 1961. New results in linear filtering and prediction. Trans. of the ASME Jour. of Basic Engr. 83: 95–108.

Kay, S. M., and S. L. Marple. 1981. Spectrum analysis - A modern perspective. Proc. IEEE Vol. 69: 1381–1419.

Krautkrämer, J., and H. Krautkrämer. 1991. Ultrasonic testing of materials, 4th ed. Springer-Verlag, Berlin, Germany.

Kuc, R. B. 1979. Application of Kalman filtering techniques to diagnostic ultrasound. Ultrasonic Imaging Vol. 1:105–120.

Lee, B. B. and E. S. Furgason. 1981. A new digital correlation flaw detection system. Journal of Nondestructive Evaluation. 2: 57–63.

Marple, S. L. 1987. Digital spectral analysis. Prentice-Hall, Englewood Cliffs, NJ.

Meditch, J. S. 1969. Stochastic optimal linear estimation and control. McGraw-Hill, New York, NY.

Mendel, J. M., and J. Kormylo. 1977. New fast optimal white-noise estimators for deconvolution. IEEE Trans. on Geosc. Electronics GE-25: 32–41.

Mendel, J. M. 1977a. White-noise estimators for seismic data processing in oil exploration. IEEE Trans. on Automatic Control AC-22: 694–706.

Mendel, J. M., 1977b. Minimum -variance deconvolution. IEEE Trans. on Automatic Control Vol. AC-22: 694–706.

Mendel, J. M., 1981. Minimum-variance deconvolution. IEEE Trans. on Geoscience and Remote sensing Vol. GE-19: 161–171.

Mendel, J. M. 1983. Optimal seismic deconvolution: An estimation-based approach. Academic press, New York, NY.

Mendel, J. M. 1987. Lessons in digital estimation theory. Prentice-Hall, Englewood Cliffs, NJ.

Morlet, J. 1983. Sampling theory and wave propagation. Pages 233–261 in C. H. Chen, ed. NATO ASI Series Vol. 1, Issues in Acoustic Signal/Image Processing and Recognition, Springer-Verlag, Berlin, Germany.

Morlet, J., G. Arens, I. Fourgreau and D, Giard. 1982. Wave propagation and sampling theory. Goephysics, 47: 203–236.

Neal, S. P. 1988. A prior knowledge based optimal Wiener filtering approach to ultrasonic scattering amplitude estimation. Iowa State University, Ames, IA.

Newhouse, V. L., N. M. Bilgutay, J. Saniie and E. S. Furgason. 1982. Flaw-to-grain echo enhancement by split-spectrum processing. Ultrasonics, 20: 59–68.

Oppenheim, A. V. and R. W. Schafer. 1989. Discrete-time signal processing. Prentice-Hall, Englewood Cliffs, NJ.

Ott, N., and H. G. Meder. 1972. The Kalman filter as a prediction error filter. Geophys. Prospect. Vol. 20: 549–560.

Parsons, T. 1987. Voice and speech processing. McGraw-Hill, New York, NY.

Petropulu, A. P. 1992. Detection of transients using discrete wavelet transform. Proc. IEEE ICASSP, Vol. 2: 477–480

Proakis, J. G. and D. G. Manolakis. 1988. Introduction to digital signal processing. Macmillan Publishing Company, New York, NY.

Ramabadran, T. V. 1990. Detection of hard alpha inclusions in titanium alloys using ultrasonic backscattered energy. Center for Nondestructive Evaluation, Internal report (Jan. 1990).

Ramabadran, T. V., C. P. Chiou, M. H. Yoon and J. P. Basart. 1991. Detection of hard-alpha inclusions in titanium alloys using ultrasonic testing methods. Center for Nondestructive Evaluation, Internal report (June 1991).

Ramabadran, T. V., and M. H. Yoon. 1991. Deconvolution of ultrasonic backscattered signals using the Kalman filter. Pages 733–740 in D. O. Thompson and D. E. Chimenti, eds. Review of Progress in Quantitative NDE, Vol 10A, Plenum Press, New York.

Rioul, O. and M. Vetterli. 1991. Wavelets and signal processing. IEEE Signal Proc. Mag. 8: 14–38.

Rose, J. H. 1989. Detection of hard alpha inclusions in titanium jet engine materials. Center for Nondestructive Evaluation, Internal report (Dec. 1989).

Saniie, J. and N. M. Bilgutay. 1986. Quantitative grain size evaluation using ultrasonic backscattered echoes. J. Acoust. Soc. Am. 80: 67–74.

Saniie, J. and T. Wang and N. M. Bilgutay. 1989. Analysis of homomorphic processing for ultrasonic grain signal characterization. IEEE Trans. on Ultrasonics, Ferroelectrics, and Frequency Control. Vol. 36: 365–375.

Saniie, J. and D. T. Nagle. 1992. Analysis of order-statistic CFAR threshold estimators for improved ultrasonic flaw detection. IEEE Trans. on Ultrasonics, Ferroelectrics, and Frequency Control, Vol. 39: 618–629.

Scharf, L. L. 1991. Statistical signal processing: detection, estimation, and time series analysis. Addison-Wesley, Reading, MA.

Shapiro, S. S. 1990. How to test normality and other distributional assumptions. American Society for Quality Control, Milwaukee, WI.

Sorenson, H. W. 1980. Parameter estimation: principles and problems. Dekker, New York, NY.

Stanke, F. E. and G. S. Kino. 1984. A unified theory for elastic wave propagation in polycrystalline materials. J. Acoust. Soc. Amer. 75: 665–681.

Thompson, R. B., and D. O. Thompson. 1985. Ultrasonics in nondestructive evaluation. Proceedings of the IEEE 73(12): 1716–1755

Thompson, R. B., and T. A. Gray. 1983. A model relating scattering measurements through liquid-solid interfaces to unbounded medium scattering amplitudes. J. Acoust. Soc. Am. 74(4): 1279–1290.

Tuteur, F. B. 1988. Wavelet transformations in signal detection. Proc. IEEE ICASSP, Vol. 3: 1435–1438

Van Trees, H. L. 1968. Detection, estimation, and modulation theory. Wiley, New York, NY.

Whalen, A. D. 1971. Detection of signals in noise. Academic Press, San Diego, CA.

Yoon, M. H., and T. V. Ramabadran. 1991. Estimation of colored plant noise using Kalman filter based deconvolution. Proceedings of the 1991 IEEE International Conference on Systems Engineering. pp. 408–411.

Yoon, M. H., and T. V. Ramabadran. 1992. Characterization of materials using grain backscattered ultrasonic signals. Pages 959–965 in D. O. Thompson and D. E. Chimenti, eds. Review of Progress in Quantitative NDE, Vol. 11A, Plenum Press, New York, NY.

Yoon, M. H., and T. V. Ramabadran. 1993. Accounting for ultrasonic signal attenuation through model parameter interpolation. Pages 767–774 in D. O. Thompson and D. E. Chimenti, eds. Review of Progress in Quantitative NDE, Vol. 12A, Plenum Press, New York, NY.

Yue, L. and Y. Chong-Fu. 1987. Two signal processing techniques for the enhancement of the flaw-to-grain echo ratio. Ultrasonics. 25: 90–94.

# ACKNOWLEDGMENTS

I would like to express my sincere appreciation to my major professor Dr. Tenkasi V. Ramabadran for his constant help, support, and invaluable advice throughout this study. I would like to thank my co-major professor Dr. John P. Basart and committee members Dr. Donald O. Thompson, Dr. William Q. Meeker Jr., and Dr. Hsien-Sen Hung for their valuable comments and help in this study. My thanks also go to Dr. Frank Margaten in the CNDE who allowed me to use his ultrasonic facilities, and to Dr. Chien-Ping Chiou in the CNDE who provided me with the ultrasonic data used in this experiment. I would also like to thank my officemate Keshi Chen for his help in preparing this dissertation.

I would like to thank my parents in Korea who always prayed for me and encouraged me to finish this study. I would also like to thank my parents-in-law and their family for their constant love, encouragement, support, and taking care of my son when I was in difficulty. I wish to express my utmost gratitude to my wife Kwiock for her love, encouragement, and sacrifice. I dedicate this dissertation to my lovely wife Kwiock and my cute son Sukhan.

This work was partially supported by the Center for Nondestructive Evaluation (CNDE) at Iowa State University.